The bone ecosystem facilitates multiple myeloma relapse and the evolution of heterogeneous proteasome inhibitor resistant disease.

Authors/affiliations

Ryan T. Bishop[1]*, Anna K. Miller[2]*, Matthew Froid[2,3], Niveditha Nerlakanti[1,3]Tao Li[1], Jeremy Frieling[1], Mostafa Nasr[1,3], Karl Nyman[1,3] Praneeth R Sudalagunta[4], Rafael Canevarolo[4], Ariosto Siqueira Silva[4], Kenneth H. Shain[1,5], Conor C. Lynch[1]+ and David Basanta[2]+

[1] Tumor Biology Department, H. Lee Moffitt Cancer Center and Research Institute, Tampa, Florida

[2] Department of Integrated Mathematical Oncology, H. Lee Moffitt Cancer Center and Research Institute, Tampa, Florida

[3] The Cancer Biology Ph.D. Program, University of South Florida, Tampa, Florida, USA.

[4] Department of Metabolism and Physiology, H. Lee Moffitt Cancer Center and Research Institute, Tampa, FL 33612, USA

[5] Department of Malignant Hematology, H. Lee Moffitt Cancer Center and Research Institute, Tampa, Florida

*+ These authors contributed equally.

Abstract

Multiple myeloma (MM) is an osteolytic plasma cell malignancy that, despite being responsive to therapies such as proteasome inhibitors, frequently relapses. Understanding the mechanism and the niches where resistant disease evolves remains of major clinical importance. Cancer cell intrinsic mechanisms and bone ecosystem factors are known contributors to the evolution of resistant MM but the exact contribution of each is difficult to define with current *in vitro* and *in vivo* models. However, mathematical modeling can help address this gap in knowledge. Here, we describe a novel biology-driven hybrid agent-based model that incorporates key cellular species of the bone ecosystem that control normal bone remodeling and, in MM, yields a protective environment under therapy. Critically, the spatiotemporal nature of the model captures two key features: normal bone homeostasis and how MM interacts with the bone ecosystem to induce bone destruction. We next used the model to examine how the bone ecosystem contributes to the evolutionary dynamics of resistant MM under control and proteasome inhibitor treatment. Our data demonstrates that resistant disease cannot develop without MM intrinsic mechanisms. However, protection from the bone microenvironment dramatically increases the likelihood of developing intrinsic resistance and subsequent relapse. The spatial nature of the model also reveals how the bone ecosystem provides a protective niche for drug sensitive MM cells under treatment, consequently leading to the emergence of a heterogenous and drug resistant disease. In conclusion, our data demonstrates a significant role for the bone ecosystem in MM survival and resistance, and suggests that early intervention with bone ecosystem targeting therapies may prevent the emergence of heterogeneous drug resistant MM.

Introduction

Multiple myeloma (MM) is the second most common hematological malignancy in the US[1], characterized by the clonal expansion of plasma cells localized primarily in the bone marrow microenvironment of the skeleton [2,3]. In the bone microenvironment, MM cells disrupt the finely tuned balance of trabecular and cortical bone remodeling to generate osteolytic lesions. This is primarily via MM-induced inhibition of osteoblastic bone formation and increase of osteoclastic bone resorption. There are currently several approved therapies to treat MM including, but not limited to, proteasome inhibitors (e.g., bortezomib and carfilzomib), chemotherapy (e.g., melphalan), immunomodulatory drugs (e.g., lenalidomide), and cellular and non-cellular immunotherapies (e.g., B cell maturation antigen (BCMA) chimeric antigen receptor- (CAR) T cells and daratumumab) that significantly contribute to the long-term survival of MM patients[4]. However, MM remains fatal as nearly all patients ultimately become refractory to various lines of therapy. A greater understanding of how resistant MM emerges in the clinical setting can yield new treatment strategies to slow relapse times and extend the efficacy of standard of care therapies.

In MM and other cancers, the tumor microenvironment is a well-known contributor to the development of treatment resistance[5-10]. MM is an archetype of cancer cell-stroma interactions whereby MM cells reside and metastasize systemically within the bone marrow microenvironment[11]. In the bone ecosystem, MM interacts closely with mesenchymal stem cells (MSCs) and other progenitor cells[6,12-15] that secrete MM pro-survival and proliferative factors. Additional studies have shown that the bone marrow microenvironment can also protect MM cells from applied therapy in a phenomenon known as environment mediated drug resistance (EMDR)[7,8,16]. Reciprocally, it is well established that MM-derived factors stimulate osteoblast lineage cells to recruit and activate osteoclasts through receptor activator of nuclear factor kappa-B ligand (RANKL) production, which in turn degrade the bone matrix to release stored cytokines and growth factors (e.g., transforming growth factor-beta, TGF-β) that support MM survival and growth[2,3,5-10]. MM cells also suppress osteoblast maturation, thus tipping the balance towards excessive bone destruction[2,3]. This vicious cycle leads to complications for MM

patients such as hypercalcemia and pathological fracture that greatly contribute to morbidity and mortality[17].

While EMDR can contribute to drug resistance, MM intrinsic mechanisms, such as genetic and epigenetic alterations, also play a significant role in the process. For example, increased expression of the anti-apoptotic BCL2 protein family is important in mediating MM resistance to proteasome inhibition[18-21]. In fact, depending on selective pressures by different lines of therapies and clonal mutation capacity, MM may evolve to develop multiple mechanisms of resistance[5,22,23]. While EMDR and intrinsic drug resistance mechanisms contribute to the emergence of refractory disease several questions remain: i) How does the interplay between each mechanism contribute to the evolution of resistant MM? ii) How does each mechanism contribute to the heterogeneity of the disease under either control or treatment conditions? iii) Could targeting EMDR alter the course of the disease or its responsiveness to applied therapy thereby yielding significantly greater depths of treatment response? In the context of the bone marrow microenvironment and the direct/indirect communications occurring in a temporal and spatial fashion between MM and stromal cells, these questions remain difficult to address using current *in vivo* and *ex vivo* approaches.

Mathematical models of the tumor microenvironment have become a valuable approach that allows us to interrogate the interactions between multiple cellular populations over time under normal or disease conditions. In particular, hybrid cellular automata (HCA) models which couple discrete cell-based models with partial differential equations include spatial aspects enabling users to locate where phenomena are occurring. Further, mathematical models have the potential for clinical translatability and can be used to study the impact of treatment on the tumor microenvironment and delay the onset of resistant disease[24-31]. We therefore leveraged these modeling approaches to examine MM progression and spatial evolution in response to therapy. To this end, we generated a novel HCA model powered by biological parameters from a mouse model of MM and demonstrate how it captures both normal bone turnover, and spatiotemporal cellular dynamics during MM progression in bone, such as loss of osteoblasts, increased stromal cell infiltration, osteoclast formation, and osteolysis. Additionally, we incorporate the proliferative and protective bone marrow microenvironment effects on MM mediated

by osteoclastic bone resorption and bone marrow stromal cells. In the treatment setting, the HCA demonstrates that EMDR contributes to minimal residual disease, protecting tumors from complete eradication. Moreover, this reservoir of MM cells increases the likelihood of unique resistance mechanisms arising over time and greatly contributes to the evolution of MM heterogeneity over time compared to non-EMDR scenarios. These results highlight the importance of the bone marrow microenvironment in contributing to MM resistance and patient relapse and provide a strong rationale for targeting both the MM and bone marrow microenvironment mechanisms for optimal treatment response.

Results

The HCA model recapitulates the key steps of trabecular bone remodeling.

Trabecular bone remodeling is a continuously occurring process that is essential for regulating calcium homeostasis and bone injury repair (Fig. 1a) [32,33]. This process occurs asynchronously throughout the skeleton at individual sites known as basic multicellular units (BMUs). The BMU in our HCA consists of five different cell types, including precursor osteoclasts, active osteoclasts, mesenchymal stem cells (MSCs), preosteoblasts, and osteoblasts. Additionally, we include central signaling molecules such as RANKL, a driver of preosteoclast motility and OC formation[34] and osteoclastic release of bone derived factors (BDFs) such as transforming growth factor beta of which bone is a major reservoir[35]. In the HCA, we use TGF-β as a representative BDF given its known biphasic effects on cell behavior and its concentration dependent ability to modulate preosteoblast proliferation and maturation to bone forming osteoblasts[36-40]. We defined the roles and interactions of these key cellular populations and the factors that govern their behavior during the remodeling process using parameters derived experimentally or from the literature (Fig. 1b-c, Supp Fig. 1a and Supplementary Tables 1-6). It is important to note that each cell in the HCA behaves as an autonomous agent that can respond to surrounding environmental cues independently. In our HCA model, new bone remodeling events are initiated over time at randomly selected locations such that multiple BMUs may be present at a given time as opposed to our previous HCA model[27,41-43]. We demonstrated that each BMU undergoes five key phases of bone remodeling: initiation,

138 resorption, reversal, formation, and quiescence[44] ultimately returning to homeostasis (Fig.
139 2 and Supplementary Video 1). We also observed that each simulation (n = 25) generated
140 multiple BMUs over time, resulting in the replacement of the majority of the bone over a
141 four-year period (Fig. 2, Supplementary Video 1, Supplementary Fig. 1). We also noted
142 that while the bone area to total area (BA/TA) remains relatively constant the shape of
143 the trabecular bone changes, underscoring the dynamic nature of HCA model and how it
144 reflects the *in vivo* scenario.
145
146 **The HCA model captures dose-dependent effects of BDF and RANKL**
147 To challenge the robustness of our bone remodeling HCA, we altered the levels of key
148 factors controlling bone homeostasis. Our *in vitro* experimental data show that
149 neutralizing TGF-β or addition of exogenous TGF-β in osteoblastic cell cultures increases
150 and decreases mineralization respectively, a finding that is consistent with the
151 literature[35,40,45] (Supplementary Fig. 2a). Similarly, lowering TGF-β levels *in silico* led to a
152 dramatic increase in bone volume (Supplementary Fig. 2b-e). Interestingly, the HCA
153 results showed that when TGF-β levels dropped below 90%, there was significant bone
154 loss (Supplementary Fig. 2b-e) due to abrogation of MSC proliferation leading to reduced
155 numbers of preosteoblasts that contribute to bone formation (Supplementary Fig. 2e).
156 These data are reflective of the known biphasic roles of TGF-β on cell behaviors and
157 processes at high and low concentrations[35,40,45]. In addition, we demonstrated the
158 sensitivity of OC formation in the HCA model in response to changes in RANKL levels
159 (Supplementary Fig. 2f-h). These data demonstrate that the complex HCA model can
160 integrate the behaviors and responses of multiple highly coupled cell types and stimuli to
161 achieve responses reflective of known biology.
162
163 **The HCA model integrates the impact of standard of care therapies on bone**
164 **remodeling.**
165 Next, we assessed the response of the HCA model to standard of care therapies used
166 for the treatment of MM such as zoledronate (ZOL) and bortezomib (BTZ). These
167 compounds can block osteoclast function and formation respectively but, as we and
168 others have shown, they can also stimulate osteoblast mediated bone formation[46-49]

169 (Supplementary Fig. 3a-b and Supplementary Fig. 4a-b). Our results show that, as
170 expected, both ZOL and BTZ therapy increased bone volume over the treatment period
171 by enhancing osteoblastic bone formation and blocking osteoclast activity/formation
172 (Supplementary Fig. 3c-h, Supplementary Fig. 4c-h). While osteoclasts are impacted by
173 both treatments, the HCA recapitulates their distinct mechanisms of action showing that
174 ZOL targets actively resorbing osteoclasts as demonstrated by a reduction in bone
175 resorption per OC (Supplementary Fig. 4h) while BTZ limits the fusion of osteoclast
176 precursors as shown by a reduction in cumulative osteoclast numbers with treatment
177 (Supplementary Fig. 3g). Collectively, these data demonstrate the ability of our HCA
178 model to capture normal bone remodeling over extended periods and the appropriate
179 response of the model to applied therapeutics used for the treatment of MM.
180
181 **The HCA model incorporates the MM-bone ecosystem vicious cycle.**
182 A key component of MM growth involves the initiation of a feed-forward vicious cycle
183 leading to reduced bone formation and enhanced osteoclastic bone destruction (Fig. 1a).
184 MM is also known to interact with several cellular components of the bone ecosystem
185 such as MSCs[2,16]. To incorporate these effects and MM growth characteristics into the
186 HCA, mice were inoculated with U266-GFP MM cells and at end point, bones were
187 processed and stained for proliferation (Histone H3 phosphorylation (pHH3)) and
188 apoptosis markers (Terminal deoxynucleotidyl transferase dUTP nick end labeling
189 (TUNEL)). Our data show that the highest proportion of proliferating MM cells are located
190 within 50μm of bone (Fig. 3a-b). We noted that fewer cells (TUNEL+) underwent
191 apoptosis in this area (Fig. 3c-d) highlighting the protective effect of BDFs being
192 generated from bone degradation. To consider the effect of bone marrow stromal cells on
193 MM cells distal from bone, we performed *in vitro* experiments and found a significant
194 increase in the proliferation of MM cells grown in the presence of conditioned medium
195 from MSCs and preosteoblasts, but not osteoblasts (Fig. 3e-f). To integrate these
196 observations into the HCA, we assume that the intrinsic rate of MM cell division increases
197 with BDF and when a preosteoblast or MSC is near the MM cells (Fig. 3g-h and
198 Supplementary Equation 11).

199 Next, to study the interactions of the MM-bone marrow microenvironment in the
200 HCA model, we initialized each simulation with a single MM cell near a newly initiated
201 bone remodeling event and the formation of an osteoclast. This assumption is a
202 simplification of the colonization process, in which rare colonizing myeloma cells migrate
203 to the endosteal niche[50,51]. The HCA model revealed exciting temporal dynamics where
204 MM promotes successive phases of bone destruction mediated by osteoclasts that in turn
205 drives MM growth, thereby successfully recapitulating the vicious cycle (Supplementary
206 Fig. 4a and Supplementary Video 2). As expected, the mathematical model demonstrated
207 increasing tumor burden over time (Fig. 4a-b) with rapid loss of bone, correlating inversely
208 with tumor burden (Fig. 4c-d). These findings are consistent with *in vivo* data obtained
209 from the U266-GFP mouse model of MM which showed increasing levels of GFP positive
210 cells in the bone marrow following *ex vivo* flow cytometric analysis (Fig. 4e) combined
211 with a rapid onset of trabecular bone loss (BV/TV; Fig. 4f-g) and associated trabecular
212 bone parameters as assessed by high resolution μCT (Supplementary Fig. 5). The
213 similarities in trends between the *in vivo* model and the HCA outputs, indicated that the
214 HCA model was accurately recapitulating the MM-bone vicious cycle.
215 Furthermore, the spatial and temporal nature of the HCA allowed us to make
216 several observations: 1) In the model, the recruitment of MSCs *in silico* increases over
217 time (Fig 5a) as we and others have previously reported[52,53], 2) the model accurately
218 shows a suppression of adult osteoblast formation (Fig. 5b) due to inhibition of
219 differentiation by MM[2,54], and 3) the model predicts an early increase in preosteoblasts
220 followed by a reduction in numbers (Fig. 5c), consistent with previous reports[55], while
221 there is a concomitant increase in osteoclasts (Fig. 5d) [2,54]. We also compared these
222 population dynamics with our *in vivo* model. In tissue sections derived the U266-GFP
223 model from various time points (days 10, 40 and 100), we measured MSC, preosteoblast,
224 osteoblast, and osteoclast content and observed strong agreement with cell population
225 trends generated by the MM HCA (Fig. 5e-h and Supplementary Fig. 6). Taken together,
226 these data demonstrate the ability of the MM HCA to capture the vicious cycle of MM
227 progression in the bone microenvironment over time.
228

229 **Environment-mediated drug resistance increases minimal residual disease and**
230 **leads to higher relapse rates**
231 We and others have shown that BTZ demonstrates a dose dependent cytotoxic effect on
232 MM (Supplementary Fig. 3a)[56,57]. The compound is also effective *in vivo* but MM still
233 grows albeit at a significantly slower rate[56]. Patients also typically become refractory to
234 BTZ. This indicates that MM cells are 1) protected by the surrounding bone ecosystem,
235 or 2) due to selective pressure and mutation or other mechanisms such as epigenetic
236 changes, drug resistant clones emerge, or 3) that both ecological and evolutionary
237 contributions can occur in parallel. Here we sought to use the spatial nature of the HCA
238 model to gain a deeper understanding of how MM resistance evolves focusing initially on
239 the contribution of bone ecosystem, i.e., EMDR. We confirmed the EMDR protective
240 effect conferred by bone stromal cells on MM in the presence of BTZ *in vitro* (Fig. 6a) and
241 integrated this effect into the HCA model (Fig. 6b). BDF was also included since it can
242 provide a survival advantage to MM cells in the presence or absence of treatment[58,59].
243 Next, we initialized HCA simulations with a homogeneous sensitive MM population. BTZ
244 was applied once the tumor burden reached a volume of 10% to mimic the scenario of
245 diagnosis in the clinical setting. Our results show that without EMDR, BTZ completely
246 eradicated the disease at high doses (Fig. 6d, Supplementary Fig. 3j), consistent with our
247 *in vitro* findings. However, when EMDR effects are included in the model, BTZ reduced
248 MM burden significantly, but the disease persisted at a stable, albeit lower, level and did
249 not grow over time compared to existing *in vivo* data (Fig. 6c-d). These data suggest that
250 EMDR does not directly contribute to MM relapse but does protect a small volume of MM
251 cells from BTZ. Therefore, to address the relapse and the emergence of BTZ resistance
252 in MM cells, we integrated a resistance probability ($p\Omega = 10^{-4}$ or $p\Omega = 10^{-3}$) during cell
253 division, which allowed for the emergence of BTZ resistance. The probability of a MM cell
254 to develop resistance to BTZ are estimated based on the current literature, in which
255 mammalian cancer cells have a probability of developing resistance to numerous
256 treatments of between 10^{-3} to 10^{-6} [60,61]. Based on our *in vitro* observations, we also
257 incorporated a cost of resistance[62] in the model such that BTZ-resistant cells proliferate
258 at a slower rate and are out-competed by PI-sensitive cells in the absence of treatment
259 (Supplementary Fig. 7).

260 We then repeated our *in-silico* experiments and observed that with the lower resistance
261 probability ($p_\Omega = 10^{-4}$), EMDR increased the likelihood of tumor progression with more
262 simulations likely to relapse (54.4%, n = 125) compared to tumors without EMDR (6.4%,
263 n = 125; Fig. 6e and g; Supplementary Video 3). Similarly, with a higher resistance
264 probability ($p_\Omega = 10^{-3}$) tumors were more likely to relapse when EMDR is present (100%,
265 n = 25) compared to tumors without EMDR (56%, n = 25, Fig. 6f and h; Supplementary
266 Video 4). However, the higher resistance probability also increased the likelihood of tumor
267 progression regardless of EMDR, implying a greater role for MM intrinsic resistance
268 mechanisms during tumor relapse. To strengthen these findings, we tested a more
269 clinically relevant treatment strategy, in which BTZ therapy was pulsed (2 weeks on, 1
270 week off) and observed similar results (Supplementary Fig. 8). To validate our *in silico*
271 results, we utilized both *in vitro* and *in vivo* methodology. To this end, U266 MM cells were
272 cultured alone (monocultures) or with protective human MSCs (huMSCs) and exposed to
273 vehicle or BTZ. BTZ-treated U266 groups, responded to BTZ as evidence by a reduction
274 in MM confluency (Fig. 6j). However, we observed that BTZ was less efficient when U266
275 were cultured with huMSC and recovered over a 30-day period, whereas monocultures
276 did not. Further, co-cultured U266 cells treated with a second dose of BTZ, continued to
277 proliferate, even beyond initial confluency, and thus were considered "relapsed", whereas
278 this was not the case in monocultures (Fig. 6K). Since the propensity of MM cells to
279 develop resistance cannot be readily manipulated, we repeated the *in vitro* experiments
280 with a mixed population of MM cells that were either sensitive (U266; YFP positive) or
281 resistant (U266-PSR; RFP positive). In cultures composed of 90% PI-sensitive U266,
282 10% PI-resistant U266-PSR, we observed that MSCs protect against BTZ, leading to
283 enhanced relapse compared to MM cells cultured alone thus confirming our *in silico*
284 observations. Next, we investigated the role of EMDR *in vivo*. Currently, there are no
285 approved stromal targeting therapies available for the treatment of MM, however, Zol is
286 frequently given to patients to inhibit osteoclast-mediated bone destruction that in turn
287 also reduces the release of BDF that promote MM survival. NSG mice were inoculated
288 with 90% PI-sensitive U266-GFP-Luc and 10% PI-resistant-RFP MM cells. Upon
289 detection of the tumors in the hindlimbs, mice were divided in to two groups and
290 pretreated with either vehicle or Zol for one week to limit osteoclast-mediated release of

291 BDFs. Following pretreatment, mice were further subdivided and treated with BTZ only or
292 BTZ and Zol for another week. As predicted by our *in-silico* results, limiting EMDR with
293 Zol led to a deeper response to BTZ in PI-sensitive MM, as evidence by bioluminescence
294 imaging and end point flow cytometry (Fig 6n-o).
295 Our HCA model revealed during BTZ application, EMDR protected a reservoir of sensitive
296 cells that ultimately develops intrinsic resistance leading to the increased relapse rates
297 observed (Fig. 8a-b; Supplementary Fig. 9a). The role of this sensitive reservoir in relapse
298 is particularly evident at the lower resistance probability, where tumors with EMDR
299 exhibited more variable (generally longer) relapse times compared to tumors without
300 EMDR. When EMDR is absent, many tumors go extinct and relapse only occurs if
301 intrinsic resistance arises early following treatment, whereas with EMDR, sensitive cells
302 persist, and resistance can arise later in the course of the disease. We validated this
303 finding *in vitro,* where we demonstrate that MSCs protect a small portion of PI-sensitive
304 U266 MM cells from BTZ treatment, whereas in cultures containing only MM cells, PSR-
305 RFP MM cells ultimately became the sole clone upon relapse following BTZ treatment
306 (Fig 7c-d). Further, *in vivo*, treatment of mice with BTZ, led to the outgrowth of PI-resistant
307 PSR-RFP. However, in Zol-pretreated (EMDR-inhibited) mice we see a deeper reduction
308 in PI-sensitive MM cells compared to BTZ-only treated mice, where EMDR is intact (Fig.
309 7e-f). We next determined the clinical relevance of whether PI sensitive MM cells existed
310 in patients that were considered to have relapsed refractory MM (RRMM). We isolated
311 CD138+ cells from MM and exposed the cells to BTZ *ex vivo*. We observed that
312 approximately 20% of relapsed refractory MM patients who a failed a PI-containing
313 regimen (n=86) contained MM cells that are still sensitive to PI treatment thus supporting
314 our *in silico* and *in vitro* and *in vivo* findings. Taken together, these results demonstrate
315 the ability of the HCA to predict the effect of resistance and EMDR on tumor relapse and
316 indicate a vital role of EMDR in contributing to minimal residual disease and the
317 development of relapse refractory MM.
318
319 **Environment-mediated drug resistance and resistance probability impact MM**
320 **heterogeneity in relapsed disease**

321 Even though relapsed tumors with a high resistance probability had similar growth
322 dynamics with and without EMDR, we noted that the composition of the tumors differed
323 greatly. Myeloma is a clonal disease with the prevalence of clones changing throughout
324 treatment[23,50,63,64]. Given the spatial resolution of the HCA model, we next asked whether
325 EMDR impacted the heterogeneity of resistant tumors. To this end, we tracked the
326 number and spatial localization of new clones forming from unique resistance events
327 under BTZ treatment conditions in the presence or absence of EMDR. We observed that
328 at a high resistance probability ($p_\Omega = 10^{-3}$) EMDR drove the evolution of significantly more
329 resistant subclones (mean = 5.2 subclones with >10 cells, n = 24 simulations) compared
330 to non-EMDR conditions where the arising population was composed largely of a single
331 resistant clone (mean = 1.2 subclones with >10 cells, n = 10 simulations; Fig. 8a), with
332 similar results at lower resistance probabilities and pulsed BTZ treatment (Supplementary
333 Fig. 9b-c). *In vivo*, we observed a greater reduction in the ratio of GFP+ sensitive to RFP+
334 resistant MM when mice were treated with Zol+BTZ compared to BTZ only (Fig 8b-c).
335 Moreover, the HCA revealed a significant proportion of resistant subclones originated in
336 close proximity to MSCs/preosteoblasts (Fig. 8d) or following release of BDF from
337 osteoclastic bone resorption (Supplementary Fig. 9c). Taken together, these data would
338 indicate that EMDR not only leads to enhanced relapse, but increased MM heterogeneity
339 due to the emergence of independent resistant MM clones. Further, it is also plausible
340 that EMDR may give rise to MM clones with potentially unique intrinsic BTZ resistance
341 mechanisms making the treatment of relapsed tumors more challenging. Together, these
342 data support that early targeting of bone marrow microenvironment, and thus EMDR,
343 would lead to reduced MM heterogeneity and potentially deeper responses with
344 subsequent lines of treatments.
345

346 **Discussion**

347 Understanding the factors that govern the evolution of refractory MM remains of huge
348 clinical importance. Dissecting how intrinsic and bone ecosystem mechanisms contribute
349 to the evolution of the disease in the presence or absence of treatment or where these
350 clones arise spatially are difficult questions to address with standard experimental
351 techniques alone. Here, we address this using a novel experimentally derived hybrid

352 cellular automaton (HCA) model of MM evolution in the bone ecosystem that provides
353 new insights. For example, we show that the bone ecosystem contributes to minimal
354 residual disease, and MM clonal heterogeneity. These findings are in part supported by
355 previous studies revealing enrichment of binding proteins and chemokine receptors on
356 MM cells in minimal residual disease, indicating a likely role for stromal interactions in
357 facilitating relapse[65]. Our findings and additional wider biological validation provide
358 rationale for the targeting of the bone ecosystem during the application of standard of
359 care treatment to prevent the emergence of multiple resistant clones.

360 Our own *in vitro* and *in vivo* data, as well as data from the literature, were used
361 where possible to parameterize and calibrate the HCA model. However, there were some
362 parameters that could not be estimated, and the specific assumptions that have been
363 incorporated into the HCA may impact the generality of the results. For example, we
364 assume that MSCs are recruited in proportion to tumor burden based on experimental
365 data in non-treatment conditions, but the application of treatment could alter this
366 recruitment rate and thus bone ecosystem protective effects. Furthermore, there are
367 limitations to how well parameters estimated from *in vitro* data correspond to the *in vivo*
368 setting. To address this, we tested the robustness of the model results by varying a subset
369 of parameter values to determine the impact on simulation results (Supplementary
370 Methods 1.4; Supplementary Fig. 10). Overall, our finding that EMDR increases minimal
371 residual disease and leads to higher relapse rates was consistent across parameter
372 values, underscoring the robustness of the model.

373 There have been several mathematical models that explore interactions between
374 MM and the bone marrow microenvironment. For example, ordinary differential equation
375 (ODE), evolutionary game theory (EGT), and hybrid agent-based models have revealed
376 insights into MM growth in bone and have even taken into consideration the impact of
377 MM progression on bone destruction[66-72]. Additionally, mathematical models have
378 focused on how ecosystem effects contribute to drug resistance[73-76]. However, the HCA
379 model presented herein represents a significant advance in that it is carefully integrated
380 with biological data to recapitulate the bone-MM ecosystem under normal and treatment
381 conditions and is the first model to dissect intrinsic vs. ecosystem driven resistance in
382 multiple myeloma. A major additional advantage of our model is its spatial nature, allowing

us to visualize and measure where the ecosystem, and particularly stromal cells, contribute to the generation of resistant clones.

Our model shows that resistant MM clones can arise independently of the bone ecosystem during BTZ treatment if the resistance probability is sufficiently high. But, when EMDR is present, we observe the evolution of higher numbers of resistant clones near MSCs/preosteoblasts/BDF during continuous BTZ treatment. The model also suggests that targeting of EMDR during treatment would reduce MM heterogeneity. Various adhesion molecules and cytokines such as the CXCL12/CXCR4 and IL-6/JAK/STAT axis have been shown to mediate ecosystem protective effects and drugs/biologics that specifically target those pathways have been trialed[77,78]. Unfortunately, these drugs have had little success translating to clinical practice due to limited survival improvements when added to existing therapies[79], thus there remains a need to identify multiple mechanisms of EMDR in patients with novel therapies and feasible methods of delivering these drugs. However, we posit that early intervention with EMDR-targeting agents, perhaps in combination, would reduce tumor heterogeneity, rendering relapsing tumors vulnerable to a targeted second line therapy that targets the predominantly homogenous disease. As such, future studies/trials should take into consideration the tumor diversity upon relapse and response to second line therapies.

Another important aspect of the model is the ability to apply and withdraw therapy at varying stages of MM progression to quantitatively determine the impact on MM over time which may be useful for adaptive therapy design and implementation. Adaptive therapy is an emerging, evolution-inspired approach for cancer treatment that exploits competitive interactions between drug sensitive and drug resistant cells to maintain a stable tumor burden[62]. Several models have studied the many ways therapies can be applied in an adaptive manner ensuring that the competition between treatment resistant and naïve populations allows for better overall survival for cancer patients. Importantly, our model captures tumor interactions with the bone ecosystem and thus includes the potential impact of the bone ecosystem on adaptive therapy. This allows us to study not only how treatments impact tumor populations but also their influence on bone ecosystem cells such as osteoblasts and osteoclasts, and how this can then influence MM response since the protective bone microenvironment can serve as a reservoir of sensitive cells

414 under treatment. Clinical trials thus far using adaptive therapy guided by mathematical
415 modeling have had encouraging results. For instance, recent studies have shown that in
416 patients with bone metastatic prostate cancer, adaptive therapies guided by mathematical
417 models can increase the time to progression and the overall survival using standard of
418 care treatments[80]. These data support the feasibility of integrating mathematical modeling
419 for the design of patient specific treatment. It should be noted however, the HCA model
420 is parameterized with a variety of in vitro, in vivo, and human data, making translation
421 directly to the clinic challenging in its current form. This can be resolved with further
422 rigorous model calibration and validation using clinical data, and multiple efforts at moving
423 agent-based models into the clinical setting are underway[29-31,81,82].

424 A key component of our HCA model lies in its ability to recapitulate the homeostatic
425 nature of bone remodeling over prolonged periods (~4 years). As we demonstrated, the
426 impact of therapies on tumor-naïve bone volume and the bone stromal cellular
427 components that control the process can also be quantitatively examined. It also can
428 examine non-cancerous bone diseases that result from an imbalance in bone remodeling
429 such as osteoporosis[83]. The underlying causes of osteoporosis can result in differing
430 effects on osteoclasts and osteoblasts, which could be incorporated into the model. For
431 example, estrogen deficiency increases the lifespan of osteoclasts while having the
432 opposite effect on osteoblasts, whereas age-related senescence is characterized by
433 decreased osteoclastogenesis and osteoblastogenesis[83]. Osteoporosis treatments
434 include anti-resorptive therapies (e.g., bisphosphonates) and bone formation therapies
435 (e.g., intermittent PTH). By modifying certain model parameters, we can explore the effect
436 of different therapeutic strategies on disease outcomes to determine if certain treatments
437 are more effective in particular scenarios[84]. While we have primarily used Zol and BTZ
438 for proof of principle, the model can be easily adapted to integrate the effects of other
439 standard of care therapies as single agents or in combination such as dexamethasone,
440 and IMIDs. Importantly, the temporal and cellular resolution of the model also can identify
441 key moments in which to administer treatments to maintain a healthy bone volume.

442 Our HCA model, like all models, has caveats. For example, its two-dimensional
443 nature does not take into account the potential three-dimensional role in evolutionary
444 dynamics[85,86] or the vascular nature of the bone marrow-MM microenvironment that can

445 play a role in drug/nutrient diffusion,[10,87]. However, these can be incorporated into the
446 model, if necessary, upon availability of relevant experimental data. Another potential and
447 future extension of the model is to incorporate the immune ecosystem given its role in
448 controlling bone turnover and cancer progression[10,87], the influence of BDFs on immune
449 populations[88,89] and the growing armamentarium of immunotherapies in MM. Here, we
450 excluded the immune component to focus solely on the role of the bone stroma on MM
451 progression combined with the fact that MM growth in immunocompromised mice was
452 used to parameterize and compare model outputs. Infiltrating immune cells have noted
453 effects on cancer progression. For example, initially, natural killer (NK) cells and cytotoxic
454 T lymphocytes can drive an anti-tumor response[90]. However, as the tumor progresses,
455 immunosuppressive populations expand including myeloid derived suppressor cells
456 (MDSCs) and regulatory T-cells (Tregs)[90]. MM is characterized by an increase of inactive
457 NK cells, MDSCs, and Tregs and treatments such as bortezomib can alter the
458 composition and activity of infiltrating or resident immune cells[90,91]. Tumor-immune
459 dynamics in MM have been previously explored with ODE models[92,93] and parameters
460 derived from *in vitro* or *in vivo* studies can be integrated into our HCA model albeit with a
461 limit on complexity. Another caveat is the difficulty in determining the rate of MM
462 resistance and the assumption that it occurs intrinsically due to treatment pressure. Prior
463 studies suggest that drug resistance may arise through the selective expansion of pre-
464 existent resistant tumor cells, *de novo*, or through the gradual increase in resistance over
465 time[94]. In our model, we assume that after treatment initiates (i.e., once the bone marrow
466 consists of 10% of MM cells), there is a probability that a dividing MM cell could develop
467 a resistance mechanism, and that mechanisms directly causes resistance to bortezomib
468 resulting in heterogeneity. This resistance probability that would lead to treatment
469 resistance is difficult to assess in patients or in experimental models but the resultant
470 heterogeneity arising from different resistance probabilities may allow us to infer
471 resistance rates in patients. Moreover, the *in silico* model is not fixated on specific
472 resistance mechanisms currently but more on whether a cell is sensitive or not. One such
473 benefit of the *in silico* model is the ability to alter parameters, such as p_{Ω}, response to
474 treatment and doubling time, to mimic the heterogeneity seen in the clinic.

475 In conclusion, we have described a new mathematical model of MM evolution in
476 the context of the bone ecosystem. Our results show that, under treatment conditions, the
477 interactions between the bone ecosystem and the tumor contributes to the presence of
478 residual disease and to the enrichment of tumor heterogeneity. These results suggest
479 that early intervention with drugs that target the bone ecosystem could lead to MM
480 extinction or at the very least reduce tumor heterogeneity by preventing the evolution of
481 multiple drug resistant clones. Given the current interest in novel strategies of treatment
482 that consider the evolutionary dynamics in cancer such as adaptative therapies, we also
483 predict that our model can be a useful clinical tool in guiding patient specific treatment
484 strategies.
485
486 **Methods**
487 **Hybrid Cellular Automaton Model**
488 The model we developed builds on the HCA paradigm first described by Anderson *et al.*
489 and used to study evolutionary dynamics in cancer and our work in the context of bone
490 metastasis[41-43,95,96]. By definition, an HCA consists of discrete cell types that are updated
491 once per time step according to a set of flow charts (Fig. 1c) as well as a set of partial
492 differential equations that describe cytokines in the microenvironment. Here, we consider
493 six different cell types, including precursor osteoclasts, active osteoclasts, mesenchymal
494 stem cells (MSCs), precursor osteoblasts, active osteoblasts, and multiple myeloma cells.
495 Additionally, we incorporate two signaling molecules including RANKL and bone derived
496 factors (BDFs) such as transforming growth factor beta (TGF-β). In the sections below,
497 we describe the interactions between cell types and cytokines that are key in bone
498 remodeling and MM progression. Further details can be found in Supplementary Methods
499 1.
500 *Parameters and grid*
501 We implemented our model using the Hybrid Automata Library (HAL)[97]. When possible,
502 parameters for the HCA model were derived from empirical and published data
503 (Supplementary Tables 1-6). The model is defined on a 2D rectangular grid (160 x 150
504 pixels) representing a $1600 \times 1500\ \mu m^2$ cross section of the bone marrow. Trabecular
505 bone is defined in the center of the grid and initially consists of 12.9% of the total area,

506 consistent with our *in vivo* data (Supplementary Methods 1.1). Normal bone remodeling
507 events are uniformly distributed over 4 years, the approximate turnover time of trabecular
508 bone[83]. A remodeling event is initiated by the expression of RANKL by five osteoblast
509 lineage cells on the perimeter of the bone.

510 *Preosteoclasts and osteoclasts*

511 Precursor osteoclasts follow the gradient of RANKL to the bone remodeling site. With a
512 given probability, at least five preosteoclasts will fuse together to become a
513 multinucleated osteoclast. Active osteoclasts resorb bone matrix, leading to the release
514 of BDF. We assume that the amount of bone that osteoclasts resorb is proportional to
515 their lifespan of approximately 14 days[83,98].

516 *MSCs, preosteoblasts, and osteoblasts*

517 After an osteoclast fuses, an MSC is placed on the grid within a radius of $40\ \mu m$ of the
518 osteoclast, provided there is not already an MSC within the neighborhood. This
519 requirement ensures that MSCs are located adjacent to sites of bone remodeling and can
520 couple bone resorption with bone formation[36]. MSCs undergo asymmetrical division to
521 create preosteoblasts, which proliferate when BDF is above a certain threshold or
522 differentiate into bone matrix-producing osteoblasts when BDF is below the threshold
523 (Supplementary Fig. 2c). We assume that osteoblast lifespan is proportional to the
524 amount of bone that was resorbed at the location of the osteoblast, which is approximately
525 3 months. In the model, we assume that osteoblast death is proportional to the amount
526 of bone that was resorbed by the osteoclast subunit that had occupied the space. Whilst
527 this is a simplifying assumption of the biology, this assumption permits the coupling of
528 bone resorption with bone formation, since the lifespan of an osteoblast controls how
529 much bone the osteoblast forms. Bone resorption and bone formation are tightly coupled
530 processes[99]. The definitive mechanisms through which osteoclasts and osteoblasts
531 sense each other and their catabolic/anabolic processes have still not been fully
532 elucidated and can be context dependent. However, several mechanisms are known to
533 play a role including the release of bone derived factors (BDFs; namely TGF-beta and
534 IGF-1), osteoclast derived factors such as sphingosine 1-phosphate, extracellular
535 vesicles, apoptotic bodies containing RANK, and demineralized collagen remnants in the
536 resorption lacunae. To model each of these mechanisms independently would make our

model very complex as well as computationally expensive. We therefore integrated a straightforward coupling of osteoblasts and osteoclasts in the model. Further, when an osteoblast is buried, this has consequences for bone homeostasis. To maintain a steady state of bone, the lifespan of the nearest osteoblast is increased to allow it to build more bone to compensate for the amount lost due to the buried osteoblast. Whilst this is a simplifying assumption, research suggests osteoblast lineage cells communicate through gap junctions. This allows osteoblasts to coordinate activities and ensure new bone tissue is deposited at the correct location and in the appropriate amount to maintain structural integrity and bone homeostasis[100-104].

Cytokines

RANKL (R_L) and BDF (T_β) are two key cytokines that drive the normal bone remodeling process. RANKL is produced by osteoblast lineage cells ($\alpha_R B_{i,j}$) with natural decay of the ligand ($\delta_R R_L$). BDF is released during bone resorption ($\alpha_T B_{i,j} C_{i,j}$) with natural decay of the ligand ($\delta_T T_\beta$). We also assume that there is a constant production of BDFs (α_B) by other cell types that are not explicitly defined in the model. These cytokines are incorporated into our model through the following system of partial differential equations (PDEs):

$$\frac{\partial R_L(x,y,t)}{\partial t} = \underbrace{D_R\left(\frac{\partial^2 R_L}{\partial x^2} + \frac{\partial^2 R_L}{\partial y^2}\right)}_{\text{Diffusion}} + \underbrace{\alpha_R B_{i,j}}_{\text{Production}} - \underbrace{\delta_R R_L}_{\text{Decay}}$$

$$\frac{\partial T_\beta(x,y,t)}{\partial t} = \underbrace{D_T\left(\frac{\partial^2 T_\beta}{\partial x^2} + \frac{\partial^2 T_\beta}{\partial y^2}\right)}_{\text{Diffusion}} + \underbrace{\alpha_B}_{\text{Basal Production}} + \underbrace{\alpha_T B_{i,j} C_{i,j}}_{\text{Production}} - \underbrace{\delta_T T_\beta}_{\text{Decay}}$$

where the subscripts specify the location on the grid, i.e., $x = ih$, $y = jh$ where $\{i, j\}$ are positive integers and h denotes the spatial step, $h = \Delta x = \Delta y$. The system of PDEs is solved using the forward time centered space (FTCS) scheme with periodic boundary conditions imposed on all sides of the domain, which is implemented using the diffusion function in HAL.

Multiple Myeloma

A single myeloma cell is recruited within a radius of $40\ \mu\text{m}$ of an osteoclast after the first osteoclast fusion event occurs (Fig. 4a). MM cells move and proliferate in response to

564 BDF and have a further proliferative advantage if they are within a radius of $20\ \mu\mathrm{m}$ of an
565 MSC or preosteoblast (Fig. 3g), and a survival advantage if BDF is above a certain
566 threshold (Fig. 3h). As the MM cell population increases, additional MSCs are recruited.
567 Furthermore, if three or more myeloma cells are located close to bone, a new bone
568 remodeling event is initiated which increases RANKL and osteoclast formation. MM cells
569 also prevent the differentiation of preosteoblasts if they are located within a radius of
570 $80\ \mu\mathrm{m}$ of a MM cell which decreases osteoblast activity.

571 *Treatment*

572 The HCA incorporates the direct and indirect effects of bortezomib by including the
573 cytotoxic effect on MM cells as well as its ability to inhibit preosteoclast fusion and
574 enhance bone formation[48,49] (Supplementary Fig. 3). To mimic the clinical scenario of MM
575 diagnosis, once MM reaches 10% of the bone marrow area *in silico*, treatment is applied
576 either continuously (as for mouse models of multiple myeloma) or pulsed (2 weeks on, 1
577 week off; as is performed in the clinic) until MM burden reaches 20% of the bone marrow.
578 In these simulations, once treatment is initiated, myeloma cells have a probability of
579 developing resistance mechanisms during cell division that would cause the MM cells to
580 become resistant to bortezomib. MM cells that are within a radius of $20\ \mu\mathrm{m}$ of an MSC or
581 preosteoblast or are located at a position where BDF is above a certain threshold, have
582 a survival advantage during treatment referred to as environment mediated drug
583 resistance (EMDR).

584 **Multiple myeloma mouse models**

585 All animal experiments were performed with University of South Florida (Tampa, FL)
586 Institutional Animal Care and Use Committee approval (CCL; #7356R). Male and female
587 14–16-week-old immunodeficient mice NOD-SCIDγ (NSG) mice were divided into tumor
588 naïve or tumor bearing mice GFP-expressing human U266 (U266-GFP) multiple
589 myeloma cells were injected (5×10^6cells/100μL PBS) or PBS (100μL) via tail vein. Mice
590 were euthanized at days 3, 10, 20, 40 and 100 (3-5/group/timepoint). In a separate
591 experiment male and female 8 week-old NSG mice were inoculated with PI-sensitive
592 U266-GFP-Luc (90%) and PI-resistant PSR-RFP (10%) MM cells via tail vein injection
593 (5×10^6cells/100μL PBS). Upon detection of tumor burden in the hind limbs via

594 bioluminescent imaging (IVIS), mice were randomized to two groups to receive either
595 twice weekly vehicle (PBS) or Zol (30µg/kg). Following one week of Zol pretreatment,
596 mice were further randomized in to four subgroups and received the following: Group 1
597 Vehicle (5 mice), Group 2 Zol (30µg/kg/twice weekly; 5 mice), Group 3 Zol+BTZ (7 mice),
598 Group 4 BTZ (0.5mg/kg/twice weekly; 4 mice). After one week of BTZ treatment, all mice
599 were euthanized. Tibiae were excised and soft tissue removed for histological and FACs
600 analyses.

601 **Micro-computed Tomography, Immunofluorescence and Histomorphometry,**
602 Harvested right tibiae were fixed in 4% paraformaldehyde (PFA) in 1x phosphate buffered
603 saline (PBS) for 48 hours at room temperature. Evaluation of trabecular bone
604 microarchitecture was performed in a region of 1000 µm, beginning 500µm from the
605 growth plate using the SCANCO µ35CT scanner. Tibiae were decalcified in an excess of
606 10% EDTA at pH 7.4 at 4°C for up to three weeks with changes every 3 days before being
607 place in cryoprotection buffer (30% sucrose), frozen in cryomedium (OCT) and subjected
608 to cryosectioning to yield 20 µm tissue sections. Sections were dried, washed and blocked
609 before addition of primary antibodies (anti-pHH3; 06-570 Millipore, anti-Osterix; ab22552,
610 abcam: anti-αSMA: PA5-16697, Invitrogen). Slides were washed and incubated with
611 goat anti-rabbit Alexa Fluor-647-conjugated secondary antibody and counterstained with
612 DAPI. Mounted sections were imaged using 10X image tile-scans of whole tibia. pHH3+,
613 αSMA+, Osterix+ or GFP+ cells were identified and quantified using Fiji software[105]. Dual
614 ALP and TRAcP staining were performed on cryosections. Brightfield visualization was
615 performed using the EVOS auto at 20X magnification. Five images per section were taken
616 and the number of ALP+ cuboidal bone-lining osteoblasts and red multinucleated
617 TRAcP+ osteoclasts per bone surface were calculated.
618
619 *For additional and in-depth methods, please see supplementary materials.*
620
621 **Author Contributions**
622 A.K.M and D.B. were responsible for computational model design and execution. R.T.B
623 and C.C.L were responsible for biological experimentation design and analysis**.** T.L, N.N,

J.F performed biological experiments. P.R.S, R.C, A.S and K.H.S were involved in conception, design, experimentation, and analysis of *ex vivo* samples. A.K.M, R.T.B, C.C.L and D.B were involved in overall concept and design. All authors were involved in data interpretation, manuscript writing and editing.

Acknowledgements

The authors would like to thank the patients at H. Lee Moffitt Cancer Center who provided clinical samples for *ex vivo* assays as well as consented to access to their clinical data through the Total Cancer Care database. In addition, the authors thank, Marilena Tauro, Tatiana Miti, Malgorzata Tyczynska, Mark Robertson-Tessi and Etienne Baratchart, at Moffitt Cancer Center for insightful discussions over the years and with editing and revision of manuscript. This work has been supported in part by the Small Animal Imaging Laboratory (SAIL) and the Flow Cytometry, and Analytical Microscopy Core Facilities at the Moffitt Cancer Center, an NCI designated Comprehensive Cancer Center (P30-CA076292). This work was supported in part by funds from the NCI PSON (5U01CA244101), Physical Sciences in Oncology (PSOC) Grant 1U54CA193489-01A1 (to K.H.S., A.S, and others), H. Lee Moffitt Cancer Center's Team Science Grant (A.S., K.H.S.), Miles for Moffitt Foundation (A.S.). Additionally, this work was supported by personal donations from The Pentecost Myeloma Research Center.

Data availability statement

All the data supporting the findings of this study are available within the article and its Supplementary information files and from the corresponding author upon reasonable request. A reporting summary for this article is available as a Supplementary Information file. Source data are provided with this paper.

Code availability statement

The code generated in this manuscript is available at https://github.com/dbasanta/MM_ABM

655 **References:**

656 1. Howlader N, N.A., Krapcho M, Miller D, Brest A, Yu M, Ruhl J, Tatalovich Z,
657 Mariotto A, Lewis DR, Chen HS, Feuer EJ, Cronin KA SEER Cancer Statistics
658 Review, 1975-2016, National Cancer Institute. (2019).
659 2. Galson, D.L., Silbermann, R. & Roodman, G.D. Mechanisms of multiple myeloma
660 bone disease. *Bonekey Rep* **1**, 135 (2012).
661 3. Roodman, G.D. Pathogenesis of myeloma bone disease. *J Cell Biochem* **109**, 283-
662 291 (2010).
663 4. Cowan, A.J.*, et al.* Diagnosis and Management of Multiple Myeloma: A Review.
664 *JAMA* **327**, 464-477 (2022).
665 5. Abdi, J., Chen, G. & Chang, H. Drug resistance in multiple myeloma: latest findings
666 and new concepts on molecular mechanisms. *Oncotarget* **4**, 2186-2207 (2013).
667 6. Markovina, S.*, et al.* Bone marrow stromal cells from multiple myeloma patients
668 uniquely induce bortezomib resistant NF-kappaB activity in myeloma cells. *Mol*
669 *Cancer* **9**, 176 (2010).
670 7. Meads, M.B., Gatenby, R.A. & Dalton, W.S. Environment-mediated drug
671 resistance: a major contributor to minimal residual disease. *Nat Rev Cancer* **9**,
672 665-674 (2009).
673 8. Meads, M.B., Hazlehurst, L.A. & Dalton, W.S. The bone marrow microenvironment
674 as a tumor sanctuary and contributor to drug resistance. *Clin Cancer Res* **14**, 2519-
675 2526 (2008).
676 9. Shain, K.H.*, et al.* Beta1 integrin adhesion enhances IL-6-mediated STAT3
677 signaling in myeloma cells: implications for microenvironment influence on tumor
678 survival and proliferation. *Cancer Res* **69**, 1009-1015 (2009).
679 10. Shay, G., Hazlehurst, L. & Lynch, C.C. Dissecting the multiple myeloma-bone
680 microenvironment reveals new therapeutic opportunities. *J Mol Med (Berl)* **94**, 21-
681 35 (2016).
682 11. Azab, A.K.*, et al.* Hypoxia promotes dissemination of multiple myeloma through
683 acquisition of epithelial to mesenchymal transition-like features. *Blood* **119**, 5782-
684 5794 (2012).

685 12. Uchiyama, H., Barut, B.A., Mohrbacher, A.F., Chauhan, D. & Anderson, K.C.
686 Adhesion of human myeloma-derived cell lines to bone marrow stromal cells
687 stimulates interleukin-6 secretion. *Blood* **82**, 3712-3720 (1993).
688 13. Hao, M.*, et al.* Bone marrow stromal cells protect myeloma cells from bortezomib
689 induced apoptosis by suppressing microRNA-15a expression. *Leuk Lymphoma*
690 **52**, 1787-1794 (2011).
691 14. Roccaro, A.M.*, et al.* BM mesenchymal stromal cell-derived exosomes facilitate
692 multiple myeloma progression. *J Clin Invest* **123**, 1542-1555 (2013).
693 15. Azab, A.K.*, et al.* CXCR4 inhibitor AMD3100 disrupts the interaction of multiple
694 myeloma cells with the bone marrow microenvironment and enhances their
695 sensitivity to therapy. *Blood* **113**, 4341-4351 (2009).
696 16. Di Marzo, L.*, et al.* Microenvironment drug resistance in multiple myeloma:
697 emerging new players. *Oncotarget* **7**, 60698-60711 (2016).
698 17. Edwards, C.M., Zhuang, J. & Mundy, G.R. The pathogenesis of the bone disease
699 of multiple myeloma. *Bone* **42**, 1007-1013 (2008).
700 18. Wuilleme-Toumi, S.*, et al.* Mcl-1 is overexpressed in multiple myeloma and
701 associated with relapse and shorter survival. *Leukemia* **19**, 1248-1252 (2005).
702 19. Chen, S.*, et al.* A Bim-targeting strategy overcomes adaptive bortezomib
703 resistance in myeloma through a novel link between autophagy and apoptosis. in
704 *Blood*, Vol. 124 2687-2697 (2014).
705 20. Touzeau, C., Maciag, P., Amiot, M. & Moreau, P. Targeting Bcl-2 for the treatment
706 of multiple myeloma. *Leukemia* **32**, 1899-1907 (2018).
707 21. Kumar, S.*, et al.* Efficacy of venetoclax as targeted therapy for relapsed/refractory
708 t(11;14) multiple myeloma. *Blood* **130**, 2401-2409 (2017).
709 22. Bianchi, G. & Munshi, N.C. Pathogenesis beyond the cancer clone(s) in multiple
710 myeloma. *Blood* **125**, 3049-3058 (2015).
711 23. Paino, T.*, et al.* Phenotypic identification of subclones in multiple myeloma with
712 different chemoresistant, cytogenetic and clonogenic potential. *Leukemia* **29**,
713 1186-1194 (2015).

714 24. Pasetto, S., Enderling, H., Gatenby, R.A. & Brady-Nicholls, R. Intermittent
715 Hormone Therapy Models Analysis and Bayesian Model Comparison for Prostate
716 Cancer. *Bull Math Biol* **84**, 2 (2021).
717 25. Brady-Nicholls, R.*, et al.* Predicting patient-specific response to adaptive therapy
718 in metastatic castration-resistant prostate cancer using prostate-specific antigen
719 dynamics. *Neoplasia* **23**, 851-858 (2021).
720 26. West, J.B., Dinh, M.N., Brown, J.S., Zhang, J., Anderson, A.R. & Gatenby, R.A.
721 Multidrug Cancer Therapy in Metastatic Castrate-Resistant Prostate Cancer: An
722 Evolution-Based Strategy. *Clin Cancer Res* **25**, 4413-4421 (2019).
723 27. Araujo, A.*, et al.* Quantification and Optimization of Standard-of-Care Therapy to
724 Delay the Emergence of Resistant Bone Metastatic Prostate Cancer. *Cancers*
725 *(Basel)* **13**(2021).
726 28. Gallaher, J.*, et al.* Improving treatment strategies for patients with metastatic
727 castrate resistant prostate cancer through personalized computational modeling.
728 *Clin Exp Metastasis* **31**, 991-999 (2014).
729 29. Macklin, P., Edgerton, M.E., Thompson, A.M. & Cristini, V. Patient-calibrated
730 agent-based modelling of ductal carcinoma in situ (DCIS): from microscopic
731 measurements to macroscopic predictions of clinical progression. *J Theor Biol*
732 **301**, 122-140 (2012).
733 30. Gallaher, J.A.*, et al.* From cells to tissue: How cell scale heterogeneity impacts
734 glioblastoma growth and treatment response. *PLoS Comput Biol* **16**, e1007672
735 (2020).
736 31. Alfonso, J.C.L.*, et al.* Tumor-immune ecosystem dynamics define an individual
737 Radiation Immune Score to predict pan-cancer radiocurability. *Neoplasia* **23**,
738 1110-1122 (2021).
739 32. Jilka, R.L. Biology of the basic multicellular unit and the pathophysiology of
740 osteoporosis. *Med Pediatr Oncol* **41**, 182-185 (2003).
741 33. Wang, L., You, X., Zhang, L., Zhang, C. & Zou, W. Mechanical regulation of bone
742 remodeling. *Bone Res* **10**, 16 (2022).
743 34. Novack, D.V. & Faccio, R. Osteoclast motility: putting the brakes on bone
744 resorption. *Ageing Res Rev* **10**, 54-61 (2011).

745 35. Janssens, K., ten Dijke, P., Janssens, S. & Van Hul, W. Transforming growth
746 factor-beta1 to the bone. *Endocr Rev* **26**, 743-774 (2005).
747 36. Tang, Y.*, et al.* TGF-beta1-induced migration of bone mesenchymal stem cells
748 couples bone resorption with formation. *Nat Med* **15**, 757-765 (2009).
749 37. Martin, T.J. & Sims, N.A. Osteoclast-derived activity in the coupling of bone
750 formation to resorption. *Trends Mol Med* **11**, 76-81 (2005).
751 38. Janssens, K.*, et al.* Transforming Growth Factor-1 to the Bone. (2005).
752 39. Wu, M., Chen, G. & Li, Y.P. TGF-beta and BMP signaling in osteoblast, skeletal
753 development, and bone formation, homeostasis and disease. *Bone Res* **4**, 16009
754 (2016).
755 40. Edwards, J.R.*, et al.* Inhibition of TGF-beta signaling by 1D11 antibody treatment
756 increases bone mass and quality in vivo. *J Bone Miner Res* **25**, 2419-2426 (2010).
757 41. Araujo, A., Cook, L.M., Lynch, C.C. & Basanta, D. Size Matters: Metastatic cluster
758 size and stromal recruitment in the establishment of successful prostate cancer to
759 bone metastases. *Bull Math Biol* **80**, 1046-1058 (2018).
760 42. Araujo, A., Cook, L.M., Lynch, C.C. & Basanta, D. An integrated computational
761 model of the bone microenvironment in bone-metastatic prostate cancer. *Cancer*
762 *Res* **74**, 2391-2401 (2014).
763 43. Cook, L.M., Araujo, A., Pow-Sang, J.M., Budzevich, M.M., Basanta, D. & Lynch,
764 C.C. Predictive computational modeling to define effective treatment strategies for
765 bone metastatic prostate cancer. *Sci Rep* **6**, 29384 (2016).
766 44. Sims, N.A. & Martin, T.J. Osteoclasts Provide Coupling Signals to Osteoblast
767 Lineage Cells Through Multiple Mechanisms. *Annu Rev Physiol* **82**, 507-529
768 (2020).
769 45. Paton-Hough, J.*, et al.* Preventing and Repairing Myeloma Bone Disease by
770 Combining Conventional Antiresorptive Treatment With a Bone Anabolic Agent in
771 Murine Models. *J Bone Miner Res* **34**, 783-796 (2019).
772 46. Pan, B.*, et al.* The nitrogen-containing bisphosphonate, zoledronic acid, increases
773 mineralisation of human bone-derived cells in vitro. *Bone* **34**, 112-123 (2004).

774 47. Zangari, M., Yaccoby, S., Cavallo, F., Esseltine, D. & Tricot, G. Response to
775 bortezomib and activation of osteoblasts in multiple myeloma. *Clin Lymphoma*
776 *Myeloma* **7**, 109-114 (2006).
777 48. Pennisi, A., Li, X., Ling, W., Khan, S., Zangari, M. & Yaccoby, S. The proteasome
778 inhibitor, bortezomib suppresses primary myeloma and stimulates bone formation
779 in myelomatous and nonmyelomatous bones in vivo. *Am J Hematol* **84**, 6-14
780 (2009).
781 49. Hurchla, M.A.*, et al.* The epoxyketone-based proteasome inhibitors carfilzomib
782 and orally bioavailable oprozomib have anti-resorptive and bone-anabolic activity
783 in addition to anti-myeloma effects. *Leukemia* **27**, 430-440 (2013).
784 50. Hewett, D.R.*, et al.* DNA Barcoding Reveals Habitual Clonal Dominance of
785 Myeloma Plasma Cells in the Bone Marrow Microenvironment. *Neoplasia* **19**, 972-
786 981 (2017).
787 51. Lawson, M.A.*, et al.* Osteoclasts control reactivation of dormant myeloma cells by
788 remodelling the endosteal niche. *Nat Commun* **6**(2015).
789 52. Jones, E.A.*, et al.* Optimization of a flow cytometry-based protocol for detection
790 and phenotypic characterization of multipotent mesenchymal stromal cells from
791 human bone marrow. *Cytometry B Clin Cytom* **70**, 391-399 (2006).
792 53. Noll, J.E.*, et al.* Myeloma plasma cells alter the bone marrow microenvironment by
793 stimulating the proliferation of mesenchymal stromal cells. *Haematologica* **99**, 163-
794 171 (2014).
795 54. Marino, S., Petrusca, D.N. & Roodman, G.D. Therapeutic targets in myeloma bone
796 disease. *Br J Pharmacol* **178**, 1907-1922 (2021).
797 55. Kassen, D.*, et al.* Myeloma impairs mature osteoblast function but causes early
798 expansion of osteo-progenitors: temporal changes in bone physiology and gene
799 expression in the KMS12BM model. *Br J Haematol* **172**, 64-79 (2016).
800 56. LeBlanc, R.*, et al.* Proteasome inhibitor PS-341 inhibits human myeloma cell
801 growth in vivo and prolongs survival in a murine model. *Cancer Res* **62**, 4996-5000
802 (2002).
803 57. Manasanch, E.E. & Orlowski, R.Z. Proteasome inhibitors in cancer therapy. *Nat*
804 *Rev Clin Oncol* **14**, 417-433 (2017).

805 58. Morgan, G.J., *et al.* First-line treatment with zoledronic acid as compared with
806 clodronic acid in multiple myeloma (MRC Myeloma IX): a randomised controlled
807 trial. *Lancet* **376**, 1989-1999 (2010).
808 59. Accardi, F., Toscani, D., Bolzoni, M., Dalla Palma, B., Aversa, F. & Giuliani, N.
809 Mechanism of Action of Bortezomib and the New Proteasome Inhibitors on
810 Myeloma Cells and the Bone Microenvironment: Impact on Myeloma-Induced
811 Alterations of Bone Remodeling. *Biomed Res Int* **2015**, 172458 (2015).
812 60. Seshadri, R., Kutlaca, R.J., Trainor, K., Matthews, C. & Morley, A.A. Mutation rate
813 of normal and malignant human lymphocytes. *Cancer Res* **47**, 407-409 (1987).
814 61. Duesberg, P., Stindl, R. & Hehlmann, R. Explaining the high mutation rates of
815 cancer cells to drug and multidrug resistance by chromosome reassortments that
816 are catalyzed by aneuploidy. *Proc Natl Acad Sci U S A* **97**, 14295-14300 (2000).
817 62. Gatenby, R.A., Silva, A.S., Gillies, R.J. & Frieden, B.R. Adaptive therapy. *Cancer*
818 *Res* **69**, 4894-4903 (2009).
819 63. Keats, J.J., *et al.* Clonal competition with alternating dominance in multiple
820 myeloma. *Blood* **120**, 1067-1076 (2012).
821 64. Walker, B.A., *et al.* Intraclonal heterogeneity is a critical early event in the
822 development of myeloma and precedes the development of clinical symptoms.
823 *Leukemia* **28**, 384-390 (2014).
824 65. Paiva, B., *et al.* Phenotypic and genomic analysis of multiple myeloma minimal
825 residual disease tumor cells: a new model to understand chemoresistance. *Blood*
826 **127**, 1896-1906 (2016).
827 66. Ayati, B.P., Edwards, C.M., Webb, G.F. & Wikswo, J.P. A mathematical model of
828 bone remodeling dynamics for normal bone cell populations and myeloma bone
829 disease. *Biol Direct* **5**, 28 (2010).
830 67. Ji, B., Genever, P.G. & Fagan, M.J. A virtual approach to evaluate therapies for
831 management of multiple myeloma induced bone disease. *Int J Numer Method*
832 *Biomed Eng* **32**, e02735 (2016).
833 68. Ji, B., Genever, P.G., Patton, R.J. & Fagan, M.J. Mathematical modelling of the
834 pathogenesis of multiple myeloma-induced bone disease. *Int J Numer Method*
835 *Biomed Eng* **30**, 1085-1102 (2014).

836 69. Sartakhti, J.S., Manshaei, M.H., Bateni, S. & Archetti, M. Evolutionary Dynamics
837 of Tumor-Stroma Interactions in Multiple Myeloma. *PLoS One* **11**, e0168856
838 (2016).
839 70. Wang, Y., Pivonka, P., Buenzli, P.R., Smith, D.W. & Dunstan, C.R. Computational
840 modeling of interactions between multiple myeloma and the bone
841 microenvironment. *PLoS One* **6**, e27494 (2011).
842 71. Qiao, M., Wu, D., Carey, M., Zhou, X. & Zhang, L. Multi-Scale Agent-Based
843 Multiple Myeloma Cancer Modeling and the Related Study of the Balance between
844 Osteoclasts and Osteoblasts. *PLoS One* **10**, e0143206 (2015).
845 72. Dingli, D., Chalub, F.A., Santos, F.C., Van Segbroeck, S. & Pacheco, J.M. Cancer
846 phenotype as the outcome of an evolutionary game between normal and malignant
847 cells. *Br J Cancer* **101**, 1130-1136 (2009).
848 73. Picco, N., Sahai, E., Maini, P.K. & Anderson, A.R.A. Integrating Models to Quantify
849 Environment-Mediated Drug Resistance. *Cancer Res* **77**, 5409-5418 (2017).
850 74. Su, J.*, et al.* Targeting the biophysical properties of the myeloma initiating cell
851 niches: a pharmaceutical synergism analysis using multi-scale agent-based
852 modeling. *PLoS One* **9**, e85059 (2014).
853 75. Perez-Velazquez, J., Gevertz, J.L., Karolak, A. & Rejniak, K.A.
854 Microenvironmental Niches and Sanctuaries: A Route to Acquired Resistance. *Adv*
855 *Exp Med Biol* **936**, 149-164 (2016).
856 76. Perez-Velazquez, J. & Rejniak, K.A. Drug-Induced Resistance in
857 Micrometastases: Analysis of Spatio-Temporal Cell Lineages. *Front Physiol* **11**,
858 319 (2020).
859 77. Ghobrial, I.M.*, et al.* A Phase Ib/II Trial of the First-in-Class Anti-CXCR4 Antibody
860 Ulocuplumab in Combination with Lenalidomide or Bortezomib Plus
861 Dexamethasone in Relapsed Multiple Myeloma. *Clin Cancer Res* **26**, 344-353
862 (2020).
863 78. Ghobrial, I.M.*, et al.* Phase I/II trial of the CXCR4 inhibitor plerixafor in combination
864 with bortezomib as a chemosensitization strategy in relapsed/refractory multiple
865 myeloma. *Am J Hematol* **94**, 1244-1253 (2019).

866 79. Suzuki, K., Nishiwaki, K. & Yano, S. Treatment Strategies Considering Micro-
867 Environment and Clonal Evolution in Multiple Myeloma. *Cancers (Basel)* **13**(2021).
868 80. Zhang, J., Cunningham, J., Brown, J. & Gatenby, R. Evolution-based mathematical
869 models significantly prolong response to abiraterone in metastatic castrate-
870 resistant prostate cancer and identify strategies to further improve outcomes. *Elife*
871 **11**(2022).
872 81. Frankenstein, Z.*, et al.* Stromal reactivity differentially drives tumour cell evolution
873 and prostate cancer progression. *Nat Ecol Evol* **4**, 870-884 (2020).
874 82. Jenner, A.L.*, et al.* Agent-based computational modeling of glioblastoma predicts
875 that stromal density is central to oncolytic virus efficacy. *iScience* **25**, 104395
876 (2022).
877 83. Manolagas, S.C. Birth and death of bone cells: basic regulatory mechanisms and
878 implications for the pathogenesis and treatment of osteoporosis. *Endocr Rev* **21**,
879 115-137 (2000).
880 84. Lemaire, V., Tobin, F.L., Greller, L.D., Cho, C.R. & Suva, L.J. Modeling the
881 interactions between osteoblast and osteoclast activities in bone remodeling. *J*
882 *Theor Biol* **229**, 293-309 (2004).
883 85. Schenck, R.O., Brosula, G., West, J., Leedham, S., Shibata, D. & Anderson,
884 A.R.A. Gattaca: Base-Pair Resolution Mutation Tracking for Somatic Evolution
885 Studies using Agent-based Models. *Mol Biol Evol* **39**(2022).
886 86. West, J., Schenck, R.O., Gatenbee, C., Robertson-Tessi, M. & Anderson, A.R.A.
887 Normal tissue architecture determines the evolutionary course of cancer. *Nat*
888 *Commun* **12**, 2060 (2021).
889 87. Moser-Katz, T., Joseph, N.S., Dhodapkar, M.V., Lee, K.P. & Boise, L.H. Game of
890 Bones: How Myeloma Manipulates Its Microenvironment. *Front Oncol* **10**, 625199
891 (2020).
892 88. Guder, C., Gravius, S., Burger, C., Wirtz, D.C. & Schildberg, F.A.
893 Osteoimmunology: A Current Update of the Interplay Between Bone and the
894 Immune System. *Front Immunol* **11**, 58 (2020).
895 89. Mori, G., D'Amelio, P., Faccio, R. & Brunetti, G. The Interplay between the bone
896 and the immune system. *Clin Dev Immunol* **2013**, 720504 (2013).

897 90. Kawano, Y., *et al.* Targeting the bone marrow microenvironment in multiple
898 myeloma. *Immunol Rev* **263**, 160-172 (2015).
899 91. Zavidij, O., *et al.* Single-cell RNA sequencing reveals compromised immune
900 microenvironment in precursor stages of multiple myeloma. *Nat Cancer* **1**, 493-
901 506 (2020).
902 92. Gallaher, J.A., Enriquez-Navas, P.M., Luddy, K.A., Gatenby, R.A. & Anderson,
903 A.R.A. Spatial Heterogeneity and Evolutionary Dynamics Modulate Time to
904 Recurrence in Continuous and Adaptive Cancer Therapies. *Cancer Res* **78**, 2127-
905 2139 (2018).
906 93. Gallaher, J., *et al.* Methods for determining key components in a mathematical
907 model for tumor-immune dynamics in multiple myeloma. *J Theor Biol* **458**, 31-46
908 (2018).
909 94. Vander Velde, R., *et al.* Resistance to targeted therapies as a multifactorial,
910 gradual adaptation to inhibitor specific selective pressures. *Nat Commun* **11**, 2393
911 (2020).
912 95. Anderson, A.R., Weaver, A.M., Cummings, P.T. & Quaranta, V. Tumor morphology
913 and phenotypic evolution driven by selective pressure from the microenvironment.
914 *Cell* **127**, 905-915 (2006).
915 96. Anderson, A.R. A hybrid mathematical model of solid tumour invasion: the
916 importance of cell adhesion. *Math Med Biol* **22**, 163-186 (2005).
917 97. Bravo, R.R., *et al.* Hybrid Automata Library: A flexible platform for hybrid modeling
918 with real-time visualization. *PLoS Comput Biol* **16**, e1007635 (2020).
919 98. Jilka, R.L., Weinstein, R.S., Bellido, T., Parfitt, A.M. & Manolagas, S.C. Osteoblast
920 programmed cell death (apoptosis): modulation by growth factors and cytokines. *J*
921 *Bone Miner Res* **13**, 793-802 (1998).
922 99. Durdan, M.M., Azaria, R.D. & Weivoda, M.M. Novel insights into the coupling of
923 osteoclasts and resorption to bone formation. *Semin Cell Dev Biol* **123**, 4-13
924 (2022).
925 100. Plotkin, L.I. & Bellido, T. Beyond gap junctions: Connexin43 and bone cell
926 signaling. *Bone* **52**, 157-166 (2013).

927 101. Stains, J.P. & Civitelli, R. Cell-cell interactions in regulating osteogenesis and
928 osteoblast function. *Birth Defects Res C Embryo Today* **75**, 72-80 (2005).
929 102. Stains, J.P., Watkins, M.P., Grimston, S.K., Hebert, C. & Civitelli, R. Molecular
930 mechanisms of osteoblast/osteocyte regulation by connexin43. *Calcif Tissue Int*
931 **94**, 55-67 (2014).
932 103. Civitelli, R. Cell-cell communication in the osteoblast/osteocyte lineage. *Arch*
933 *Biochem Biophys* **473**, 188-192 (2008).
934 104. Watkins, M.*, et al.* Osteoblast connexin43 modulates skeletal architecture by
935 regulating both arms of bone remodeling. *Mol Biol Cell* **22**, 1240-1251 (2011).
936 105. Schindelin, J.*, et al.* Fiji: an open-source platform for biological-image analysis. *Nat*
937 *Methods* **9**, 676-682 (2012).
938
939
940

941 **Figures**

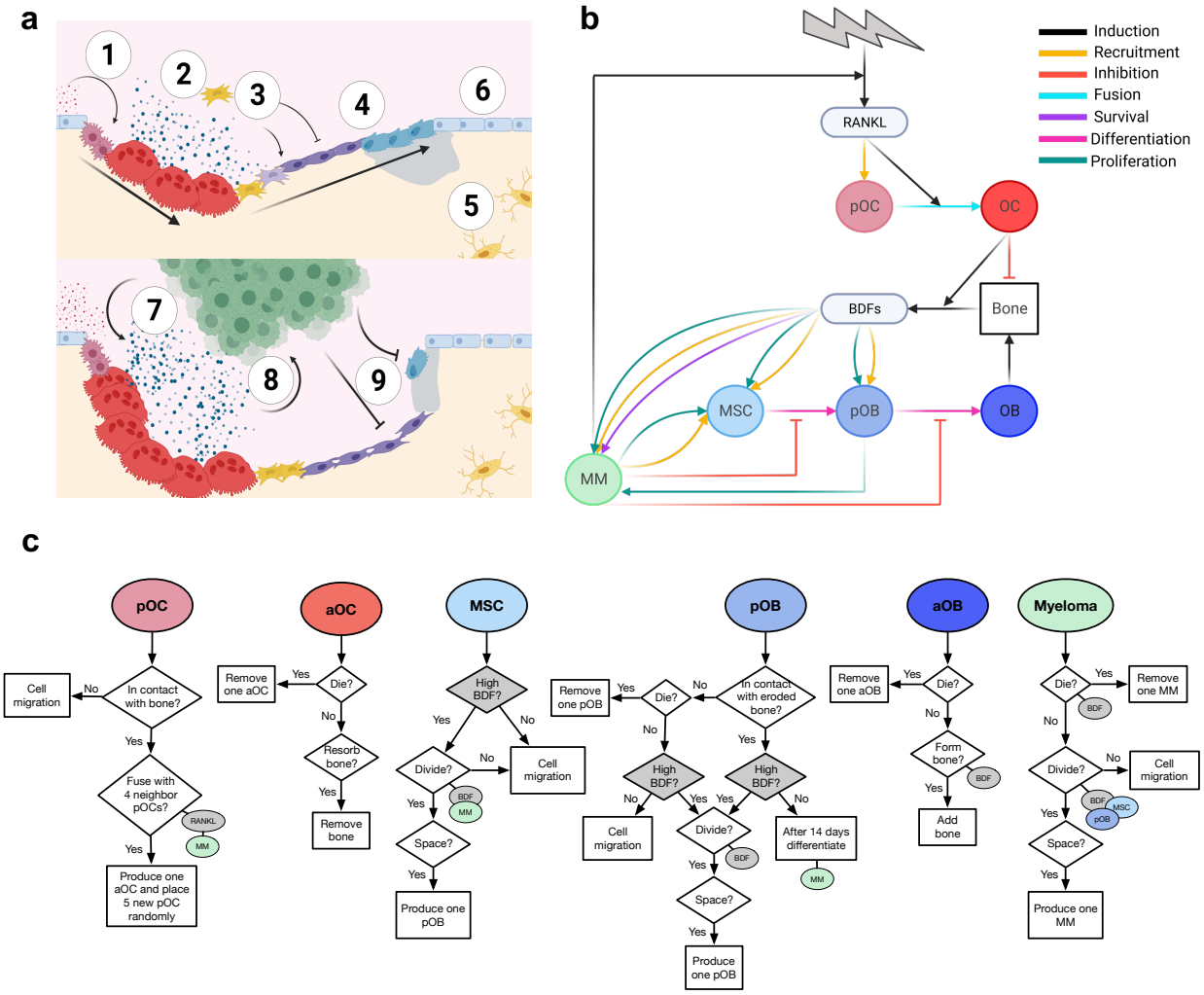

942

943 **Fig. 1. Development of a hybrid HCA of the naïve and myeloma bone**
944 **microenvironment.**

945 **a**, Bone-lining osteoblast lineage cells release RANKL inducing fusion and maturation of
946 osteoclasts (1). Osteoclasts resorb the bone, releasing stored bone-derived factors
947 (BDFs) such as TGF-β (2). TGF-β recruits local MSCs and stimulates asymmetric division
948 in to preosteoblasts (2). When TGF-β levels remain high, preosteoblasts rapidly
949 proliferate. Following osteoclast apoptosis, release of TGF-β falls and preosteoblasts
950 differentiate to mature bone producing osteoblasts (3). While TGF-β levels remain low,
951 osteoblasts produce new bone (4). As bone returns to normal, a fraction of the osteoblasts
952 is buried within the matrix becoming terminally differentiated osteoblasts (5), the

953 remaining osteoblasts undergo apoptosis, or become quiescent bone-lining cells (6).
954 Myeloma cells enhance the formation of osteoclasts (7), enhanced bone resorption
955 produces higher levels of BDFs which fuel myeloma growth (8) and inhibit osteoblast
956 differentiation (8) and activity (9). Created with biorender.com
957 **b**, Interaction diagram between cell types in the HCA and factors such as BDFs and
958 RANKL (created with biorender.com). A more detailed interaction diagram with
959 references can be found in supplementary figure 1.
960 **c**, Flowcharts describing the sequence of steps followed by preosteoclasts, osteoclasts,
961 MSCs, preosteoblasts, osteoblasts, and myeloma cells.
962

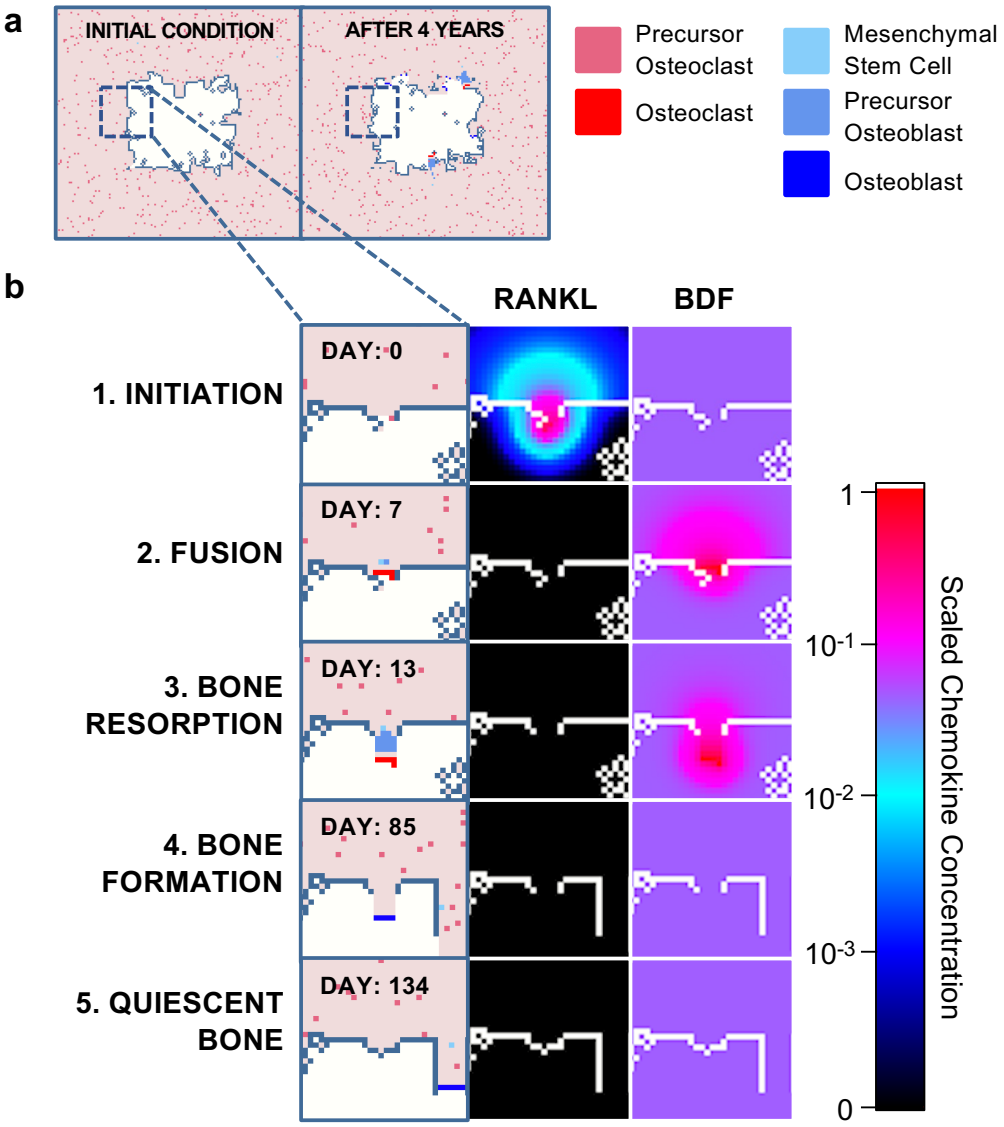

Fig. 2. The HCA model captures all stages of bone homeostasis.

a, Images from simulations at initial conditions (left) and after 4 years (right). Legend depicts colors of cell types in the model.

b, BMU is initiated in response to release of RANKL from bone lining cells (1). preosteoclasts migrate to RANKL and fuse to form an osteoclast under highest concentrations (2). osteoclast resorbs bone and stored BDFs are released which recruits MSCs. MSCs divide asymmetrically producing preosteoblasts which proliferate rapidly

under high TGF-β conditions. Upon completion of resorption, BDF levels fall allowing for preosteoblast differentiation to osteoblasts. osteoblasts form new bone (4) and ultimately undergo apoptosis or become quiescent bone lining cells (5).

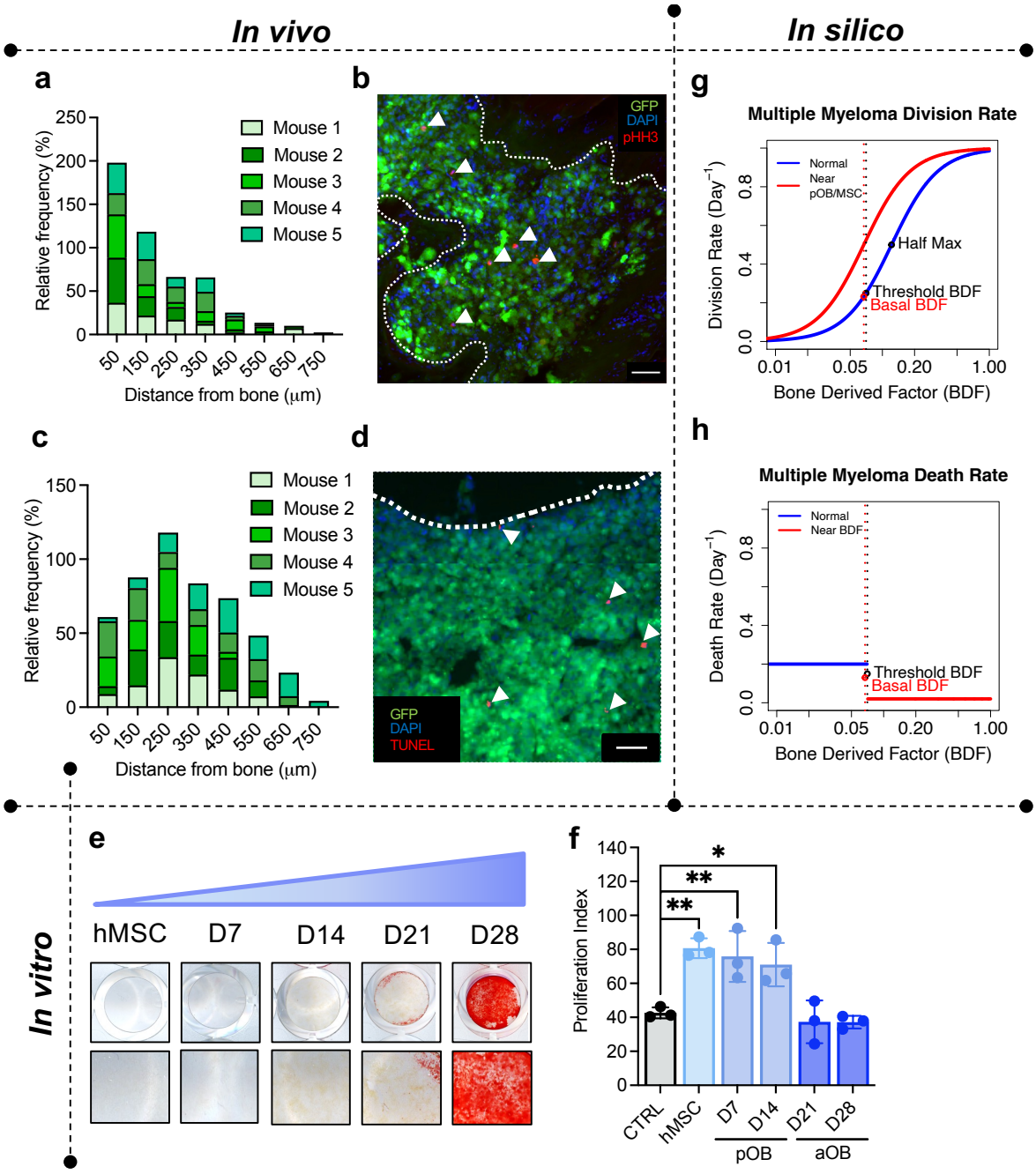

Fig. 3. Multiple myeloma cells receive proliferative and survival advantages from the bone marrow microenvironment.

a, Quantification of the distance of phosphorylated histone H3 positive (pHH3+; red) myeloma cells (green) to the nearest trabecular or cortical bone in U266^{GFP}-bearing mice 100 days post inoculation. N=5 tibia.

982 **b,** Representative images from experiment in **a**, DAPI (blue) was used as a nuclear
983 counterstain. White dotted line indicates tumor bone interface. Scale bar, 50 microns.
984 **c,** Quantification of the distance of TUNEL+ (red) myeloma cells (green) to the nearest
985 trabecular or cortical bone in $U266^{GFP}$-bearing mice 100 days post inoculation. N=5 tibia
986 **d,** Representative image from experiment described in **c**, DAPI (blue) was used as a
987 nuclear counterstain. White dotted line indicates tumor bone interface. Scale bar, 50
988 microns.
989 **e,** Images of huMSCs differentiated to different stages of the osteoblast lineage. Cells
990 were stained with Alizarin Red to identify mineralization.
991 **f,** Proliferation index of CM-DiL stained U266 cells 7 days after growth in 50% conditioned
992 medium from control wells or cells of the osteoblast lineage. Results are displayed as
993 means of at least 3 experiments.
994 **g,** Plot of functional form used to represent the division rate of myeloma cells in the
995 presence and absence of preosteoblasts/MSCs.
996 **h,** Plot of functional form used to represent the death of myeloma cells when BDF is above
997 and below a threshold.
998 * p-value < 0.05, ** p-value <0.01

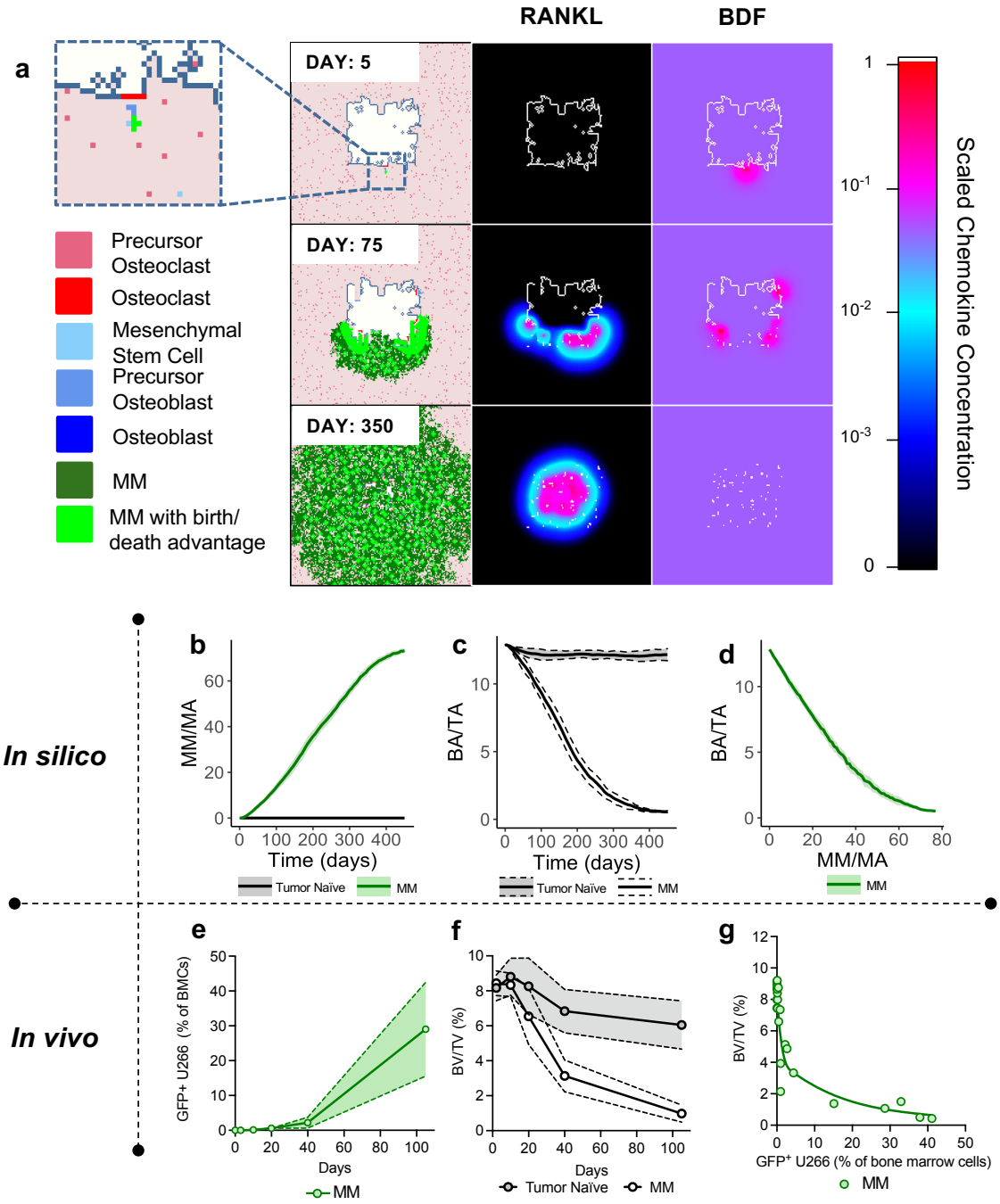

Fig. 4. Computational and biological model outputs of myeloma growth and bone dynamics.

a, HCA model images showing single myeloma cell (Day 5), colonization of the marrow by MM cells (Day 75), increased osteoclastogenesis (Day 75, RANKL), bone resorption

1004 (Day 75; BDF) and eventual takeover of the marrow by MM cells (Day 350). Light green
1005 myeloma cells indicate MM cells with proliferative or survival advantage.
1006 **b**, Myeloma growth dynamics in HCA model in the absence of treatment.
1007 **c**, Myeloma induced loss of trabecular bone in HCA model compared to normal bone
1008 homeostasis.
1009 **d**, Bone loss decreases rapidly with myeloma expansion *in silico*.
1010 **e**, Myeloma growth in bone marrow of mice inoculated with U266-GFP cells over time
1011 N=3-5 tibia per time point.
1012 **f**, Trabecular bone volume fraction (BV/TV) was assessed *ex vivo* with high-resolution
1013 microCT. N=3-5 tibia per time point.
1014 **g**, Biological model shows rapid myeloma-induced bone loss.
1015

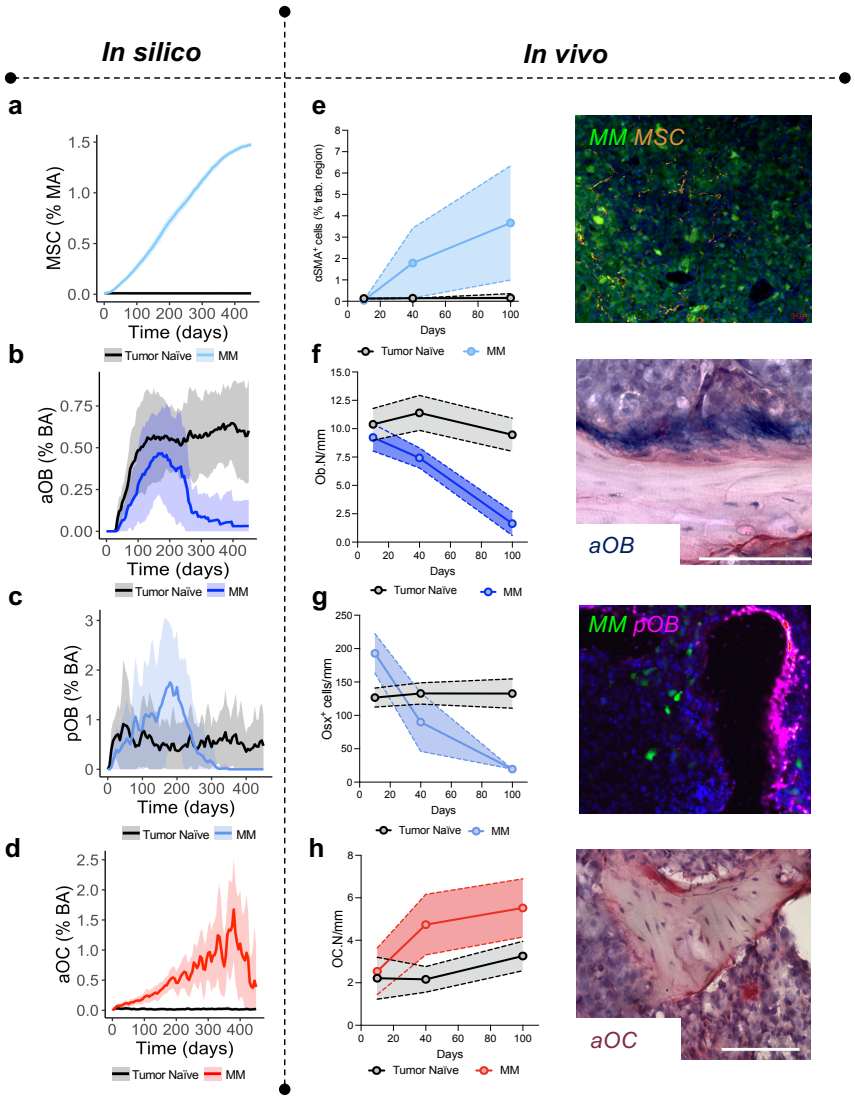

1016

1017 **Fig. 5. Computational and biological model outputs of cell types in the myeloma**
1018 **bone microenvironment.** **a-d,** Computational model outputs of increasing MSC
1019 percentage of the marrow area (%MA) (**a**), loss of osteoblasts (**b**) rise and fall of
1020 preosteoblast percentage (**c**) and increasing osteoclast percentage due to growth of MM
1021 (**d**). **e-h**, *Ex vivo* analysis of histological sections from the U266-GFP myeloma model
1022 (N=3-5 tibia per time point.) per time point demonstrates increasing presence of αSMA+
1023 MSCs (**e**), loss of ALP+ cuboidal osteoblasts (**f**), early increase and subsequent reduction
1024 of OSX+ preosteoblasts (**g**) and increasing numbers of TRAcP+ multinucleated
1025 osteoclasts (**h**) compared to tumor naïve mice.

1026

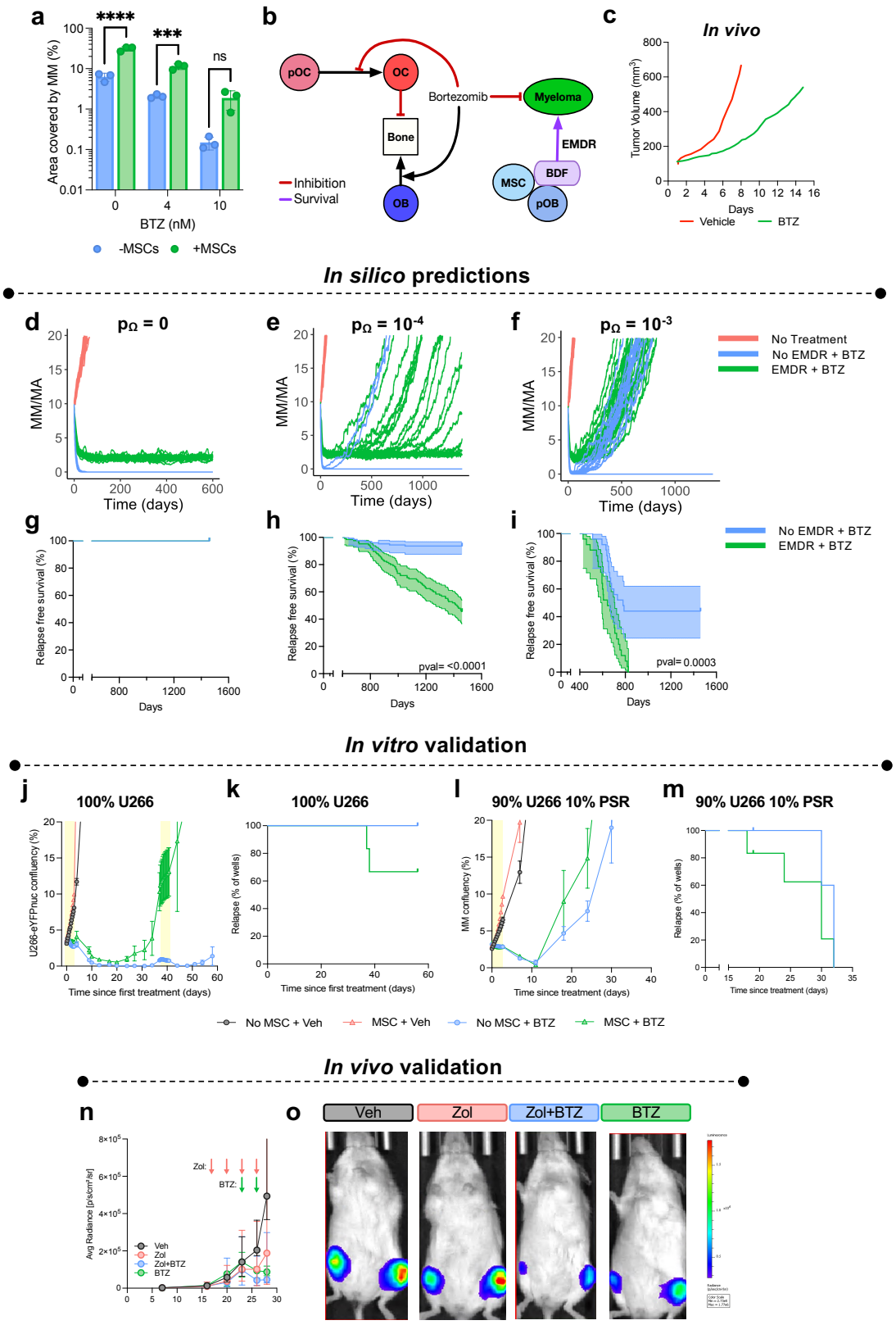

Fig. 6. EMDR contributes to minimal residual disease and relapse.

1029 **a,** GFP+ U266 MM were plated alone or with huMSCs in the presence or absence of BTZ;
1030 MM burden was measured after 72h by area covered by GFP+ cells.
1031 **b**, Interaction diagram showing the cell types and factors in the HCA that are affected by
1032 BTZ or contribute to EMDR.
1033 **c**, *In vivo* growth of MM cells with and without BTZ treatment, data was taken from [42].
1034 **d-f,** Model outputs of MM growth with continuous BTZ treatment, +/- EMDR when MM
1035 cells do not develop resistance (**d**) or with a probability to develop resistance (10^{-4}, **e** or
1036 10^{-3}, **f**) and develop resistance.
1037 **g-i**, Kaplan-Meier plot of relapse-free survival from simulations described in **d-f**.
1038 **j,** Nuclear-eYFP+ U266 were cultured alone or with huMSCs in the presence or absence
1039 of 10nM of BTZ. MM growth was tracked by eYFP over 60 days. Yellow shading indicates
1040 periods when treatment was on.
1041 **k**, Kaplan-Meier plot of 'relapse' (wells reaching >20% MM confluency) from experiment
1042 described in j.
1043 **l**, MM cells (90% U266- Nuclear-eYFP+ and 10% PSR-RFP+) were cultured alone or with
1044 huMSCs in the presence or absence of 10nM of BTZ.
1045 **m**, Kaplan-Meier plot of 'relapse' (wells reaching >20% MM confluency) from experiment
1046 described in l.
1047 **n**, Average U266 growth by BLI after MM cells (90% U266-$GFP^{+}Luc^{+}$, 10% PSR-RFP)
1048 were tail vein injected into NSG mice. Mice were divided into two groups and pre-treated
1049 with vehicle or Zol (30ug/kg) for 1 week prior to mice being randomized and treated with
1050 either vehicle (n=5 mice), Zol (n=5 mice), Zol+BTZ (n=7 mice), or BTZ (0.5mg/kg; n= 4
1051 mice). Pink and green arrows indicate days of Zol or BTZ treatment respectively.
1052 **o**, Representative BLI IVIS images from the experiment described in **n**.
1053

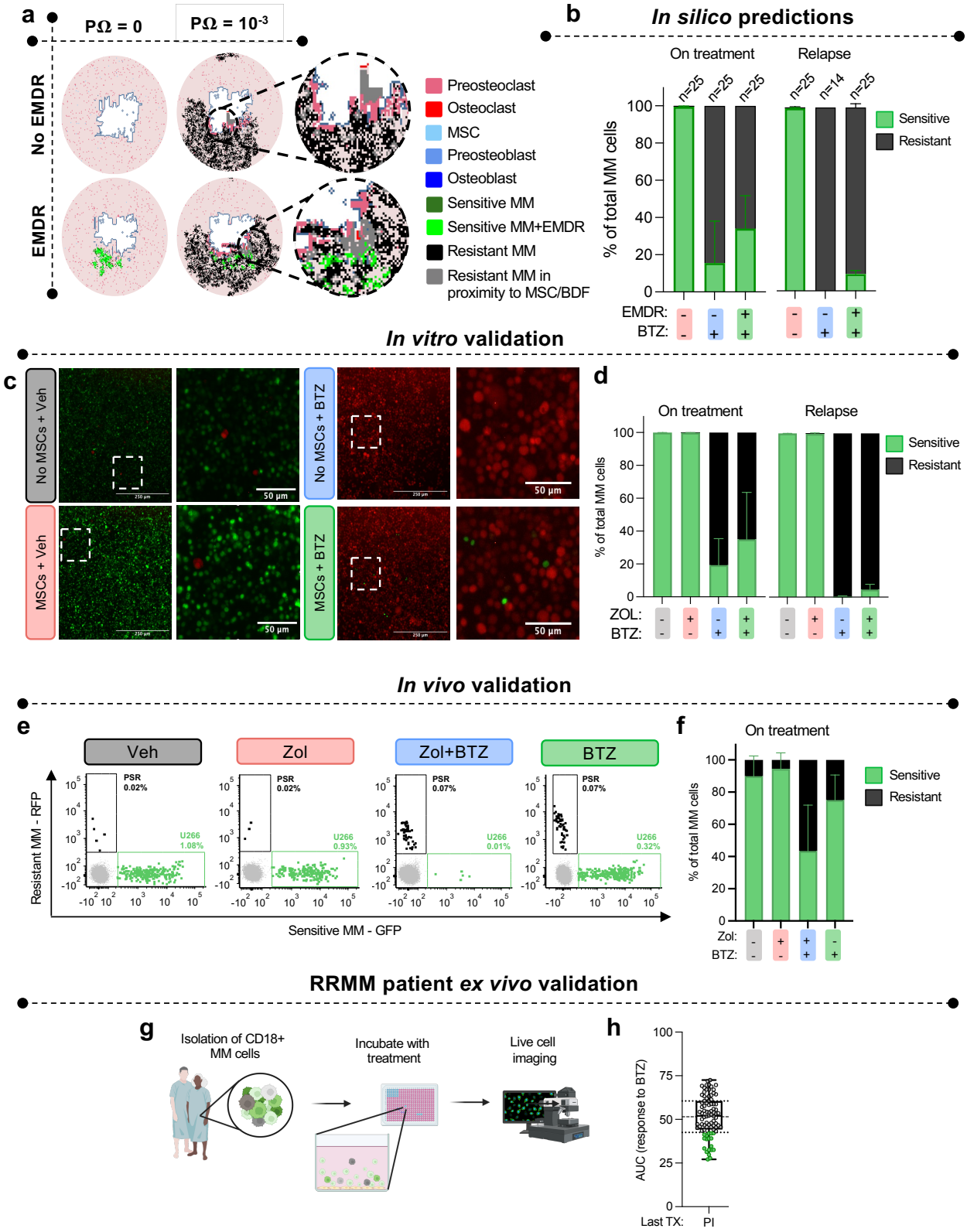
a
PΩ = 0
PΩ = 10-3
No EMDR
EMDR
Preosteoclast
Osteoclast
MSC
Preosteoblast
Osteoblast
Sensitive MM
Sensitive MM+EMDR
Resistant MM
Resistant MM in proximity to MSC/BDF
b
In silico predictions
On treatment
Relapse
% of total MM cells
Sensitive
Resistant
EMDR:
BTZ:
In vitro validation
c
No MSCs + Veh
MSCs + Veh
No MSCs + BTZ
MSCs + BTZ
50 µm
d
ZOL:
BTZ:
In vivo validation
e
Veh
Zol
Zol+BTZ
BTZ
PSR 0.02%
PSR 0.02%
PSR 0.07%
PSR 0.07%
U266 1.08%
U266 0.93%
U266 0.01%
U266 0.32%
Resistant MM - RFP
Sensitive MM - GFP
f
Zol:
BTZ:
RRMM patient ex vivo validation
g
Isolation of CD18+ MM cells
Incubate with treatment
Live cell imaging
h
AUC (response to BTZ)
Last TX:
PI

1054

1055 **Fig. 7. EMDR contributes protection of sensitive MM and tumor heterogeneity.**
1056 **a,** HCA images from simulations with continuous BTZ application, with no resistance
1057 probability (p_Ω=0) or high resistance probability ($p_\Omega=10^{-3}$) in the presence or absence of
1058 EMDR.
1059 **b**, Computational outputs of the proportion of BTZ-sensitive and BTZ-resistant MM cells
1060 1 year on treatment (left) and at relapse (right) with $p_\Omega=10^{-3}$. Related to Figures 6f and 6i.
1061 **c**, Representative images of U266-nuclear eYFP+ and PSR-RFP+ cells at relapse when
1062 cultured alone or huMSCs, with or without BTZ in vitro. Related to figure **6j-k**.
1063 **d**, The proportion of BTZ-sensitive (U266-nuclear eYFP+) and BTZ-resistant (PSR-RFP+
1064 MM cells cultured alone or with huMSCs with and without BTZ on treatment (left) and at
1065 relapse (right). Related to Figures **6l-m** and **7d**.
1066 **e**, Representative flow plots of BTZ-sensitive (U266 GFP+Luc+; green) and BTZ-resistant
1067 (PSR-RFP+; black) from the bone marrow (gray) of NSG mice treated with vehicle, Zol,
1068 Zol+BTZ or BTZ. Vehicle = 10 femur, Zol = 10 femur, Zol+BTZ = 12 femur, BTZ = 8 femur.
1069 **F**, Proportion of BTZ-sensitive (U266 GFP+Luc+) and BTZ-resistant (PSR-RFP+) MM
1070 cells in the bone marrow of NSG mice treated with vehicle, Zol, Zol+BTZ or BTZ.
1071 **g,** schematic of the EMMA platform. CD138+ MM cells and stroma are isolated from MM
1072 patients and co-cultured without test compounds. Live cell imaging is used to assess
1073 viability.
1074 **h**, The AUC of MM cells from RRMM patients, whose last relapse was to a PI-containing
1075 regimen (PI) or a non-PI containing regimen (Other), in response to BTZ. Green dots
1076 identify sensitive MM cells (quartile 1).
1077

1078

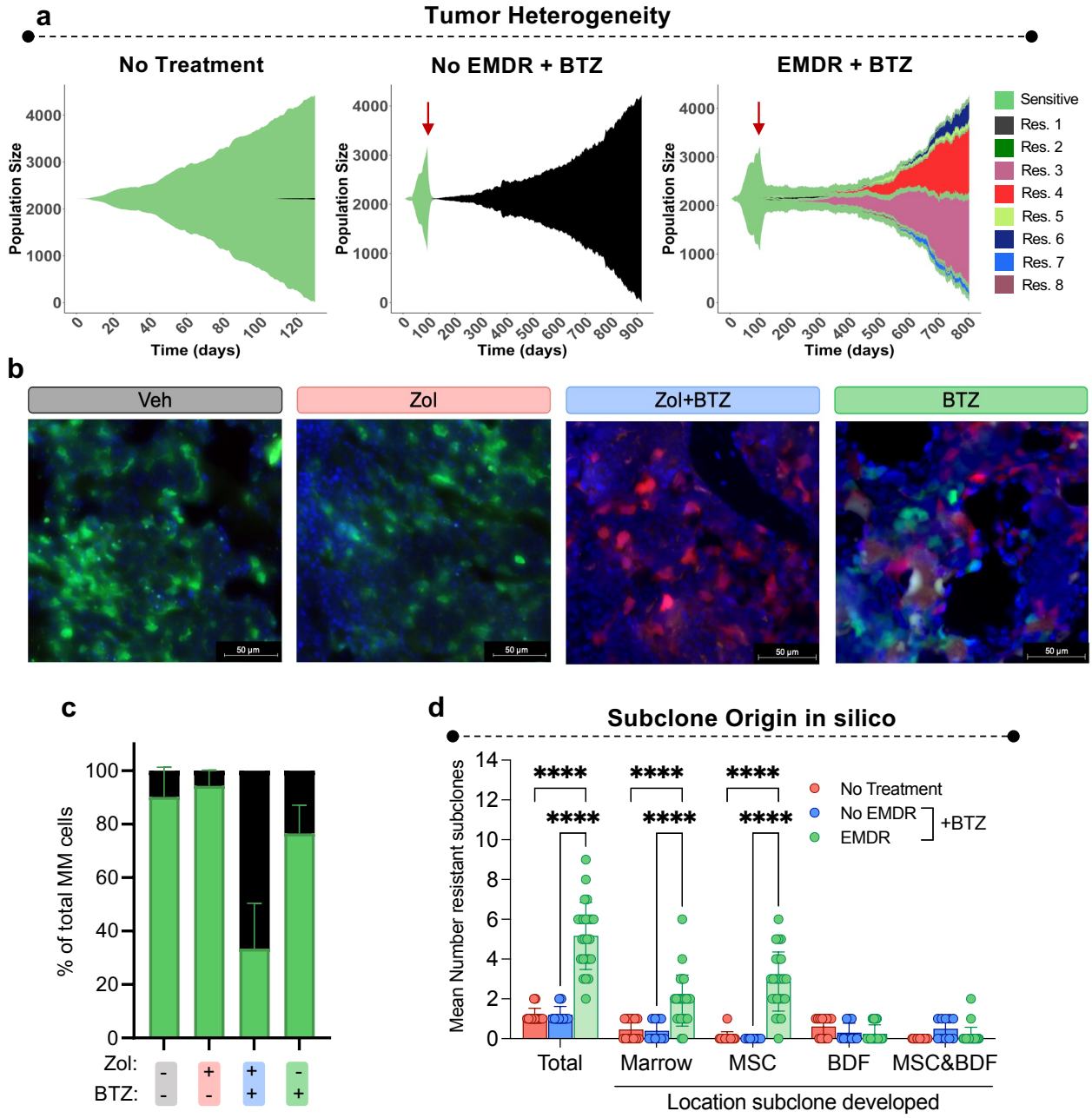

Fig. 8. EMDR contributes to tumor heterogeneity upon relapse.

a, Muller plots of sensitive and individual BTZ resistant (Res) sub-clones from simulations described in **a-c**. Colors denote different subclones. Red arrow indicates start of BTZ treatment. **** pvalue <0.0001

1085 **b**, Images of GFP+ U266 (green) and RFP+ PSR (red) MM cells and cell nuclei (DAPI;
1086 blue) in tibial sections of mice from *in vivo* study described in Figure 7. Magnification 20X.
1087 Scale bar 50 microns.
1088 **c**, Relative quantification of GFP+ U266 and PSR MM in tibial sections described in Figure
1089 8b. Vehicle = 5 tibia, Zol = 5 tibia, Zol+BTZ = 7 tibia, BTZ = 4 tibia.
1090 **d**, Mean number of resistant sub-clones arising following BTZ treatment tumors that
1091 reached 20% with resistant subclones and the locations within the bone marrow
1092 microenvironment where each subclone originated, with/without EMDR from simulations
1093 described in **a**. n = 13/25 (No Treatment), n = 10/25 (No EMDR+BTZ), n = 24/25
1094 (EMDR+BTZ).
1095
1096
1097

Supplementary: The bone ecosystem facilitates multiple myeloma relapse and the evolution of heterogeneous proteasome inhibitor resistant disease.

Authors/affiliations

Ryan T. Bishop[1]*, Anna K. Miller[2]*, Matthew Froid[2,3], Niveditha Nerlakanti[1,3]Tao Li[1], Jeremy Frieling[1], Mostafa Nasr[1,3], Karl Nyman[1,3] Praneeth R Sudalagunta[4], Rafael Canevarolo[4], Ariosto Siqueira Silva[4], Kenneth H. Shain[1,5], Conor C. Lynch[1]+ and David Basanta[2]+

[1] Tumor Biology Department, H. Lee Moffitt Cancer Center and Research Institute, Tampa, Florida

[2] Department of Integrated Mathematical Oncology, H. Lee Moffitt Cancer Center and Research Institute, Tampa, Florida

[3] The Cancer Biology Ph.D. Program, University of South Florida, Tampa, Florida, USA.

[4] Department of Metabolism and Physiology, H. Lee Moffitt Cancer Center and Research Institute, Tampa, FL 33612, USA

[5] Department of Malignant Hematology, H. Lee Moffitt Cancer Center and Research Institute, Tampa, Florida

* These authors contributed equally as first authors

+ These authors contributed equally as senior authors.

1121 **Supplementary Methods**

1122

1123

1124 **1. Hybrid Cellular Automaton Methods**

1125 We developed a new hybrid cellular automaton (HCA) model to capture some of the key
1126 cellular and molecular populations that characterize the MM bone ecosystem. This model
1127 was developed from scratch although some of the assumptions, including those about
1128 what are the most important populations for the model, build on our previous experience
1129 building a similar model to study bone metastatic prostate cancer[1-3]. In this instance our
1130 code (available on this repository: https://github.com/dbasanta/MM_ABM) build on the
1131 HAL library which will help our code become a more self-sufficient and reusable platform
1132 of use to other bone-modelling scientists. We have generated different and novel data
1133 and *in vivo* model to parameterize, calibrate the model and validate the results. Building
1134 on our experience starting computational models of cancer from homeostasis, this new
1135 code is more robust and capable of performing bone remodeling simultaneously in
1136 several sites. This robustness is also demonstrated by the fact that homeostasis in the
1137 bone is preserved even with the use of variable depths of osteoclast-mediated bone
1138 resorption which was not the case previously.

1139

1140 The model we developed incorporates six different cell types, including precursor
1141 osteoclasts, active osteoclasts, mesenchymal stem cells (MSCs), precursor osteoblasts
1142 adult osteoblasts, and multiple myeloma (MM) cells. Additionally, we incorporate two
1143 signaling molecules including RANKL and bone derived factors (BDFs) such as
1144 transforming growth factor beta (TGF-β). In the sections below, we describe the specific
1145 assumptions and parameters incorporated into the HCA of normal bone remodeling
1146 (**Supplementary Section 1.1**), multiple myeloma (**Supplementary Section 1.2**), and
1147 bortezomib treatment (**Supplementary Section 1.3**). Refer to **Supplementary Tables 1-**
1148 **6** in **Supplementary Section 1.5** for a complete description of the parameters and values
1149 used in the HCA.

1150

1151 **1.1. Normal Bone Remodeling**

1152

1153 **Algorithmic Implementation**

1154 *Initial and boundary conditions of agent grid*

1155 We first develop a model of trabecular bone remodeling in which we represent a cross
1156 section of the bone marrow as a 2D rectangular grid. We define the length of the grid as
1157 $0 \leq x \leq 160\,px$ and the height as $0 \leq y \leq 150\,px$, where $\Delta x = 1\,px = 10\,\mu m$, the
1158 diameter of a myeloma cell. To obtain the initial arrangement of bone, we first initiated the
1159 bone as a $60\,px \times 50\,px$ rectangle in the center of the grid, surrounded by bone marrow.
1160 The initial area of the bone was set to represent the approximate bone area to total area
1161 (BA/TA) from sham limbs of wild type RAG2 mice (mean: 12.4%, n = 6, data not shown).
1162 As bone remodeling occurs over time, the initial rectangle is transformed, though the
1163 BA/TA remains approximately constant. We arbitrarily select one of these final bone
1164 configurations as the initial condition for subsequent runs of the model. Hence, trabecular
1165 bone initially consists of 12.9% of the total area. We assume that the number of precursor
1166 osteoclasts remains constant and is approximately equal to the number of monocytes,
1167 which is 2.8% of the bone marrow[4]. MSCs initially consist of 0.01% of the bone marrow[5].
1168 We implement periodic boundary conditions on all sides of the domain for all cell types.

1169

1170 *Timesteps*

1171 We use two separate time step sizes, Δt_{diff} and Δt_{cells}, to account for the differences in
1172 the timescales for diffusion (fast) versus cell processes (slow). We use $\Delta t_{diff} = 1\,sec$ and
1173 $\Delta t_{cells} = 6\,min$.

1174

1175 *Simulation Process*

1176 The computational algorithm was implemented using the Hybrid Automata Library
1177 (HAL)[6] and is organized as shown in **Supplementary Fig. 1a** and **Fig. 1c**.

1178

1179 **Precursor osteoclasts**

1180

1181 *Fusion*

Precursor osteoclasts fuse and become multinucleated osteoclasts. This process is regulated by the expression of RANKL (**Supplementary Fig. 2f**), which is expressed by osteoblast lineage cells such as osteoblast precursors, osteocytes, and bone lining cells[7,8]. It is not well understood which cell type is the primary source of RANKL for osteoclast fusion, but it has been suggested that microdamage to trabecular bone leads to osteocyte apoptosis, which may signal to bone lining cells to express RANKL[7,8]. In our model, we assume that bone remodeling events are initiated through microfractures that are uniformly distributed over 4 years, the approximate turnover time of trabecular bone[9]. The total number of remodeling events was approximated using the initial total amount of bone divided by the approximate amount of bone resorbed per osteoclast. For simplicity, each basic multicellular unit (BMU) initiates from a single remodeling event that consists of five adjacent cells on the perimeter of bone that begin to express RANKL. The number of cells expressing RANKL was selected to equal the approximate diameter of an osteoclast, which is $50\ \mu m$[10].Precursor osteoclasts follow the gradient of RANKL and once there are five adjacent cells on the perimeter of bone, they fuse to become an active osteoclast (osteoclast) with probability

$$p_{fusion} = 1 - (1 - MAX_FUSION_RATE)^{TIMESTEP_AGENT} \#(1)$$

This probability reflects that fusion is a process that takes at least 3 days to complete. We note that this probability is scaled geometrically since the agent time step (6 min) is smaller than the unit of time (1 hour), hence the probability that the preosteoclast does not fuse per agent time step must be considered. Additionally, fusion requires stimulation with RANKL which is modeled as a Hill function such that the probability of fusion increases and saturates at one as RANKL increases (**Supplementary Fig. 2g**):

$$f_{fusion}(RANKL) = \frac{1}{1 + \left(\frac{K_{aOC}}{RANKL}\right)} \#(2)$$

A Hill function is chosen as the functional form because it is commonly used to represent cell responses that are dependent on receptor-ligand interactions[11]. After the

1212 preosteoclasts fuse to become an osteoclast, five new preosteoclasts are randomly
1213 placed on the grid so that the number of preosteoclasts remains constant over time. To
1214 assess whether these functional forms qualitatively capture the dynamics of fusion in
1215 response to different concentrations of RANKL, we inhibit RANKL production by
1216 multiplying the production rate by scale factor π_{Ri} (**Equation 10**). As expected, the total
1217 number of osteoclasts decreases as RANKL decreases (**Supplementary Fig. 2h**).
1218
1219 *Movement*
1220 Precursor osteoclasts migrate in response to a gradient of RANKL[12,13]. We use the same
1221 technique to describe the probability of a cell remaining stationary or moving up, down,
1222 left, or right used in the original implementation of the hybrid discrete-continuum model[14]
1223 (**Equation 9**). If a preosteoclast would otherwise move in a direction that is occupied by
1224 a myeloma cell or precursor osteoblast, the two cells swap positions on the grid. This
1225 requirement underlies the assumption that fusion is not limited by spatial restrictions and
1226 is necessary in order to capture *in vivo* data showing that osteoclasts increase over time
1227 due to multiple myeloma.
1228
1229 **Active osteoclasts**
1230 In the model, active osteoclasts consist of 5 subunits to represent the size difference
1231 between osteoclasts and other cell types and to account for the fact that they are the
1232 result of the fusion of 5 preosteoclasts. In order for the osteoclast to function as a single
1233 unit, once a subunit of an osteoclast is selected for a given timestep, all of the other
1234 subunits are collected and the action for each is defined to be the same for a given
1235 osteoclast.
1236
1237 *osteoclast lifespan*
1238 We assume that the amount of bone that osteoclasts resorb is proportional to their
1239 lifespan, which we define to be normally distributed with a mean lifespan of 14 days[9],
1240 bounded between 7 and 21 days:
1241
1242 $$N(\mu_{OC}, \sigma_{OC}^2)\ within\ the\ interval\ (OC_{min}, OC_{max})\#(3)$$

1243

1244 To verify the implementation of this assumption in the model, we show that the average
1245 osteoclast lifespan per year remains constant over time (**Supplementary Fig. 1e**). The
1246 end of the bone resorption phase is followed by a reversal period, which couples bone
1247 resorption and bone formation. When an osteoclast dies, it is removed from the grid, and
1248 the cleared space is designated as eroded bone. Bone derived factors continue to be
1249 produced at a lower level for three days, which allows precursor osteoblasts to move and
1250 attach to the eroded surface. This release of BDFs could either be due to matrix
1251 metalloproteinase activity[15] or small osteoclasts that remain on the surface[16], though the
1252 source is not modeled explicitly.

1253

1254 *Osteoclast resorption*

1255 We assume that each osteoclast resorbs bone in the direction with the maximum amount
1256 of bone. Osteoclasts resorb bone tissue in areas where there is a high degree of
1257 mechanical stress or strain. There are several proposed mechanisms governing how
1258 osteoclasts detect areas of bone resorption. Integrins may play a role in guiding the
1259 direction of bone resorption by regulating the formation and orientation of the sealing
1260 zone. Specifically, integrins on the leading edge of the osteoclast are thought to sense
1261 the mechanical properties of the bone tissue and orient the osteoclast towards areas of
1262 higher mechanical stress or strain[17]. This results in the formation of a sealing zone that is
1263 oriented in the direction of the mechanical stress or strain, allowing the osteoclast to
1264 efficiently remove bone tissue from areas that are under the greatest mechanical load.
1265 Another hypothesis is that osteoclasts may be guided by the orientation of collagen fibers
1266 in bone[18]. Collagen is the main structural protein in bone, and it forms a network of fibers
1267 that give bone its strength and resilience. Studies have suggested that osteoclasts may
1268 be able to sense the orientation of collagen fibers in bone through a range of receptors
1269 and signaling pathways, and that this information may guide their resorption activity.
1270 Another hypothesis is that osteoclasts may be guided by chemical gradients of signaling
1271 molecules that are produced by other cells in the bone microenvironment[17]. By following
1272 these chemical gradients, osteoclasts may be able to target areas of bone where
1273 remodeling is needed.

1274

1275 To determine the direction, we check the Von Neumann neighborhood around each
1276 subunit of the osteoclast and record the total amount of bone in each direction. If more
1277 than one direction contains the maximum amount of bone, one of these directions is
1278 randomly selected. The bone is removed from the grid as it is resorbed and is replaced
1279 by the osteoclast. As bone is resorbed, bone derived factors are released from the bone
1280 matrix[16], which is modeled as a production term in **Equation 10**. Because the amount of
1281 bone that osteoclasts resorb is proportional to their lifespan, we verify that the average
1282 amount of bone resorbed per osteoclast per year remains constant over time
1283 (**Supplementary Fig. 1g**).

1284

1285 **Mesenchymal stem cells (MSCs)**

1286

1287 *Recruitment*

1288 MSCs have been identified in various niches within the bone marrow, and their precise
1289 location and distribution are still under investigation. Some of the most common locations
1290 where MSCs are found in the bone marrow are the endosteal region, the perivascular
1291 region, and the central marrow region[19,20]) MSCs are located in close proximity to the
1292 endosteal surface, where bone remodeling takes place, and the majority of MSCs are in
1293 contact with blood vessels or surrounded by pericytes and other undefined cells, which
1294 suggests that these cells are located in the perivascular niche[19,21]. After an osteoclast
1295 fuses, an MSC is placed on the grid within a certain radius of the osteoclast (MSC_radius),
1296 provided there is not already an MSC within the neighborhood. This requirement ensures
1297 that MSCs are located adjacent to sites of bone remodeling to couple bone resorption
1298 with bone formation[22]. However, to preserve that approximately 0.01% of the bone
1299 marrow consists of MSCs[5], MSCs that are not within a certain radius of an osteoclast are
1300 removed from the grid. Therefore, the number of MSCs fluctuates over time but is capable
1301 of returning to the initial condition.

1302

1303 *Proliferation*

1304 We assume that MSCs divide only when BDF is above a certain threshold (BDF_{thresh})
1305 (**Supplementary Fig. 2c**). The probability of cell division is
1306

1307 $$p_{div} = 1 - \left(1 - f_{div}(BDF)\right)^{TIMESTEP_AGENT} \#\#(4)$$

1308

1309 where

1310 $$f_{div}(BDF) = \begin{cases} 0 & if\ BDF < BDF_{thresh} \\ \dfrac{\rho_{MSC}}{1 + \left(\dfrac{K_{MSC}}{BDF}\right)^2} & if\ BDF \geq BDF_{thresh} \end{cases} \#$$

1311 When an MSC divides we assume it undergoes asymmetric division, producing a
1312 precursor osteoblast. The daughter cell is randomly placed in an empty grid cell within
1313 the Moore neighborhood of the MSC.
1314

1315 *Movement*

1316 MSCs migrate in the direction of higher TGF-β when there is a cytokine gradient,
1317 otherwise they move randomly[16]. As before, we use the hybrid discrete-continuum
1318 technique to describe the probability of cell movement (**Equation 9**).
1319

1320 **Preosteoblasts**

1321

1322 *Death*

1323 We assume that preosteoblasts die if they are not adjacent to eroded bone with probability
1324

1325 $$p_{death} = 1 - (1 - pOB_DEATH)^{TIMESTEP_AGENT} \quad \#(5)$$

1326

1327 or with probability one if $pOB_{age} \geq 42\ days$. Once a preosteoblast dies it is immediately
1328 removed from the grid.
1329

1330 *Proliferation*

1331 We assume that high levels of BDF promote proliferation of preosteoblasts whereas low
1332 levels promote differentiation [23]. The probability of cell division is the same as it is for
1333 MSCs (**Equation 4**; **Supplementary Fig. 2c**), except that a preosteoblast divides

symmetrically to produce another preosteoblast. As before, the daughter cell is randomly placed in an empty grid cell within the Moore neighborhood of the preosteoblast. To assess whether these model assumptions qualitatively capture the dynamics of proliferation in response to different concentrations of BDF, we inhibit BDF production by multiplying the production rate by scale factor π_{Ti} (**Equation 10**). As expected, the average proportion of preosteoblast over time decreases as BDF decreases (**Supplementary Fig. 2e**).

Differentiation

After the bone resorption phase, preosteoblasts attach to the eroded surface and differentiate due to differentiation signals provided by the exposed bone matrix[22]. In the model, preosteoblasts that are adjacent to eroded bone and exposed to low levels of bone derived factors for two weeks will differentiate into active osteoblasts (osteoblasts).

Movement

We assume the precursor osteoblasts that are not attached to eroded bone, move in response to a gradient of bone derived factors, which is modeled in the same way as for MSCs with the hybrid discrete-continuum technique (**Equation 9**).

Osteoblasts

Death

Active osteoblasts ultimately either undergo apoptosis, become osteocytes, or become quiescent bone-lining cells[9]. In the model, we assume that osteoblast death is proportional to the amount of bone that was resorbed by the osteoclast subunit that had occupied the space prior to the osteoblast (osteoclast_depth). Therefore, osteoblast death is also proportional to the average time it takes for an osteoblast to form one unit of bone (basal_time). This assumption permits the coupling of bone resorption with bone formation, since the lifespan of an osteoblast controls how much bone the osteoblast forms. Thus, bone homeostasis is maintained even when the amount of bone resorbed

by an osteoclast varies. Under normal conditions the lifespan of an osteoblast is approximately 3 months[9], which we reproduce in our model (**Supplementary Fig. 1f**). This equation describes how to define the lifespan of an aOB so that it lives long enough to replace the bone resorbed by an aOC (during homeostasis).

$$aOB_DEATH = basal_time \cdot aOC_depth \# (6)$$

Units for equation 6:

- aOB_Death: days
- basal_time: days per unit of bone
- aOC_depth: units of bone

Alternatively, an active osteoblast may unintentionally get buried in bone by itself or other osteoblasts during bone formation. This is comparable to an osteoblast becoming an osteocyte, one of its potential cell fates. In the model, this occurs if the Von Neumann neighborhood of an osteoblast only contains bone or other osteoblasts. When an osteoblast is buried, this has possible consequences for bone homeostasis since the osteoblast did not form as much bone as it would have had it completed its full lifespan. To maintain a steady state of bone, the lifespan of the nearest osteoblast is increased to allow it to build more bone to compensate for the amount lost due to the buried osteoblast. This is a simplifying assumption of the model since biologically there are many factors involved to regulate the number and lifespan of osteoblasts. However, several studies have demonstrated the ability of osteoblasts, osteocytes and other cells of the BMU to sense and communicate with one another through juxtacrine and paracrine signaling to maintain bone homeostasis, through regulate cell proliferation, lifespan and activity [24-27].

Bone Formation

We assume that the time it takes for an osteoblast to form a unit of bone is dependent on the local concentration of BDF. To determine the functional relationship between BDF and mineralization rate we use *in vitro* data from MC3T3-E1 cells cultured in osteoblastic media with various concentrations of TGF-β or the TGF-β inhibitor, 1D11 (**Supplementary Methods 2.4**). This data shows how the mineralization rate compares

to the control, specifically that it increases as TGF-β decreases (**Supplementary Fig. 2a**). We approximate this trend using an exponential decay function and extract the parameters using nonlinear least squares regression (**Supplementary Fig. 2b**):

$$f_{BF}(BDF) = (f_0 - Plateau) \cdot e^{-\delta_{BF} \cdot BDF} + Plateau \#(7)$$

This equation is unitless since it represents fold change to bone mineralization time.

To determine the time that it takes an osteoblast to form one unit of bone as a function of BDF, we scale the time it takes an osteoblast to form one unit of bone in basal levels of BDF (basal_time) by **Equation 7**:

$$Mineralization_Time(BDF) = \frac{basal_time}{f_{BF}(BDF)} \#(8)$$

Units for equation 8:

- Mineralization_Time: days per unit of bone
- basal_time: days per unit of bone

This scaling allows for mineralization to increase when BDF is below the basal level. In the model, the mineralization time for each osteoblast is updated after sufficient time has passed to form a unit of bone. To determine which direction to form bone, we impose a set of rules to try to prevent the osteoblast from becoming buried and to prevent the creation of large gaps in the placement of the bone. To do this, we first check the Von Neumann neighborhood of an osteoblast for empty space. If more than one empty space exists, the osteoblast will preferentially move to the location where it will remain in contact with at least two units of bone and is not adjacent to another osteoblast; if this is not possible, one of the empty spaces will be randomly selected. To form bone, the osteoblast moves to the empty grid cell and its previous location is replaced with a new unit of bone. Because the amount of bone that osteoblasts produce is proportional to their lifespan, we verify that the average amount of bone produced per osteoblast per year remains constant over time (**Supplementary Fig. 1h**). To assess whether these model assumptions qualitatively capture the dynamics of mineralization in response to different concentrations of BDF, we inhibit BDF production by multiplying the production rate by scale factor π_{Ti} (**Equation 10**). As expected, BDF has a biphasic effect on bone in which

low BDF results in bone loss due to lack of MSC/preosteoblast proliferation and medium BDF results in bone growth due to increased mineralization (**Supplementary Fig. 2d**).

Movement

In the model, MSCs, preosteoblasts, and MM cells migrate in the direction of higher TGF-β when there is a cytokine gradient, otherwise they move randomly[22]. preosteoclasts migrate in response to a gradient of RANKL[12,13]. We use the technique for motility described in the original implementation of the hybrid discrete-continuum model[14] to describe the probability of each cell being stationary (P_0), moving left (P_1), right (P_2), down (P_3), or up (P_4):

$$
\begin{aligned}
P_0 = 1 - \frac{4kD_n}{h^2} - \frac{k\chi}{h^2}\left(m_{i+1,j} + m_{i-1,j} + m_{i,j+1} + m_{i,j-1} - 4m_{i,j}\right) P_1 \\
= \frac{kD_n}{h^2} - \frac{k\chi}{4h^2}\left(m_{i+1,j} - m_{i-1,j}\right) P_2 = \frac{kD_n}{h^2} + \frac{k\chi}{4h^2}\left(m_{i+1,j} - m_{i-1,j}\right) P_3 \\
= \frac{kD_n}{h^2} - \frac{k\chi}{4h^2}\left(m_{i,j+1} - m_{i,j-1}\right) P_4 \\
= \underbrace{\frac{kD_n}{h^2}}_{Diffusion\ Term} + \underbrace{\frac{k\chi}{4h^2}\left(m_{i,j+1} - m_{i,j-1}\right)}_{Chemotaxis\ Term} \quad \#(9)
\end{aligned}
$$

where the subscripts specify the location on the grid, i.e., $x = ih$, $y = jh$ where $\{i, j\}$ are positive integers, k denotes the timestep, $k = \Delta t$, and h denotes the spatial step, $h = \Delta x = \Delta y$. In the absence of a gradient of chemokine m, where $m = \{R_L, T_\beta\}$, cell movement is random with diffusion coefficient D_n, whereas in the presence of a gradient cell movement is directed with chemotaxis coefficient χ.

Cytokines (RANKL and BDF)

Receptor activator of NF-κB ligand (RANKL; R_L) is a cytokine that is produced in both soluble and membrane-bound forms and can activate osteoclasts. Recently, osteocytes have been identified as a major source of RANKL[28,29]. Once a microfracture occurs,

RANKL is produced at the rate α_R at five adjacent cells on the perimeter of bone, which then diffuses in two spatial dimensions and degrades at the rate δ_R.

Bone derived factors (BDFs; T_β) consist of the group of cytokines that are released during bone remodeling, including TGF-β and IGF. These cytokines are produced in a latent form by many other cell types, including T-cells, macrophages, and platelets[30]. Instead of modeling the production of BDF explicitly by these other cell types, we assume that BDFs are constantly produced at rate α_B, and further produced at rate α_T while bone is resorbed by osteoclasts. We assume that BDF also diffuses in two spatial dimensions and degrades at rate δ_T.

$$\begin{aligned}\frac{\partial R_L(x,y,t)}{\partial t} &= D_R\underbrace{\left(\frac{\partial^2 R_L}{\partial x^2}+\frac{\partial^2 R_L}{\partial y^2}\right)}_{Diffusion} + \pi_{Ri}\alpha_R \underbrace{B_{i,j}}_{Production} \\ &- \delta_R \underbrace{R_L}_{Decay}\frac{\partial T_\beta(x,y,t)}{\partial t} \\ &= D_T\underbrace{\left(\frac{\partial^2 T_\beta}{\partial x^2}+\frac{\partial^2 T_\beta}{\partial y^2}\right)}_{Diffusion} + \pi_{Ti}\alpha_B \underbrace{}_{Basal\ Production} \\ &+ \pi_{Ti}\alpha_T \underbrace{B_{i,j}C_{i,j}}_{Production} - \delta_T \underbrace{T_\beta}_{Decay} \quad \#(10)\end{aligned}$$

where

$$\Omega_{i,j} = \{\, 1 \quad if\ \Omega\ at\ (x_i, y_j)\ \ 0 \qquad otherwise \quad \Omega = bone\ cell\ (B)\ or\ osteoclast\ (C)$$

Boundary conditions of PDE grid

The system of PDEs is solved using the forward time centered space (FTCS) scheme with periodic boundary conditions imposed on all sides of the domain, which is implemented using the diffusion function in HAL. The timestep is chosen to ensure numerical stability, i.e., $\frac{D\Delta t_{diff}}{(\Delta x)^2} < \frac{1}{4}$.

1.2. Incorporating Multiple Myeloma

Preosteoclasts

1482 *Fusion*

1483 Multiple myeloma cells enhance RANKL expression in the bone microenvironment which
1484 leads to increased osteoclastogenesis[31]. In the model, we assume that if there are three
1485 or more myeloma cells within the Moore neighborhood of a bone cell located on the
1486 perimeter of bone, a new bone remodeling event is initiated. As described above, each
1487 bone remodeling event is characterized by RANKL expression from five adjacent cells on
1488 the perimeter of bone.

1489

1490 **Mesenchymal stem cells (MSCs)**

1491

1492 *Recruitment*

1493 Multiple myeloma cells produce chemoattractants that recruit MSCs to the bone
1494 marrow[32]. We assume that one MSC is recruited per 50 myeloma cells, and that once it
1495 is recruited, an MSC remains in the bone marrow (data not shown).

1496

1497 *Proliferation*

1498 Myeloma cells inhibit the differentiation of mesenchymal stromal cells through soluble
1499 factors and cell-cell contract[33]. In the model, we assume that the differentiation of MSCs
1500 to precursor osteoblasts occurs through asymmetric division. To capture the effect of
1501 myeloma cells on osteoblast differentiation, we assume that MSCs do not divide if they
1502 are within a certain radius of a myeloma cell (MM_radius).

1503

1504 **Preosteoblasts**

1505

1506 *Differentiation*

1507 Myeloma cells inhibit the differentiation of osteoblast progenitors through soluble factors
1508 and cell-cell contract[22]. In the model, we assume that preosteoblasts do not differentiate
1509 if they are within a certain radius of a myeloma cell (MM_radius),

1510

1511 **Multiple Myeloma**

1512

1513 *Initiation*

1514 A single myeloma cell is recruited within a certain radius of an osteoclast after the first
1515 osteoclast fusion event occurs.

1516

1517 *Death*

1518 The bone marrow microenvironment supports the growth and survival of multiple
1519 myeloma cells[34]. To determine where myeloma cell death and division occur spatially in
1520 the microenvironment, we measured the distance of these cells to the nearest bone
1521 (**Supplementary Methods 2.8**; **Fig. 3a-d**). Because there is less cell death close to bone,
1522 we assume that multiple myeloma cell death (sensitive and resistant cells) is dependent
1523 on the local concentration of BDF. The probability of cell death is

1524

1525 $$p_{death} = 1 - (1 - MM_{DEATH})^{TIMESTEP_AGENT} \#(11)$$

1526 where

1527 $$MM_{DEATH} = \{ \begin{array}{ll} MM_DEATH & if\ BDF < BDF_{thresh} \\ MM_DEATH_BDF & if\ BDF \geq BDF_{thresh} \end{array} \#$$

1528

1529 *Proliferation*

1530 We assume that myeloma cell division is dependent on the concentration of BDF and has
1531 maximum rate ρ_X. This maximum rate is dependent on if the myeloma cell is sensitive or
1532 resistant, since we showed that the U266 cell line has a cost of resistance
1533 (**Supplementary Fig. 7a-b**). Furthermore, we and others have shown that myeloma cell
1534 division increases near MSC/preosteoblast[35] (**Fig. 3f** and **Fig. 6a**). To incorporate this
1535 into the model, we assume that sensitive cells within a certain radius of an MSC or
1536 preosteoblast divide faster than sensitive cells that are not close to an MSC or
1537 preosteoblast (**Fig. 3g**), which divide faster than resistant cells. We define the probability
1538 of cell division with the following Hill function:

1539

1540 $$f_{div}(BDF) = \frac{\rho_X}{1 + \left(\frac{K_X}{BDF}\right)^2} \#(12)$$

1541 where $\rho_X = \{MAX_MM_DIV, MAX_MM_DIV_MSC, MAX_R_MM_DIV\}$ and
1542 $K_X = \{K_{MM}, K_{MM_MSC}, K_{R_MM}\}$ depending on if the myeloma cell is sensitive, resistant,

and/or within a certain radius of an MSC or preosteoblast (protect_radius). A Hill function is chosen as the functional form because it is commonly used to represent cell responses that are dependent on receptor-ligand interactions[11].

1.3. Incorporating Bortezomib

Preosteoclasts

Fusion

Bortezomib inhibits osteoclast differentiation *in vitro* in a dose-dependent manner[25]. To incorporate this into the model we multiply the probability of fusion (**Equation 2**) by a repressive Hill function so that the probability decreases as dose increases (**Supplementary Fig. 3d**):

$$f_{fusion_BTZ}(RANKL, Dose) = f_{fusion}(RANKL) \cdot \frac{1}{1 + \left(\frac{Dose}{K_{dose}}\right)^2} \#(13)$$

As expected, the total number of osteoclasts decreases as dose increases (**Supplementary Fig. 3g**).

Osteoblasts

Bone Formation

Bortezomib enhances the mineralization rate of osteoblasts *in vitro* in a dose-dependent manner (**Supplementary Fig. 3b**). To incorporate this into the model we scale the mineralization time (**Equation 8**) linearly so that at maximum dose (Dose = 1) the time it takes an osteoblast to form a unit of bone is reduced by half (**Supplementary Fig. 3c**):

$$Mineralization_Time_BTZ(BDF, Dose) = \frac{Mineralization_Time(BDF)}{Dose + 1} \#(14)$$

As expected, the BA/TA increases as dose increases (**Supplementary Fig. 3f**) due to increased production of bone per osteoblast.

Multiple Myeloma

Death

We assume that Bortezomib treatment does not affect the probability of cell death for resistant cells. On the other hand, Bortezomib decreases viability for sensitive cells *in vitro* and slows growth *in vivo* in a dose-dependent manner (**Supplementary Fig. 3a** and **Fig. 6c**)[36]. *In vivo*, failure to eradicate the disease may be due to both cell intrinsic mechanisms such as mutations, alterations in signaling pathways, copy-number alterations, epigenetic changes, and cell extrinsic mechanisms such as environment mediated drug resistance (EMDR)[37]. EMDR is when myeloma cells are transiently protected from Bortezomib due to factors or interactions with other cells in the bone microenvironment, which we define in our model to be when bone derived factors are above a certain threshold or MSCs or preosteoblasts are within a certain radius of a myeloma cell[32]. The probability of cell death during Bortezomib treatment is (**Supplementary Fig. 3i**):

$$p_{death} = 1 - (1 - MM_{DEATH})^{TIMESTEP_AGENT} \#(15)$$

where

$$\begin{aligned}
MM_{DEATH} = \{ & \; MM_DEATH && if\ RESISTANT\ and\ BDF \\
< BDF_{thresh} & \; MM_DEATH_BDF && if\ RESISTANT\ and\ BDF \\
\geq BDF_{thresh} & \; MM_DEATH(1 + 1.5 \cdot Dose) && if\ SENSITIVE\ and\ BDF \\
< BDF_{thresh} & \; and\ no\ MSC \\
/pOB & \; MM_EMDR_DEATH && if\ SENSITIVE\ and\ BDF \\
\geq BDF_{thresh} & \; or\ MSC/pOB\ \#
\end{aligned}$$

Therefore, tumor response to Bortezomib treatment depends on dose as well as the presence of bone derived factors or MSCs/preosteoblasts. At high dose, it is possible to

1601 completely eradicate the tumor in the absence of EMDR, similar to what is observed in *in*
1602 *vitro* experiments (**Supplementary Fig. 3j**).
1603
1604 *Proliferation*
1605 Once treatment is initiated, myeloma cells have a probability of developing resistance (p_Ω)
1606 during cell division that would cause the cell to become resistant to bortezomib.
1607
1608 **Dose selection**
1609
1610 *Bortezomib*
1611 We define dose to be between 0 and 1, where 0 represents no treatment and 1 represents
1612 the maximum dose, i.e., the dose that is sufficient to kill off sensitive cells without having
1613 a major impact on normal bone cells such as MSCs and preosteoblasts. Based on the *in*
1614 *vitro* cell viability assay, we define maximum dose to be 10 nM (**Supplementary Fig. 3a**).
1615
1616 **1.4. Parameter Exploration**
1617 Parameter estimates used in the HCA model may vary widely based on the experimental
1618 design. For example, MM cell proliferation and death rates vary depending on the MM
1619 cell line used, growth media, and/or cell-cell interactions. To test whether our results are
1620 dependent on a particular parameter value, select parameters were varied to assess how
1621 the relapse time (when MM burden reached 20% of the marrow) and proportion of
1622 sensitive cells at endpoint changed under continuous bortezomib treatment
1623 (**Supplementary Fig. 10**). We found that the parameter controlling the impact of EMDR
1624 had a more striking effect on the proportion of sensitive cells at endpoint instead of the
1625 relapse time (**Supplementary Fig. 10b**), whereas the parameter controlling the cost of
1626 resistance had an impact on both outputs in the presence of EMDR (**Supplementary Fig.**
1627 **10c**). Furthermore, the parameter controlling the survival advantage of BDF under no BTZ
1628 treatment conditions had only a minor impact on either output (**Supplementary Fig. 10d**),
1629 whereas the parameter controlling the proliferative advantage of sensitive cells in the
1630 presence of MSC/preosteoblast had a strong effect on the proportion of sensitive cells at
1631 endpoint. However, when the proliferative advantage is sufficiently strong, minimal

residual disease may be present in the presence or absence of EMDR, though the proportion is higher with EMDR (**Supplementary Fig. 10e**). This analysis shows that although the proportion of sensitive cells at endpoint varied, our finding that EMDR maintains a reservoir of sensitive cells was robust for these parameters. Furthermore, we showed that EMDR consistently led to a higher proportion of tumors that relapsed, except when the proliferative advantage due to MSC/preosteoblast was sufficiently large.

1.5. Parameters

The HCA model contains a large number of parameters as it has six different cell types and two microenvironmental factors. Many of the parameters were difficult to obtain and had to be estimated. Because many of the cell actions, such as proliferation and chemotaxis, result from the combination of parameters rather than a single value, our goal is to capture key outputs such as bone remodeling homeostasis instead of precisely parameterizing the model.

Supplementary Table 1: Grid Parameters

Grid Parameter	Description	Value	Units	Source
$\boldsymbol{SPACESTEP}$ $(\Delta \boldsymbol{x})$	Space step of HCA grid	10.0	μm	Estimated*
$\boldsymbol{TIMESTEP_AGENT}$ $(\Delta \boldsymbol{t_{cells}})$	Cell timestep	0.1	$hour$	Assumed
$\boldsymbol{N_TIMESTEP_PDE}$	Number of diffusion timesteps per agent timestep	360	number	Assumed
$\boldsymbol{TURNOVER_TIME}$	Turnover time of trabecular bone	35040	$hours$	[9]
$\boldsymbol{xDim}$	Length of HCA grid	1600	μm	Assumed
$\boldsymbol{yDim}$	Height of HCA grid	1500	μm	Assumed

- *SPACESTEP*. We assume that $1\ pixel\ =\ 10\ \mu m$, the diameter of a myeloma cell (experimentally derived)

Supplementary Table 2: BDF/RANKL Parameters

BDF/RANKL Parameter	Description	Value	Units	Source

---	TGF-β in bone	0.2	ng/mg	[38]
$\boldsymbol{TGFB_DiffCoef}$ $(\boldsymbol{D_T})$	BDF diffusion coefficient	780	$\mu m^2/min$	[39-42]
$\boldsymbol{RANKL_DiffCoef}$ $(\boldsymbol{D_R})$	RANKL diffusion coefficient	780	$\mu m^2/min$	Assumed
$\boldsymbol{TGFB_productionRate}$ $(\boldsymbol{\alpha_T})$	BDF production rate	2.04×10^{-9}	$(ng/\mu m^3) \cdot cell_{unit}^{-1} \cdot min^{-1}$	Estimated*
$\boldsymbol{RANKL_productionRate}$ $(\boldsymbol{\alpha_R})$	RANKL production rate	2.04×10^{-9}	$(ng/\mu m^3) \cdot cell_{unit}^{-1} \cdot min^{-1}$	Assumed $\alpha_R = \alpha_T$
$\boldsymbol{TGFB_basalRate}$ $(\boldsymbol{\alpha_B})$	BDF basal production rate	2.04×10^{-11}	$(ng/\mu m^3) \cdot min^{-1}$	Estimated*
$\boldsymbol{TGFB_decayRate}$ $(\boldsymbol{\delta_T})$	BDF decay rate	0.35	min^{-1}	[43]
$\boldsymbol{RANKL_decayRate}$ $(\boldsymbol{\delta_R})$	RANKL decay rate	0.35	min^{-1}	Assumed $\delta_R = \delta_T$
$\boldsymbol{maxTGFB}$ $(\boldsymbol{BDF_{max}})$	Maximum BDF at given location	8.7×10^{-10}	$ng/\mu m^3$	Estimated
$\boldsymbol{Ts}$ $(\boldsymbol{BDF_{basal}})$	Basal BDF	$\frac{\alpha_B}{\lvert\delta_T\rvert \cdot BDF_{max}}$	$unitless$	Estimated
$\boldsymbol{TGFBthresh}$ $(\boldsymbol{BDF_{thresh}})$	Threshold BDF	$1.05 \cdot BDF_{basal}$	$unitless$	Assumed
$\boldsymbol{maxRANKL}$ $(\boldsymbol{RANKL_{max}})$	Maximum RANKL at given location	1.7×10^{-9}	$ng/\mu m^3$	Estimated
$\boldsymbol{Extra_TGFBtime}$	Duration of BDF expression during reversal phase	72	$hours$	Assumed
$\boldsymbol{max_RANKL_on}$	Maximum duration of RANKL	336	$hours$	Assumed

- *TGF-β diffusion rate,* D_T. The $780\ \mu m^2/min$ was estimated using the molecular weight of TGF-β (25 kDa [39]). A molecule of molecular weight (M) 0.3-0.5 kDa has a diffusion coefficient of approximately $10^{-6}\ cm^2/s$ [40]. The plot of $log\ log\ (D)$ vs. $log\ log\ (M)$ correlates with a line of slope $-\frac{1}{3}$ [41]. Thus, we solve

  $(D) = (10^{-6}) + \frac{1}{3}\big((0.5) - (25)\big)$

to get $D = 2.6 \times 10^{-7}\ cm^2/s = 1560\ \mu m^2/min$. Small molecules diffuse through the extracellular space with an effective diffusion coefficient that is two to three times less than the free diffusion coefficient[42], thus $D^* = D/2 = 780\ \mu m^2/min$.

- *TGF-β production rate, α_B.*
    - Volume of resorption pit: $\pi r^2 h = \pi(25^2)(10) = 19634.95\ \mu m^3/day$, where r = radius of osteoclast and h = amount of bone resorbed per day
    - Rate of bone resorption by a $50\ \mu m$ OC: Given the density of bone = $1500\ kg/m^3$ [44], $(1500\ kg/m^3) \times (19634.95\ \mu m^3/day) \times (10^{-18}\ m^3/\mu m^3) = 2.945 \times 10^{-11}\ kg/day = 2.945 \times 10^{-5}\ mg/day$
    - TGF-β released/day due to bone resorption by a 50 μm OC: Given concentration of TGF-β in bone is 0.5 ng/mg [38], $(2.945 \times 10^{-5}\ mg/day) \times (0.5\ ng/mg) = 1.47 \times 10^{-5}\ ng/day$. Because a $50\ \mu m$ OC takes up 5 pixels, we divide this by 5 to get: $2.94 \times 10^{-6}\ ng \cdot cell_{unit}^{-1} \cdot day^{-1} = 2.04 \times 10^{-9}\ ng \cdot cell_{unit}^{-1} \cdot min^{-1}$, consistent with [45]. We convert this to units of ng per volume to be consistent with the units of chemotaxis, which requires dividing the amount (ng) by the soluble volume of each grid point. Because the soluble volume fraction is unknown, we set $\alpha_T = 2.04 \times 10^{-9}\ (ng/\mu m^3) \cdot cell_{unit}^{-1} \cdot min^{-1}$, which was calibrated to reproduce the steps of normal bone remodeling.

- *TGF-β basal production rate, α_B.* We assume that BDF is produced at a higher rate through bone resorption compared to other sources in HCA[22]
- *TGF-β decay rate, δ_T:* The half-life of *TGF-β* is 2 minutes[44]. Thus, the decay rate is $\frac{ln ln\ (2)}{2} = 0.35\ min^{-1}$.
- maxTGFβ was determined by running the unnormalized model a number of times and then recording the maximum TGFβ at a single grid point. This value of BDF was then set as maxTGFβ. The maximum TGFβ is printed after each model is run (tmax) so that it can be monitored whether the value stays between 0 and 1.
- Ts is the basal BDF and is defined as written in the table, $\alpha_B/(|\delta_T| \cdot BDF_{max})$ .This is the amount of BDF that is always present on the grid.
- MaxRANKL was determined by running the unnormalized model a number of times and then looking at the output "preosteoblastborn.csv" to evaluate the maximum value of RANKL that occurred when an osteoclast formed. This value of RANKL was then set as maxRANKL so that most values of RANKL that lead to the formation of an osteoclast are between 0 and 1 (however, it is possible that some values in future runs of model are not strictly below 1).

Supplementary Table 3: preosteoclast/osteoclast Parameters

preosteoclast/osteoclast Parameter	Description	Value	Units	Source
$\boldsymbol{pOC_DiffCoef}$	preosteoclast random motility	0.3	$\mu m^2/min$	Estimated
$\boldsymbol{pOC_TaxisCoef}$	preosteoclast chemotaxis coefficient	5×10^{10}	$\mu m^2 min^{-1} (ng/\mu m^3)^{-1}$	Estimated
$\boldsymbol{K_{aOC}}$	Half-maximal concentration constant	0.01	$concentration$	Assumed
$\boldsymbol{\mu_{OC}}$	Mean osteoclast lifespan	14	$days$	[9,46]
$\boldsymbol{\sigma_{OC}}$	osteoclast lifespan standard deviation	7/3	$days$	Assumed
$\boldsymbol{OC_{min}}$	Minimum osteoclast lifespan	7	$days$	Assumed
$\boldsymbol{OC_{max}}$	Maximum osteoclast lifespan	21	$days$	Assumed
$\boldsymbol{MAX_FUSION_RATE}$	Maximum fusion rate	$1/72$	$hours^{-1}$	[47]
$\boldsymbol{Unit_RESORPTION}$	Time to resorb one unit of bone	1	day	[48]
$\boldsymbol{aOC\ diameter}$	Diameter of osteoclast	50	μm	[10]

- *Random motility coefficient of cell, preosteoclast_DiffCoef*: Stokes-Einstein relation: $D = \frac{k_B T}{6\pi\eta a}$. Given $k_B = 1.38 \times 10^{-23}\ N \cdot m, T = 310\ K$ (body temp: $310\ K$; room temp: $300\ K$), $\eta = 10^{-3}\ N \cdot s/m^2$ (viscosity of water), $a = 5\ \mu m$ (cell radius), $D = 4.54 \times 10^{-10} cm^2 s^{-1} = 3\ \mu m^2/min$. We assume that preosteoclast random motility is 10-fold slower in bone marrow compared to water.

Supplementary Table 4: MSC/preosteoblast/osteoblast Parameters

MSC/preosteoblast/osteoblast Parameter	Description	Value	Units	Source
$\boldsymbol{MSC_DiffCoef = pOB_DiffCoef}$	MSC/preosteoblast random motility	0.03	$\mu m^2/min$	Estimated

$\boldsymbol{MSC_TaxisCoef}$	MSC chemotaxis coefficient	5×10^9	$\mu m^2 min^{-1} (ng/\mu m^3)^{-1}$	Estimated
$\boldsymbol{pOB_TaxisCoef}$	preosteoblast chemotaxis coefficient	5×10^{11}	$\mu m^2 min^{-1} (ng/\mu m^3)^{-1}$	Estimated
$\boldsymbol{K_{MSC} = K_{pOB}}$	Half-maximal concentration constant	$\sqrt{3} \cdot BDF_{thresh}$	$unitless$	Assumed
$\boldsymbol{MAX_MSC_DIVISION_RATE = MAX_pOB_DIVISION_RATE}$ $(\boldsymbol{\rho_{MSC} = \rho_{pOB}})$	Maximum proliferation rate	$1/24$	$hour^{-1}$	Assumed
$\boldsymbol{pOB_DEATH}$	preosteoblast death rate	$1/72$	$hour^{-1}$	Assumed*
$\boldsymbol{pOB_DIFF}$	preosteoblast differentiation time	336	$hour$	Determined from experiments
$\boldsymbol{MSC_radius}$	Radius around osteoclast/MM to recruit MSC	40	μm	Assumed*
$\boldsymbol{MM_radius}$	Radius of MM effect on MSC/preosteoblast differentiation	80	μm	Assumed*
$\boldsymbol{Y0}$ $(\boldsymbol{f_0})$	Maximum fold change	5.055	$unitless$	Estimated*
$\boldsymbol{Plateau}$	Minimum fold change	0.5379	$unitless$	Estimated*
$\boldsymbol{scalefactor}$	Scale factor	$\frac{19.2}{BDF_{basal}}$	$unitless$	Estimated*
$\boldsymbol{k}$ $(\boldsymbol{\delta_{BF}})$	Fold change decay constant	$0.1136 \cdot scalefactor$	$unitless$	Estimated*

$\boldsymbol{basal_time}$	Basal unit bone formation time	9	$days$	[49]

- *Random motility coefficient of cell, MSC_DiffCoef, preosteoblast_DiffCoef*: We assume that MSC and preosteoblast random motility is 100-fold slower in bone marrow compared to water, and 10 fold slower than preosteoclast.
- *Chemotaxis coefficient, MSC_TaxisCoef, preosteoblast_TaxisCoef*: The chemotaxis coefficient of human neutrophils in response to the tripeptide FNLLP is $150\ cm^2 s^{-1} M^{-1} \approx 5.18 \times 10^{-2} mm^2 (pg/mm^3)^{-1} day^{-1} = 3.6\ \times 10^{13} \mu m^2 (ng/\mu m^3)^{-1} min^{-1}$ (using 25 kDa as the molecular weight of TGF-β)[50,51]. However, to give reasonable model outputs required us to calibrate this parameter further and assume that MSC_TaxisCoef < preosteoblast_TaxisCoef.
- *preosteoblast death rate, preosteoblast_DEATH*: Assumed to be same as preosteoclast[47]
- *MSC recruitment radius, MSC_radius*: Defined so that MSC is close enough to respond to BDF generated by osteoclast
- *MM radius of impact on MSC/preosteoblast, MM_radius*: Defined so that MSC/preosteoblast responds to MM even when not directly adjacent. This assumption was necessary since HCA assumes MM is unable to migrate towards MSC/preosteoblast in absence of BDF, which created distance between MM and MSC/preosteoblast.
- *Exponential decay* (**Equation 7**)*: Y0, Plateau, k*: These values were estimated by using an exponential decay function and nonlinear least squares regression with *in vitro* data from MC3T3-E1 cells cultured in osteoblastic media with various concentrations of TGF-β or the TGF-β inhibitor, 1D11 (**Supplementary Methods 2.4**).

Supplementary Table 5: MM Parameters

MM Parameter	Description	Value	Units	Source
$\boldsymbol{MM_DiffCoef}$	MM random motility	0	$\mu m^2/min$	Assumed
$\boldsymbol{MM_TaxisCoef}$	MM chemotaxis coefficient	5×10^9	$\mu m^2 min^{-1} (ng/\mu m^3)^{-1}$	Estimated
$\boldsymbol{MM_DEATH}$	MM basal death rate	$1/120$	$hour^{-1}$	Assumed*

$\boldsymbol{MM_EMDR_DEATH}$	MM death rate with EMDR	$1/120$	$hour^{-1}$	Assumed*
$\boldsymbol{MM_DEATH_BDF}$	MM death rate with BDF	$1/1200$	$hour^{-1}$	Assumed*
$\boldsymbol{MAX_MM_DIVISION_RATE}$	Maximum proliferation rate	$1/24$	$hour^{-1}$	Estimated
$\boldsymbol{MAX_MM_DIV_MSC}$	Maximum proliferation rate	$1/24$	$hour^{-1}$	Assumed
$\boldsymbol{MAX_RESISTANT_DIVISION_RATE}$	Maximum proliferation rate	$1/48$	$hour^{-1}$	Estimated
$\boldsymbol{K_{MM}}$	Half-maximal concentration constant	$\sqrt{3} \cdot BDF_{thresh}$	$unitless$	*
$\boldsymbol{K_{MM_MSC}}$	Half-maximal concentration constant	BDF_{basal}	$unitless$	*
$\boldsymbol{K_{R_MM}}$	Half-maximal concentration constant	$\sqrt{1.25} \cdot BDF_{basal}$	$unitless$	*
$\boldsymbol{protect_radius}$	Radius of MM birth/death advantage from MSC/preosteoblast	20	μm	Assumed
$\boldsymbol{p\ resistance(p_{\Omega})}$	Resistance probability	$variable$	unitless	Assumed

- *Random motility coefficient of cell, MM_DiffCoef*: We assume that MM cells do not have random motility.
- *Chemotaxis coefficient, MM_TaxisCoef*: We assume that MM_TaxisCoef = MSC_TaxisCoef.
- *MM death rates, MM_DEATH, MM_EMDR_DEATH, MM_DEATH_BDF*: We assume that the lifespan of MM is similar to short-lived (3-5 days) and long-lived (several months) plasma cells[52]

- *Half maximal constant, K_{MM}*. We set $K_{MM} = \sqrt{3} \cdot BDF_{thresh}$, the value of BDF for which the myeloma proliferation rate is half maximum. This is estimated under the assumption that when $BDF = BDF_{thresh}$, i.e., when BDF is slightly above the basal level that is constantly present, the proliferation rate = 1/96 hour^{-1}. This value is based on the doubling time of myeloma cells *in vivo*.
- *Half maximal constant, K_{MM_MSC}*. We set $K_{MM_MSC} = BDF_{basal}$, which is estimated under the assumption that when $BDF = BDF_{basal}$, i.e. in locations in the bone marrow that are not close to bone resorption, the myeloma proliferation rate = 1/48 hour^{-1} in the presence of MSC/preosteoblast (i.e. half the maximum proliferation rate).
- *Half maximal constant, K_{R_MM}*. We set $K_{R_MM} = \sqrt{1.25} \cdot BDF_{basal}$, which is estimated so that when $BDF = BDF_{basal}$, the division rate of resistant myeloma cells is less than the division rate of sensitive myeloma cells and remains greater than the death rate in the absence of Bortezomib treatment.

Supplementary Table 6: BTZ Parameters

BTZ Parameter	Description	Value	Units	Source
$\boldsymbol{K_{dose}}$	Half-maximal concentration constant	0.05	$unitless$	Assumed

2. Biological Supplementary Methods

2.1. Cell culture

Human proteasome inhibitor sensitive (U266) myeloma cell and their proteasome inhibitor resistant derivatives (PSR[53,54]) were a kind gift from Dr. Steven Grant at the University of Virginia, VA. U266 and PSR were transduced using QIAGEN lentiviral particles (CLS-PCG-8 or CLS-PCR-8) according to manufacturer's instructions to express GFP and RFP respectively, generating U266-GFP and PSR-RFP. These cells were cultured in RPMI containing 10% FBS (PEAK), 1% penicillin-streptomycin. MCSF-generated macrophages were isolated as previously described[55,56]. Briefly, tibia and femur were harvested from 6-week-old C57Bl/6 RAG2-/- mice. Bone marrow cells were collected by centrifugation (10,000 g, 15s) cells were plated aMEM (+/+) containing 10% FBS (Peak), 1% penicillin-streptomycin and MCSF (300-25, Peprotech; 30ng/ml). Adherent macrophages were collected and used for downstream experiments after 72 hours. Murine mesenchymal

1757 stromal cells (MSCs) were isolated as previously described[57]. Human MSCs (PT-2501)
1758 and the murine preosteoblast cell line, MC3T3-E1 were purchased from Lonza and
1759 ATCC, respectively. Mouse MSCs and MC3T3-E1 cells were cultured in aMEM (-/-)
1760 containing 1% penicillin-streptomycin and 15 or 10% FBS (PEAK), respectively. Human
1761 MSCs were cultured as above except with 10% qualified FBS (Gibco).
1762

1763 **2.2. MTT Assay**

1764 Myeloma cell lines, mouse MSCs or MC3T3-E1 were plated in 96-well plates at a density
1765 of 1×10^4 cells/well. Cells were treated with vehicle or a range of concentrations of
1766 zoledronate or bortezomib. Cell viability was assessed at 72 hours by the MTT assay
1767 following the manufacturer's instructions (CellTiter 96, #G3582, Pierce.) The absorbance
1768 was measured at 490nm after 3 hours of incubation at 37°C.
1769

1770 **2.3. Osteoclastogenesis Assay**

1771 Osteoclast formation assays were performed using murine MCSF-generated
1772 macrophages as previously described[55,56]. Briefly, MCSF-generated macrophages from
1773 4–6-week-old C57Bl/6 RAG2-/- mice were plated in a 96-well plate ($25x10^3$ cells/well) in
1774 triplicate with MCSF (30ng/ml) and allowed to adhere for 24 hours. RANKL (315-11C,
1775 Peprotech) was given at the indicated doses with M-CSF on days 1 and 3. Cultures were
1776 fixed with 4% paraformaldehyde on day 5 and TRAcP stained. TRAcP positive
1777 multinucleated (>3) were deemed osteoclasts.
1778

1779 **2.4. Osteoblast mineralization assay**

1780 Mouse MSCs, MC3T3-E1 cells or human MSCs (huMSCs) were differentiated with 1X
1781 StemXVivo mouse/rat or human osteogenic supplement (CCM009; R&D Systems) for
1782 indicated number of days. To assess the effect increased TGF-β has on OB
1783 differentiation, either exogenous human TGF-β1 (240-B; R&D systems) or vehicle (PBS)
1784 was added to cultures. To assess the effect decreased TGF-β levels have on OB
1785 differentiation, either anti-TGF-β antibody (1D11; R&D systems) or isotype control (13C4;
1786 R&D systems) was added to cultures. OB mineralization was assessed by Alizarin red
1787 staining as previously described[55,56]. Conditioned medium was generated from huMSCs

1788 or huMSCs differentiated for 7-28 days in osteogenic supplement by incubating cells in
1789 standard aMEM for 24hours.
1790
1791 **2.5. MM-MSC and sensitive/resistant MM co-culture assays**
1792 Human MSCs (huMSCs; Lonza) were plated (2000 cells/100ul) or media alone in a 96
1793 well plate and allowed to adhere overnight. The following day 50% of the media was
1794 removed and replaced with media containing U266-GFP+ MM cells in standard RPMI.
1795 Plates were centrifuged at 200g for 5 minutes to facilitate adhesion to MSCs. After 3
1796 hours, bortezomib was added at indicated concentrations. Images were taken at 0 and
1797 72 hours. The area covered by GFP+ MM cells was calculated in Fiji software[58]. U266-
1798 GFP and PSR-RFP (10,000 total cells/well,) were plated at indicated ratios in a 96-well
1799 plate with indicated concentrations of bortezomib. Cell confluency for GFP and RFP
1800 populations was measured every 12 hours using Incucyte S3. For long term (60 day and
1801 30 day cultures). Cultures were set up as previously described. BTZ (10nM) was given
1802 over 72 hour periods and PI-sensitive U266 and PI-resistant PSR confluency was
1803 measured by fluorescent markers using the incucyte SX5. After treatment, media was
1804 replaced, after PBS washing, with standard RPMI. Images were taken at indicated
1805 timepoints with EVOS FL auto prior to media changes.
1806
1807 **2.6. Flow cytometry**
1808 Left tibiae were used to assess tumor burden by GFP expression. Tibial ends were
1809 excised, whole bone marrow was isolated by centrifugation at 10,000g for 10 seconds.
1810 Red blood cells were lysed by RBC lysis buffer (R7757, Sigma-Aldrich) as per
1811 manufacturers guidelines. Bone marrow cells were subject to viability staining with
1812 Zombie Near-Infrared (NIR; 1:500; 423105, BioLegend). Appropriate compensation and
1813 fluorescence-minus-one (FMO) controls were generated in parallel either with aliquots of
1814 bone marrow cells or $U266^{GFP+/-}$. Stained controls and samples were analyzed using BD
1815 Biosciences LSRII flow cytometer. The percentage of GFP-expressing cells was gated
1816 on singlet live bone marrow cells in FCS Express 7. To address the proliferative
1817 advantages provided by cells of the BME to MM cells, U266 MM cells were stained with
1818 CM-DIL (Invitrogen; V22888) according to the manufacturer's instruction and incubated

1819 with 50% (v/v) control, MSC, preosteoblasts (Day 7 or 14) or OB (day 21 or 28)
1820 conditioned media for 7 days, with media changes every 3 days. An aliquot of untreated
1821 CM-DIL+ cells was stained with Zombie NIR as above and used for baseline time point.
1822 At the end of the experiment, MM cells were stained with Zombie NIR for live/dead
1823 discrimination. The MFI for the CM-DiI channel was calculated at baseline and after 72
1824 hours on live single cell cells using appropriate FMO controls. FCS Express 7 was used
1825 to calculate the proliferative index of these cells.
1826

1827 **2.7. Microcomputed Tomography**

1828 Harvested right tibiae were fixed in 4% paraformaldehyde for 48 hours. Tibiae from mice
1829 from all time points were centralized and were subjected to micro-computed topography
1830 (µCT) scanning using SCANCO µ35 scanner to elucidate bone volume data at the
1831 proximal tibial metaphases. Individual bone scans were deidentified using numerical
1832 codes during, and reidentified post analyses in a blinded fashion. Evaluation of trabecular
1833 bone microarchitecture was performed in a region that consisting of 1000 µm, beginning
1834 500µm from the growth plate. A three-dimensional cubical voxel model of bone was built,
1835 and calculations were made for relative bone volume per total volume (BV/TV), trabecular
1836 number (Tb.N), trabecular thickness (Tb.Th), trabecular spacing (Tb.Sp) and connectivity
1837 density (Conn.D).
1838

1839 **2.8. Immunofluorescence**

1840 Tibiae were decalcified in an excess of 10% EDTA for 21 days, refreshing EDTA every
1841 48 hours before being placed in 30% sucrose (w/v) for 48 hours and subsequent
1842 cryosectioning. Tibia were mounted on Superfrost Plus slides (Fisher) with optimal cutting
1843 temperature (OCT) media and frozen on dry ice. Using a cryostat, 20 µm sections were
1844 made and stored at -80°C. For immunofluorescence, sections were kept on a slide
1845 warmer overnight at 56°C. Sections were rehydrated for 30 minutes at room temperature
1846 in PBS. Sections were blocked with 10% (v/v) normal goat serum and washed in PBS
1847 before staining addition of primary antibodies. Sections were incubated overnight at 4°C
1848 with primary rabbit antibodies at a dilution of 1:100 (anti-pHH3; 06-570 Millipore, anti-
1849 Osterix; ab22552, abcam: anti-aSMA: PA5-16697, Invitrogen,). Subsequently, slides

1850 were washed thrice in PBS and stained with goat anti-rabbit Alexa Fluor-647-conjugated
1851 secondary antibody (1:1000) at room temperature for 1h. DAPI (1ng/ml) was used as a
1852 nuclear counterstain. Mounted sections were imaged using 10X image tile-scans of whole
1853 tibia. The number of pHH3+ nuclei that co-localized with GFP+ cells were counted and
1854 the distance to nearest bone (tibia or cortical) was calculated. For MSC analyses, the
1855 percentage of total area in the trabecular region that was covered by αSMA+ cells were
1856 calculated on Fiji software. For preosteoblasts, the number of Osterix+ nuclei were
1857 counted and normalized to perimeter of trabecular bone for each mouse (Osx^+ cells/mm).
1858

1859 **2.9. Histomorphometry TRAcP and ALP analyses**

1860 Additional tibia bone sections were cryosectioned and baked at 42°C overnight to improve
1861 tissue adhesion while retaining endogenous enzymatic activity. Tibial bone sections were
1862 rehydrated in PBS before incubation in napthol-AS-MX phosphate (Sigma-Aldrich; 855-
1863 20) and fast blue RR salt (Sigma-Aldrich; FB25-10CAP) solution for 30 minutes to identify
1864 ALP+ regions with a dark blue stain. After washing in PBS, the same sections were
1865 incubated in basic stock solution for 5 minutes at 37°C. Tibial sections were developed in
1866 pararosaniline dye and sodium nitrite at 37°C for 3 minutes to highlight red TRAcP+ cells.
1867 Sections were further counterstained with hematoxylin to visualize bone morphology.
1868 Slides were mounted and imaged using EVOS Auto brightfield at 20X magnification. Five
1869 images per section were taken and the number of ALP+ cuboidal bone-lining osteoblasts
1870 and red multinucleated TRAcP+ osteoclasts per bone surface were calculated.
1871

1872 **2.10 Ex vivo mathematical myeloma advisor (EMMA) platform: Pentecost Myeloma**
1873 **Research Center cohort**. An *ex vivo* assay was used to quantify the chemosensitivity of primary
1874 MM cells[59-61]. Fresh BM aspirate cells were enriched for $CD138^+$ expression using Miltenyi
1875 (Bergisch Gladbach, Germany) 130-051-301 antibody-conjugated magnetic beads. MM cells
1876 ($CD138^+$) were seeded in Corning (Corning, NY) CellBIND 384 well plates with collagen I and
1877 previously established human-derived stroma, containing approximately 4000 MM cells and 1000
1878 stromal cells. Each well was filled with 80 µL of Roswell Park Memorial Institute (RPMI) 1640
1879 media supplemented with fetal bovine serum (FBS, heat inactivated), penicillin/streptomycin, and
1880 patient-derived plasma (10%, freshly obtained from patient's own aspirate, filtered) and left
1881 overnight for adhesion of stroma. The next day, drugs were added using a robotic plate handler

1882 so that every drug/combination was tested at 5 (fixed concentration ratio, for combinations)
1883 concentrations (1:3 serial dilution) in two replicates. Negative controls (supplemented growth
1884 media with and without the vehicle control dimethyl sulfoxide [DMSO]) were included, as well as
1885 positive controls for each drug (cell line MM1.S at highest drug concentration). Plates were placed
1886 in a motorized stage microscope (EVOS Auto FL, Life Technologies, Carlsbad, CA) equipped with
1887 an incubator and maintained at 5% CO_2 and 37 °C. Each well was imaged every 30 min for a total
1888 duration of up to 6 days. A digital image analysis algorithm[59-61] was implemented to determine
1889 changes in viability of each well longitudinally across the 96 or 144hr intervals. This algorithm
1890 computes differences in sequential images and identifies live cells with continuous membrane
1891 deformations resulting from their interaction with the surrounding extracellular matrix. These
1892 interactions cease upon cell death. By applying this operation to all 288 images acquired for each
1893 well, we quantified non-destructively, and without the need to separate the stroma and MM, the
1894 effect of drugs as a function of concentration and exposure time. Digital image analysis computes
1895 percent viability of MM cells for each time point and experimental condition (drug and
1896 concentration). For each patient-drug, we have a dose-time-response surface, which is abstracted
1897 into AUC (area under the curve), which is an area/integral measure of *ex vivo* response to therapy
1898 computed by taking an average of all *ex vivo* responses across all time (first 96h) and
1899 concentration. Clinical data was matched to patient samples ex vivo. Samples in the lowest AUC
1900 quartile were considered sensitive.
1901
1902
1903
1904 **2.10. Statistical Analysis**
1905 Statistical analysis was performed using the analysis of variance (ANOVA) with the
1906 appropriate post multiple comparison analysis in GraphPad prism 8.0-10.0.
1907

1908 **Supplementary Figures and Legends**

1909

1910

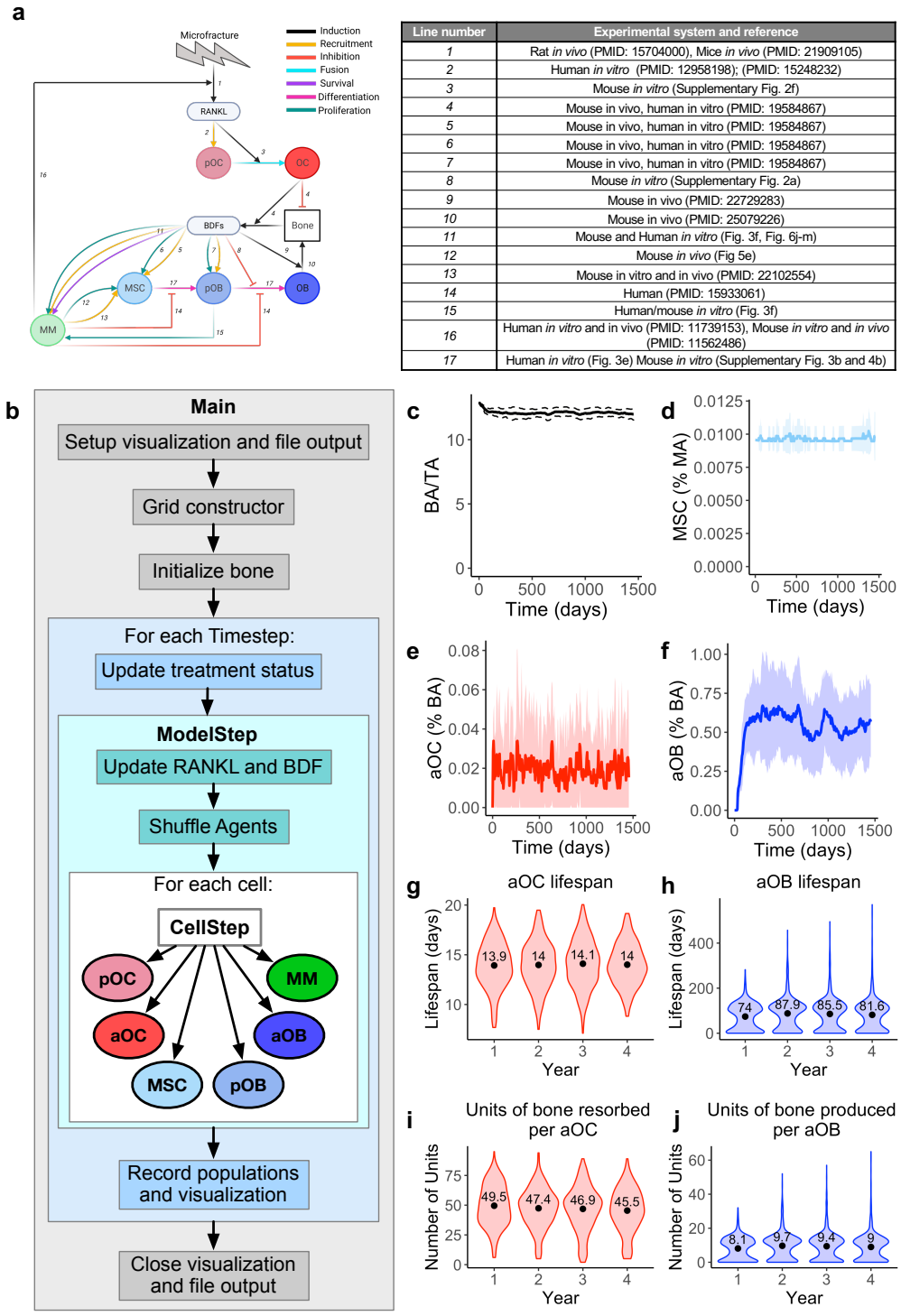

Line number	Experimental system and reference
1	Rat *in vivo* (PMID: 15704000), Mice *in vivo* (PMID: 21909105)
2	Human *in vitro* (PMID: 12958198); (PMID: 15248232)
3	Mouse *in vitro* (Supplementary Fig. 2f)
4	Mouse in vivo, human in vitro (PMID: 19584867)
5	Mouse in vivo, human in vitro (PMID: 19584867)
6	Mouse in vivo, human in vitro (PMID: 19584867)
7	Mouse in vivo, human in vitro (PMID: 19584867)
8	Mouse *in vitro* (Supplementary Fig. 2a)
9	Mouse in vivo (PMID: 22729283)
10	Mouse in vivo (PMID: 25079226)
11	Mouse and Human *in vitro* (Fig. 3f, Fig. 6j-m)
12	Mouse *in vivo* (Fig 5e)
13	Mouse in vitro and in vivo (PMID: 22102554)
14	Human (PMID: 15933061)
15	Human/mouse *in vitro* (Fig. 3f)
16	Human *in vitro* and in vivo (PMID: 11739153), Mouse *in vitro* and *in vivo* (PMID: 11562486)
17	Human *in vitro* (Fig. 3e) Mouse *in vitro* (Supplementary Fig. 3b and 4b)

1911

1912 **Supplementary Fig. 1. HCA captures key features of normal bone remodeling.**

1913 **a.** Interaction diagram (left) between cell types in the HCA and factors such as BDFs
1914 and RANKL (created with biorender.com). Table of references and experimental
1915 systems in which results were obtained (right).
1916 **b.** HCA flow diagram adapted from Bravo et al. (2020)[6].
1917 **c.** HCA model outputs of bone area to total area (BA/TA)
1918 **d.** HCA model outputs of MSC content.
1919 **e.** HCA model outputs of osteoclast numbers, and osteoblast numbers.
1920 **f-g**, Mean lifespan of osteoclasts **(f)** and osteoblasts **(g)** over 4 years of normal bone
1921 homeostasis. **h,** Mean units of bone resorbed per osteoclast each year of simulation.
1922 **i,** mean units of bone produced per osteoblast over course of the 4-year simulation.
1923

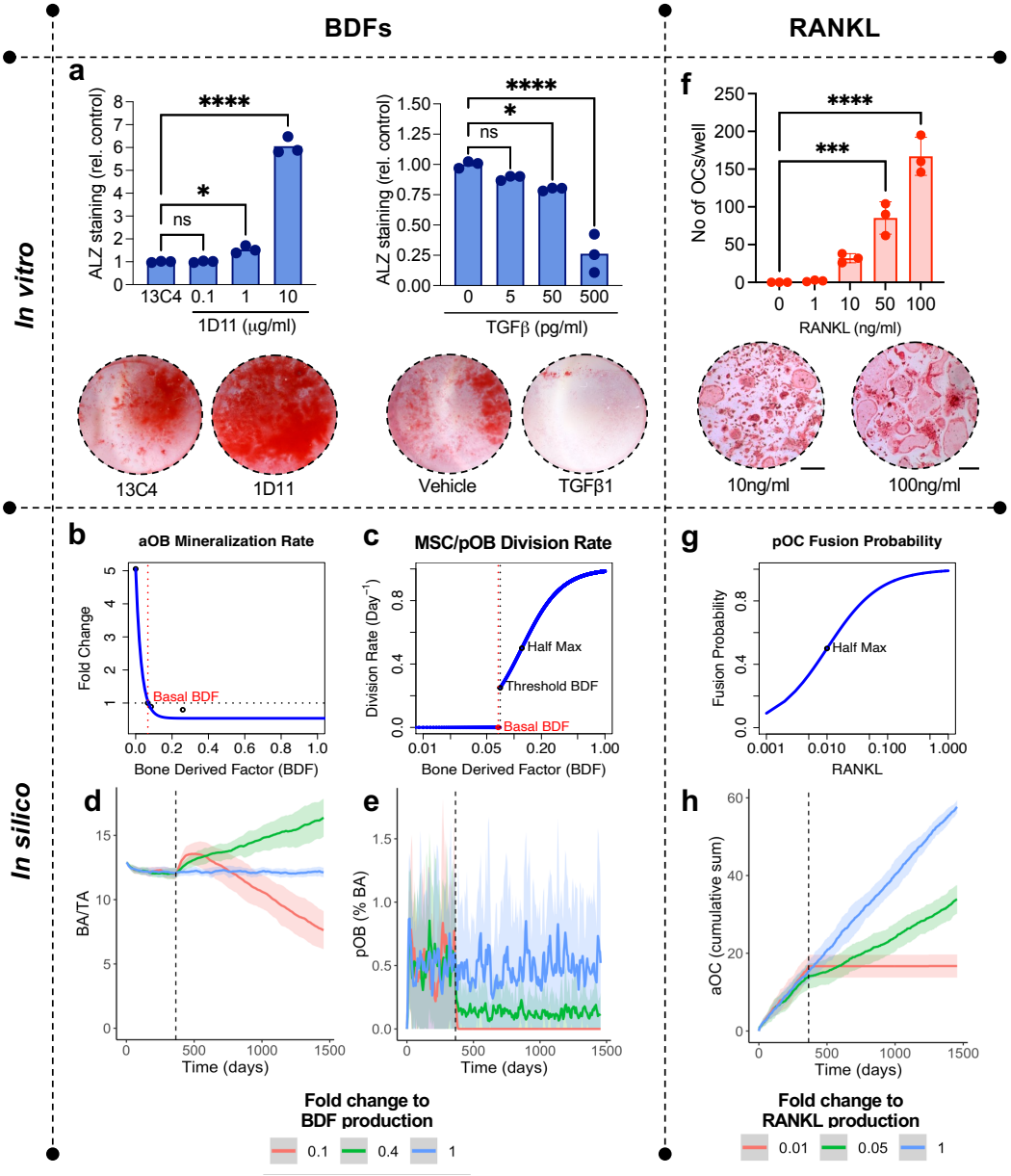

Supplementary Fig. 2. Inhibition of bone microenvironment cytokines in the HCA. a, The preosteoblast cell line MC3T3-E1 was cultured in osteogenic supplement with indicated concentrations of either isotype control antibody 13C4 or anti-TGF-β neutralizing antibody 1D11 (left) or TGF-β1 (right) for 14 days. Alizarin red was used to identify mineralized area. Results are normalized to isotype/vehicle-treated controls. Representative images of alizarin staining from control and highest

concentrations (below). **b-c**, Plots of functional forms used to represent the fold change to osteoblast mineralization rate (**b**) and MSC/preosteoblast division rate (**c**). The black dots (**b**) represent the data from the *in vitro* experiments with the MC3T3-E1 cells that were used to fit the exponential decay function, as described in section 1.1 of supplementary methods. The red dot (**c**) represents the lack of MSC/preosteoblast division rate when BDF is at a basal level (dotted red line), and the black dot (**c**) represents the division rate when BDF is at the threshold level for proliferation (dotted black line). Another black dot highlights the half maximum division rate defined by the Hill function.

* $p<0.05$ ** $p<0.01$, *** $p<0.001$, **** $p<0.0001$.

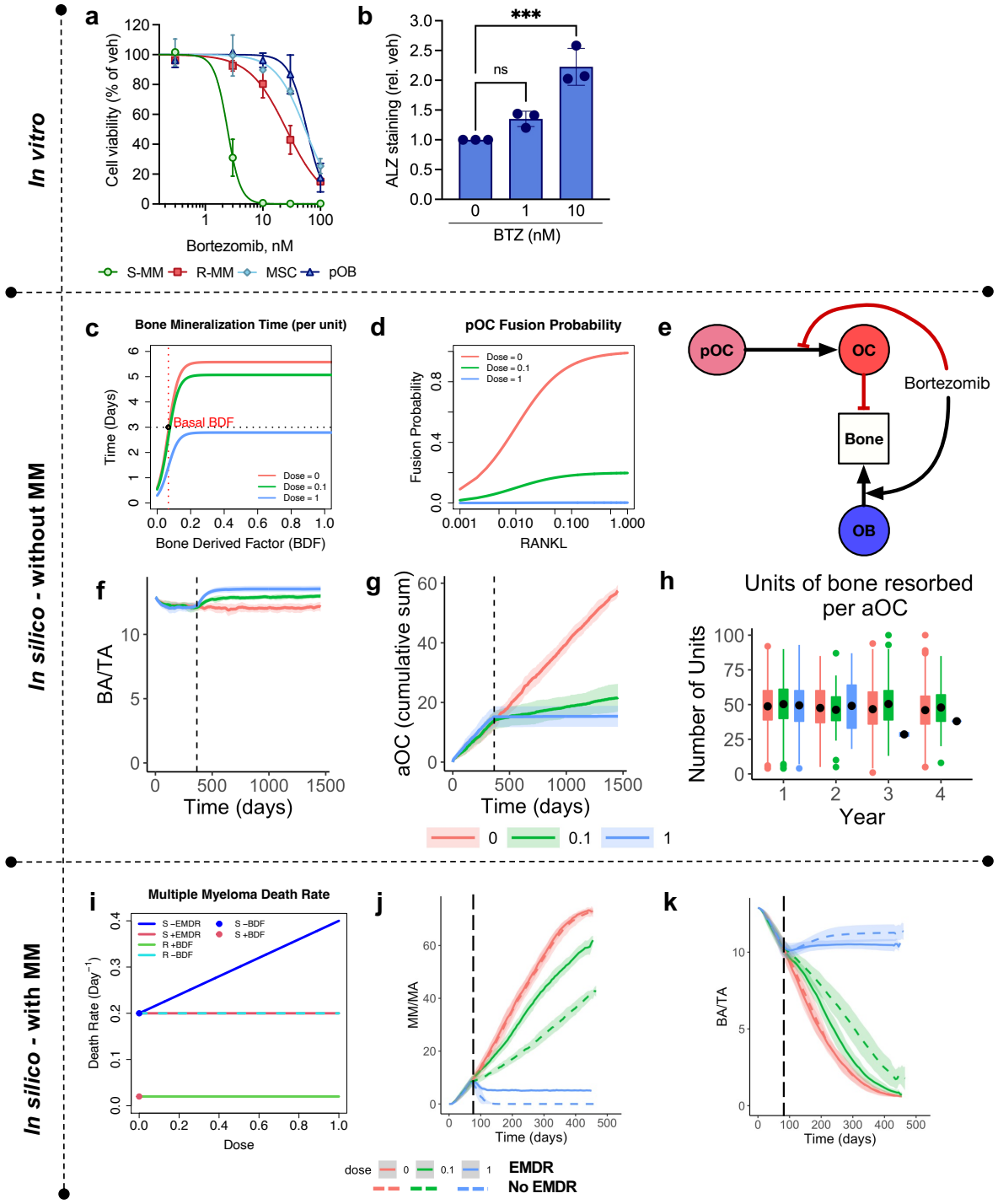

Supplementary Fig. 3. The impact of bortezomib (BTZ) on cells of the myeloma bone microenvironment *in vitro* and *in silico*. a, Sensitive U266 (S-MM) and resistant PSR (R-MM) myeloma, murine mesenchymal stromal cells (MSCs) and the preosteoblast cell line MC3T3-E1 (preosteoblast) were treated with varying

1948 concentrations of BTZ. Viability was measured after 72 hours by MTT assay. Results are
1949 normalized as percentage of control. **b**, the preosteoblast cell line MC3T3-E1 were
1950 cultured in osteogenic supplement with indicated concentrations of BTZ. Alizarin red was
1951 used to identify mineralized area. Results are normalized to vehicle-treated controls. **c-d**,
1952 Plots of functional forms used to represent the osteoblast mineralization time (**c**) and
1953 the probability of preosteoclast fusion (**d**) with indicated concentrations of bortezomib. **e**,
1954 Interaction diagram of normal bone cells with bortezomib. Red line denotes inhibition,
1955 black like indicates stimulation. **f-h**, Computational outputs of bone area to total area
1956 ratio (**f**), cumulative number of osteoclasts (**g**), and units of bone resorbed per osteoclast
1957 (**h**) following treatment of normal bone model with indicated concentrations of bortezomib.
1958 Treatment begins on day 365 (black dotted line) and is applied continuously for 3 years. **i**,
1959 Plot showing S-MM and R-MM death rate as a function of bortezomib with/without (+/-)
1960 BDF and +/- EMDR. **j**, Model outputs of MM growth with high and low doses of bortezomib
1961 with/without EMDR. Treatment begins when MM/MA=10% (black dotted line) and is
1962 applied continuously until MM/MA=20%. **k**, Flow chart outlining decisions MM cells
1963 make under BTZ treatment *** $p<0.001$.
1964

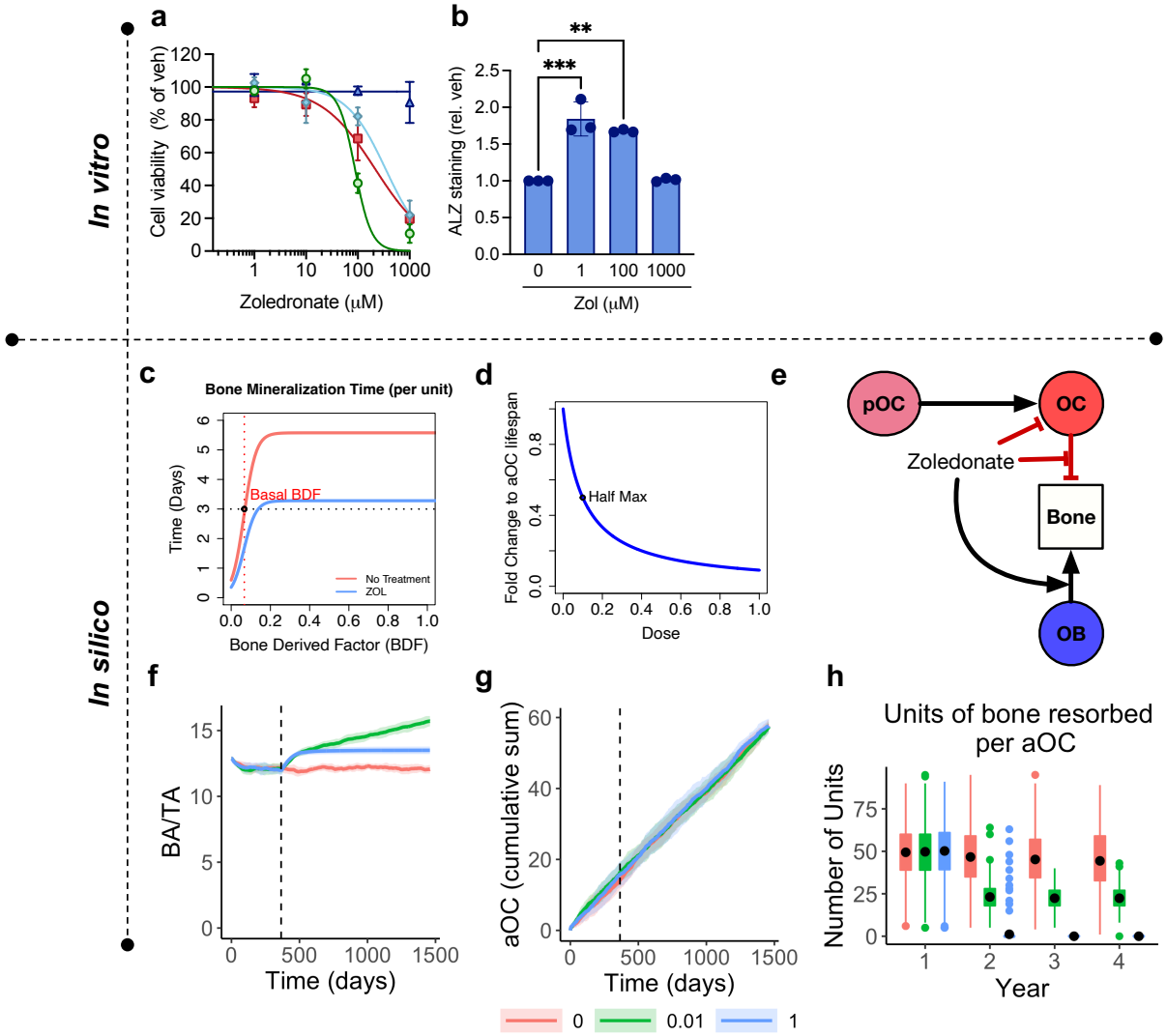

Supplementary Fig. 4. The impact of zoledronate (ZOL) on cells of the myeloma bone microenvironment *in vitro* and in *silico*. **a**, Sensitive U266 (S-MM) and resistant PSR (R-MM) myeloma, murine mesenchymal stromal cells (MSCs) and the preosteoblast cell line MC3T3-E1 (preosteoblast) were treated with varying concentrations of zoledronate (ZOL). Viability was measured after 72 hours by MTT assay. Results are normalized as percentage of control. **b**, The preosteoblast cell line MC3T3-E1 were cultured in osteogenic supplement with indicated concentrations of ZOL. Alizarin red was used to identify mineralized area. Results are normalized to vehicle-treated controls. **c-d**, Plots of functional forms used to represent the osteoblast mineralization time (**c**) and the fold change to osteoclast lifespan (**d**) with indicated concentrations of ZOL. **e**, Interaction diagram of normal bone cells with ZOL.

1977 Red line denotes inhibition, black like indicates stimulation. **f-h**, Computational outputs of
1978 bone area to total area ratio (**f**), cumulative number of osteoclasts (**g**), and units of bone
1979 resorbed per osteoclast (**h**) following treatment of normal bone model with indicated
1980 concentrations of ZOL. Treatment begins on day 365 (black dotted line) and is
1981 applied continuously for 3 years, *** $p<0.001$, **** $p<0.0001$.
1982

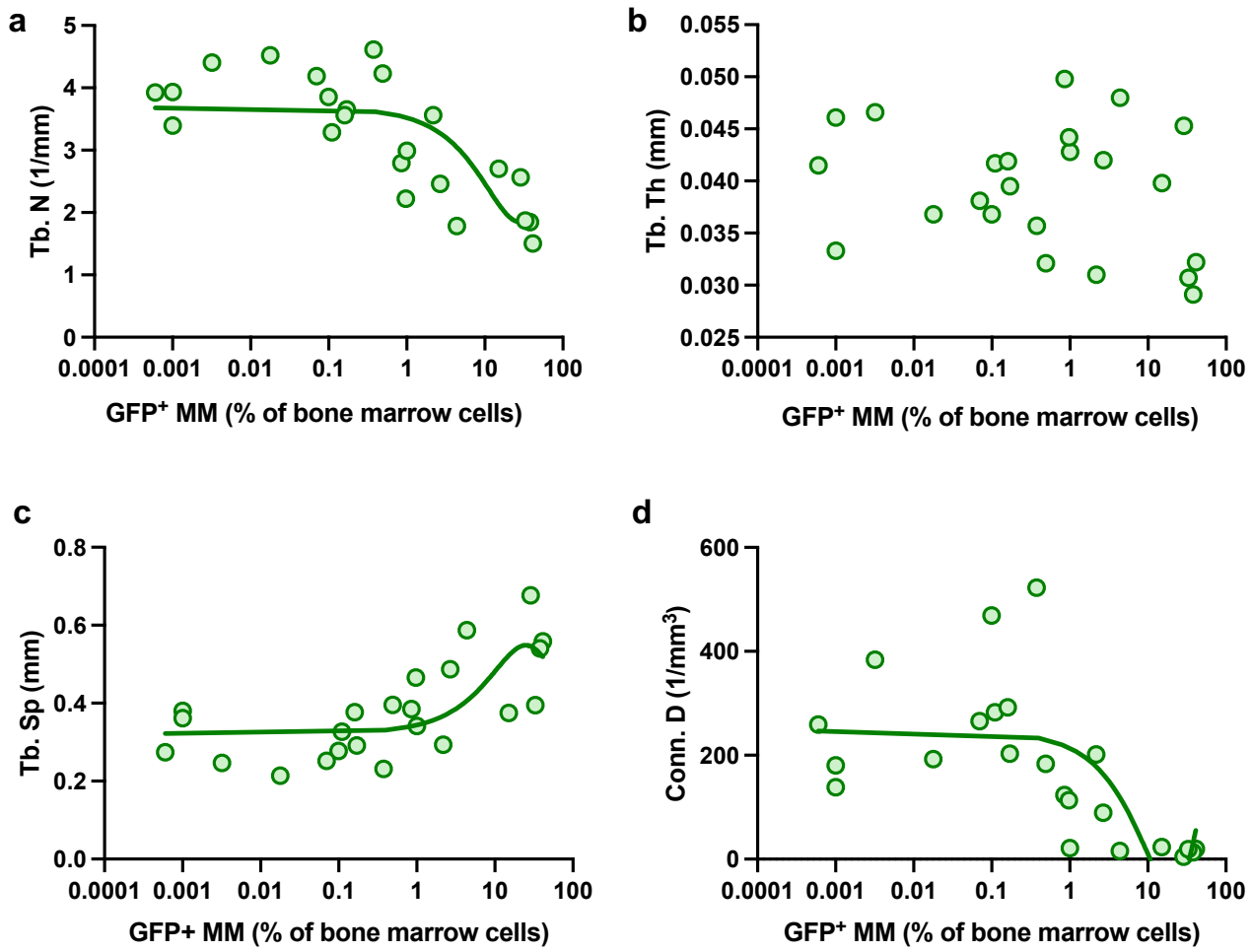

Supplementary Fig. 5. Myeloma alters bone microarchitecture *in vivo*. a-d, Tumor burden in tibia and femur was assessed by GFP positivity by flow cytometry in U266-bearing mice. High resolution microCT was used to assess trabecular number (Tb.N; **a**), thickness (Tb.Th; **b**) and spacing (Tb.Sp; **c**) and degree of connectivity (Conn.D; **d**).

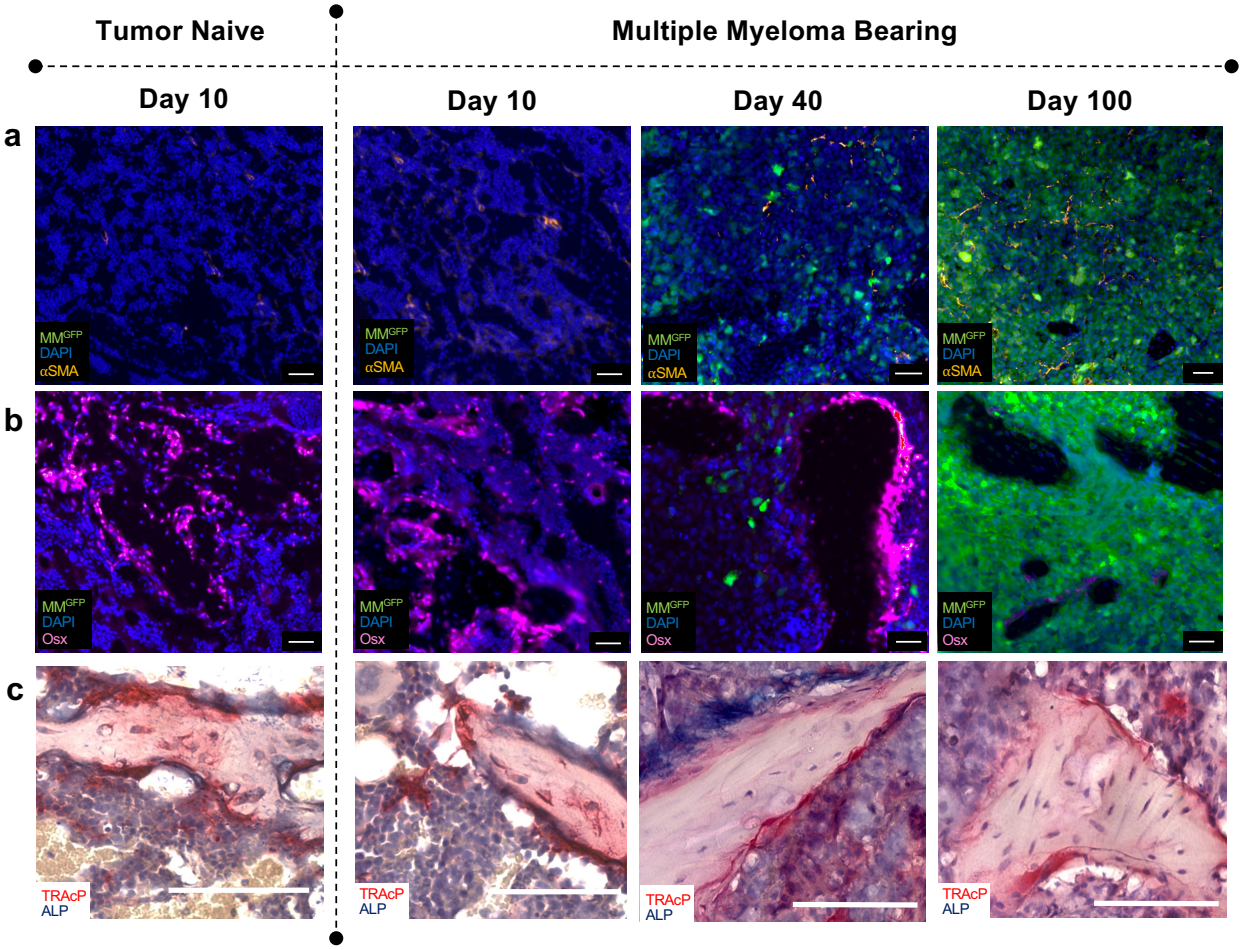

1991

1992 **Supplementary Fig. 6. Multiple myeloma alters bone marrow microenvironment. a-**
1993 **b**, Tumor naïve or U266GFP-bearing mice were sacrificed on indicated days to identify
1994 and localize αSMA+ mesenchymal stromal cells
1995 (gold; **a**), osterix+ preosteoblasts (pink; **b**) and GFP+ U266 cells (green; **a-b**)
1996 by immunofluorescence. Scale bars = 50μm **c**, Brightfield images of TRAcP+
1997 multinucleated osteoclasts (red) and ALP+ cuboidal bone-lining osteoblasts (blue). Scale
1998 bars = 100μm. Images correspond with quantifications from Figure 6.

1999

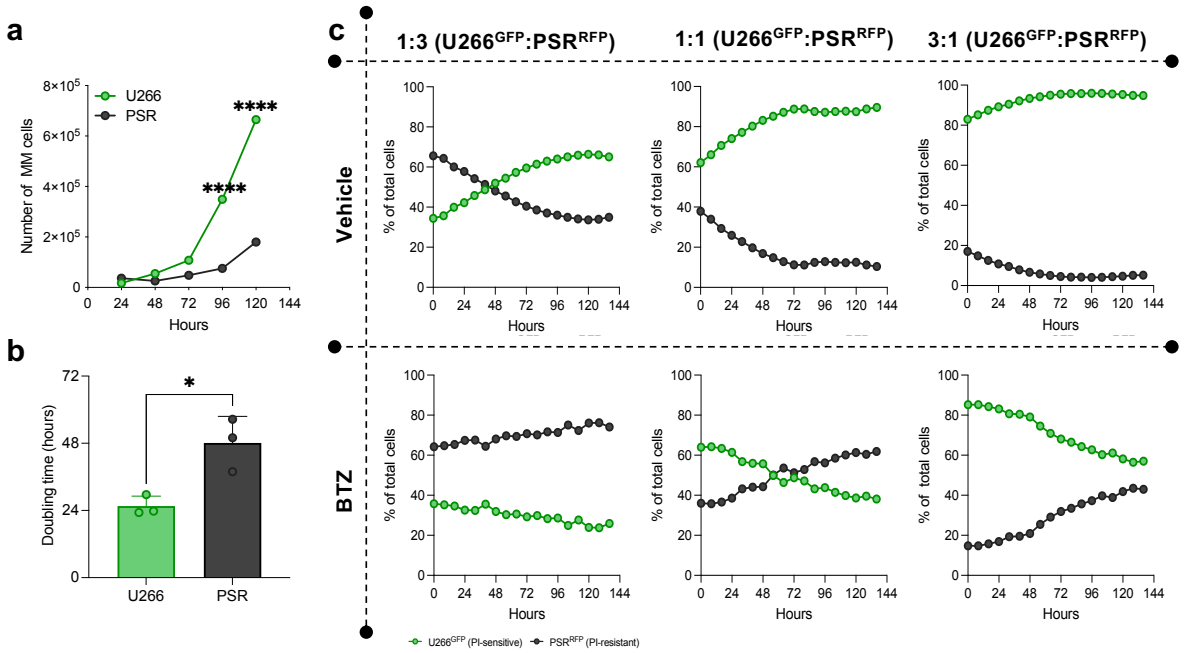

Supplementary Fig. 7. PI-sensitive MM cells outgrow their PI-resistant counterparts under normal growth conditions. **a-b**, PI-sensitive U266 and PI-resistant PSR MM cell lines were grown in standard culture conditions, the number of cell number was recorded using trypan blue staining over 120h (**a**) and used to calculate doubling times (**b**). Proteasome inhibitor sensitive GFP expressing U266 MM cells were incubated at indicated ratios with their proteasome inhibitor RFP expressing counterparts (PSR) . The percentage of each population under vehicle control conditions was monitored over time using real time imaging microscopy (Incucyte). In parallel the impact of BTZ (4nM) on the outgrowth of the populations was observed revealing the emergence of the resistant population over time.

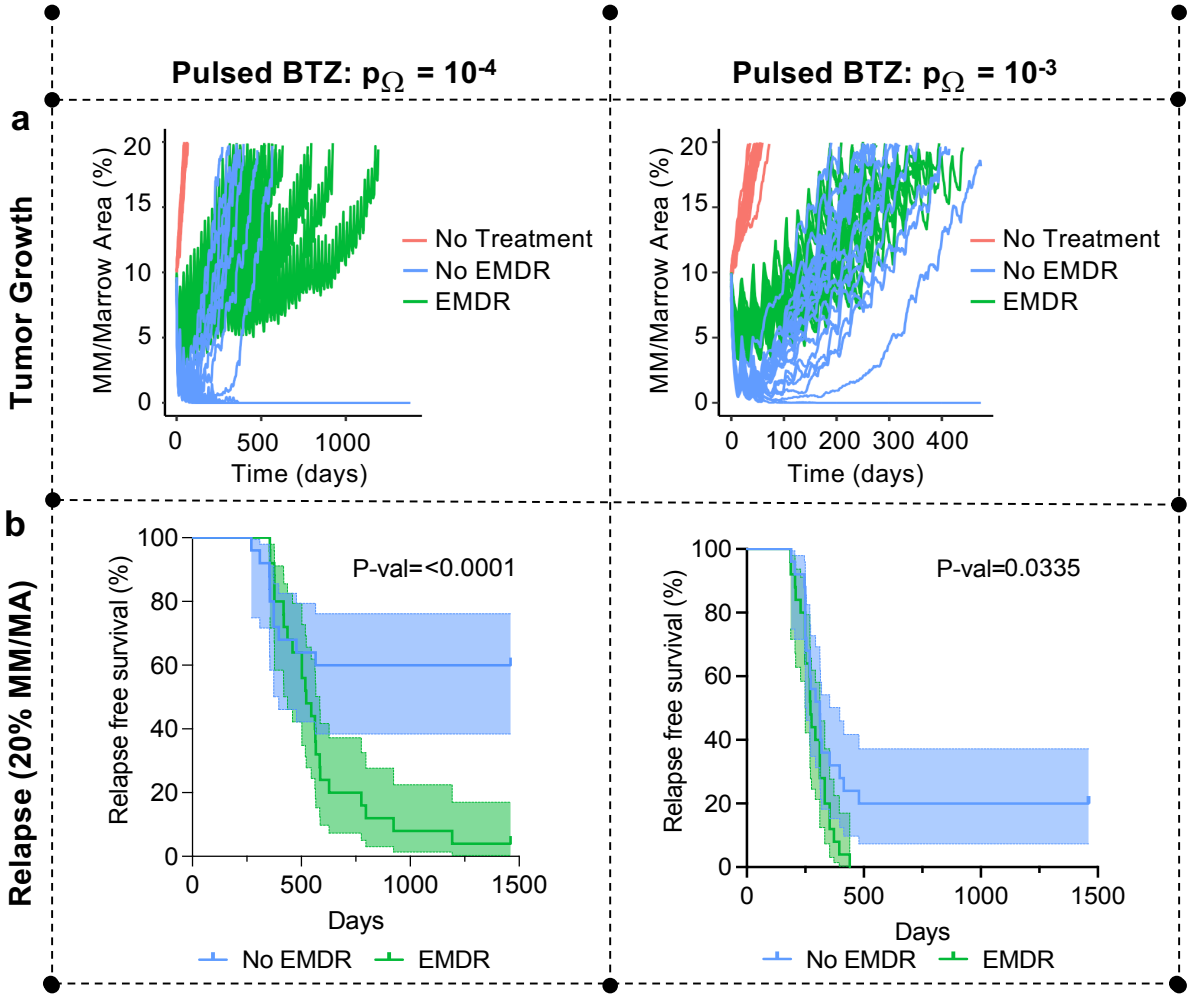

Supplementary Fig. 8. EMDR increases rate of myeloma relapse and tumor heterogeneity under pulsed bortezomib treatment. Pulsed BTZ treatment (2 weeks on therapy, 1 week off) was applied to HCA model when MM burden reached 10% of the marrow. **a-b**, Tumor growth (**a**) for individual simulations (n = 25 per condition) and Kaplan Meier plots of rate of relapse (**b**) for pulsed BTZ therapy were calculated when $p_\Omega = 10^{-4}$ (left column) and $p_\Omega = 10^{-3}$ (right column).

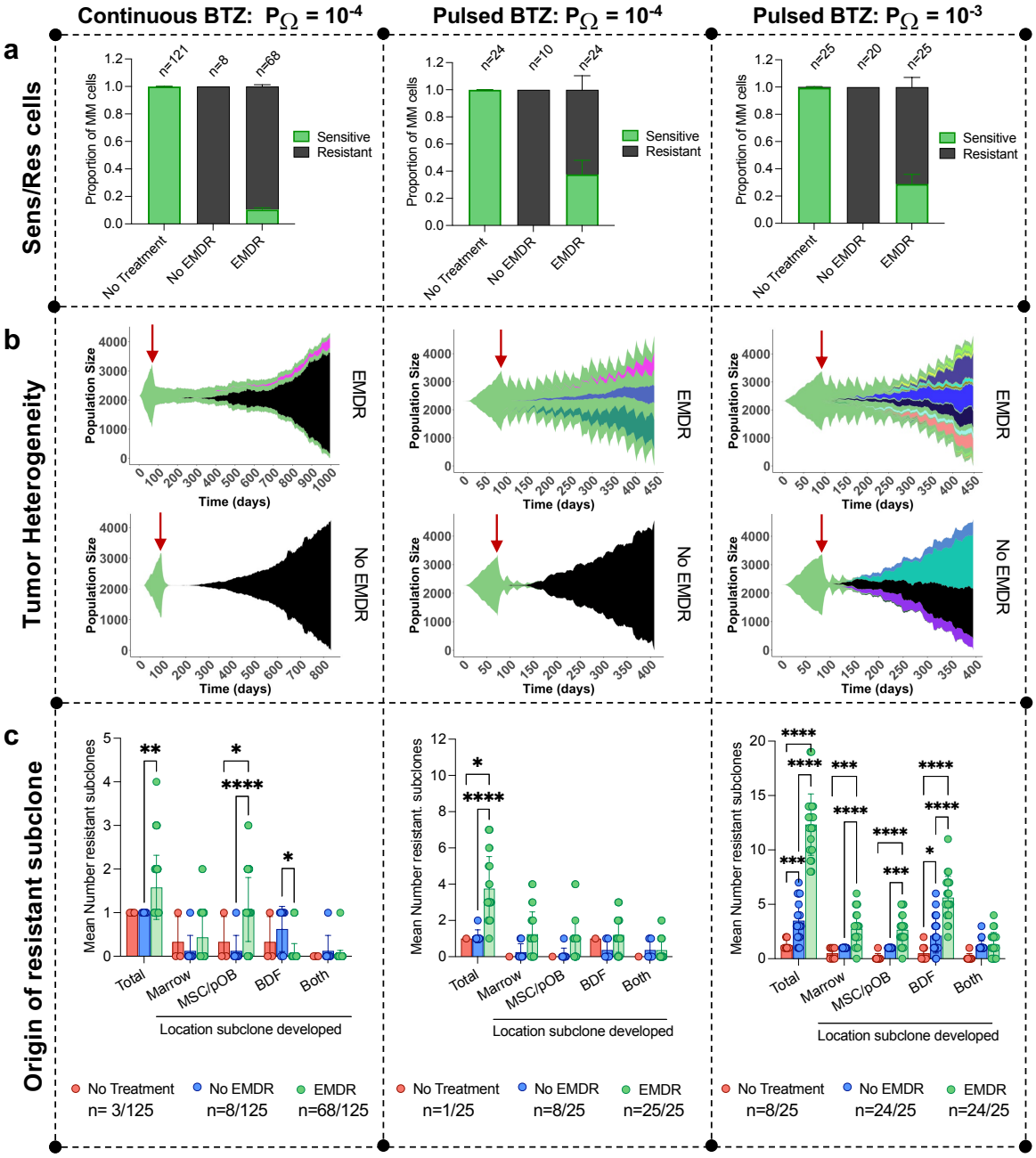

Supplementary Fig. 9. EMDR increases tumor heterogeneity under continuous and pulsed bortezomib treatment. Continuous BTZ treatment (left column) or Pulsed BTZ treatment (2 weeks on therapy, 1 week off; middle and right column) were applied to HCA model when MM burden reached 10% of the marrow. **a-c**, The proportion of sensitive/resistant MM cells at end point (MM = 20% of the marrow; **a**) and tumor heterogeneity (**b-c**) were assessed with two resistance probabilities (left and middle columns, $p_\Omega = 10^{-4}$, right column $p_\Omega = 10^{-3}$) in the presence or absence of EMDR. **b**, Muller

2028 plots indicating resistant subclones arising in tumor, created using EvoFreq[62]. Each color
2029 represents a unique subclone. Red arrow indicates start of treatment. **c,** Mean number of
2030 resistant sub-clones arising in tumors that reached 20% and contained
2031 resistant subclones (MM/MA) following continuous or pulsed BTZ treatment at different
2032 locations within the BME with/without EMDR. 'Both' refers to resistant subclones that
2033 arise close to MSCs and BDFs. Overall, EMDR leads to significantly higher numbers of
2034 resistant subclones.
2035

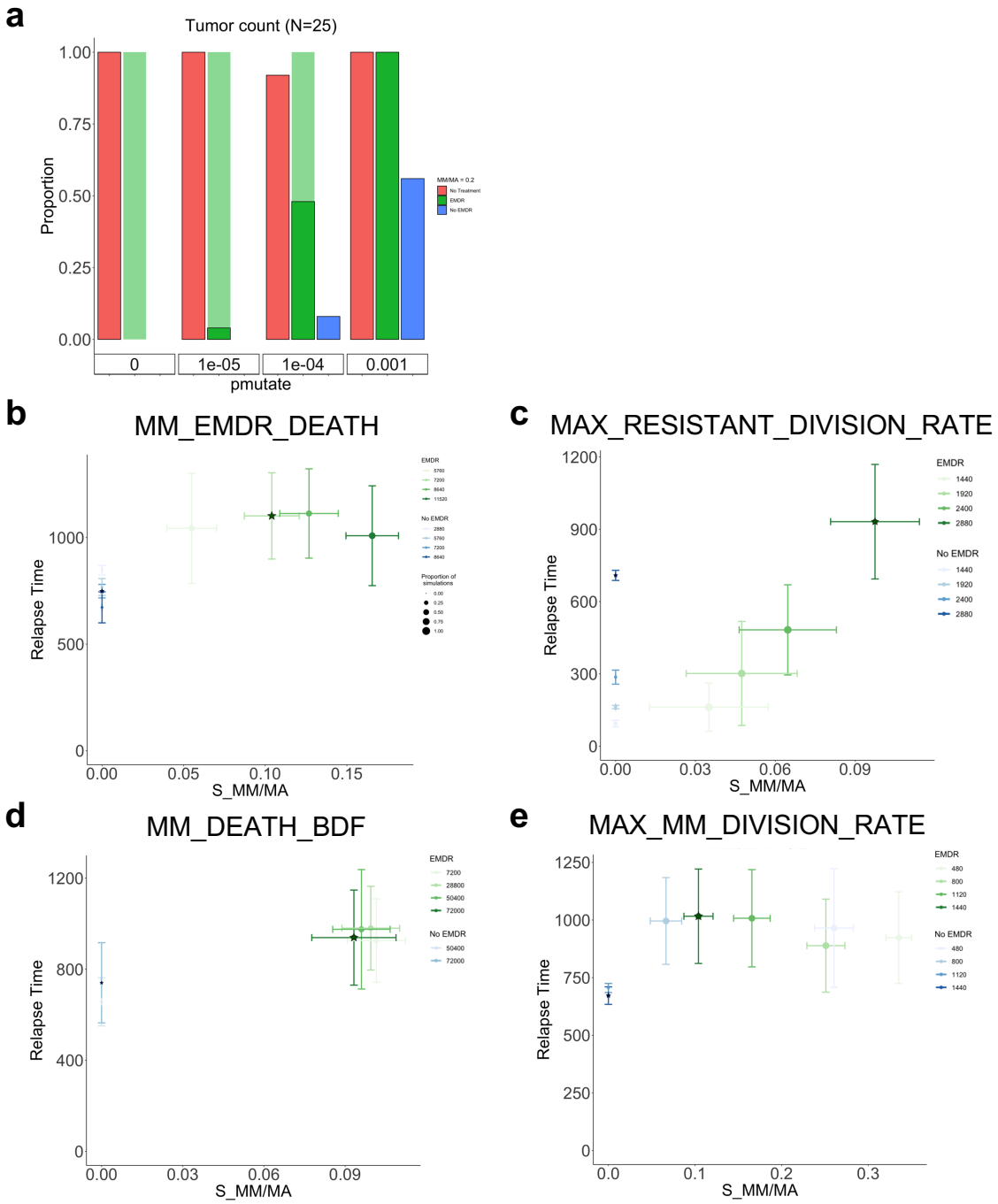

Supplementary Fig. 10. The impact of select parameter values on key model outputs. Continuous BTZ treatment was applied to HCA model when MM burden reached 10% of the marrow. **a.** Proportion of tumors that survived (lighter shade) or relapsed (darker shade) was assessed as resistance probability increased. **b-e**. Select parameters were varied to assess how the relapse time (when MM burden reached 20% of the marrow) and proportion of sensitive cells at endpoint changed due to parameter

2043 values ($p_{\Omega} = 10^{-4}$). MM_EMDR_DEATH is the lifespan of sensitive cells (+ BTZ) protected
2044 by EMDR (**b**). MAX_RESISTANT_DIVISION_RATE is the maximum division time of
2045 resistant cells (+/- BTZ) (**c**). MM_DEATH_BDF is the lifespan of sensitive cells (-BTZ) or
2046 resistant cells (+/- BTZ) in the presence of BDF (**d**). MAX_MM_DIVISION_RATE is
2047 the maximum division time of sensitive cells (+/- BTZ) in the presence of
2048 MSC/preosteoblast (**e**). The star marker indicates the outputs corresponding to the
2049 baseline parameter value. The circular marker indicates the mean value of the outputs
2050 with error bars representing the standard deviation of the simulations (n = 25); the size of
2051 the circular marker increases as the proportion of simulations that reached the endpoint
2052 increased.
2053

2054

2055 **Supplementary Video 1. HCA model recapitulates normal bone remodeling.**

2056 HCA simulation of normal bone remodeling, showing agent grid (top) and PDE grids with
2057 scaled concentration of RANKL (bottom left) and bone derived factors (BDF, bottom right)
2058 over one year. Each bone remodeling event is initiated through a small microfracture,
2059 which creates a signal to osteoblast lineage cells to express
2060 RANKL. Preosteoclasts migrate to the bone remodeling site and undergo fusion in
2061 response to RANKL to become a fully formed osteoclast. As the osteoclast resorbs the
2062 bone, BDF is released from the bone matrix which promotes the proliferation
2063 of preosteoblasts. During the reversal period, BDF continues to be released at a lower
2064 level, causing the preosteoblasts to migrate and attach to the eroded surface. Low BDF
2065 promotes the differentiation of preosteoblasts into bone-forming osteoblasts,
2066 which continue to build bone until the amount of bone that was resorbed is replaced. The
2067 bone formation phase is then followed by a period of quiescence until bone remodeling
2068 is re-initiated at the given location.

2069 YouTube link: https://www.youtube.com/watch?v=UFpXzLNFMzo

2070

2071

2072 **Supplementary Video 2. HCA model captures key steps of myeloma-bone vicious**
2073 **cycle.**

2074 HCA simulation of the myeloma-bone vicious cycle, showing agent grid (top) and PDE
2075 grids with scaled concentration of RANKL (bottom left) and bone derived factors (BDF,
2076 bottom right) over one year. Each simulation is initialized with a single MM cell after the
2077 formation of the first osteoclast. MM increases the number of osteoclasts which drives
2078 bone resorption and the release of BDFs. BDFs and MSCs that are recruited in response
2079 to MM contribute to the growth and survival of MM cells (light green cells), causing MM
2080 cells to further expand in the bone marrow. At the same time, MM cells inhibit the
2081 differentiation of MSCs and preosteoblasts, preventing the formation of bone and further
2082 driving osteolytic bone disease.

2083 YouTube link: https://www.youtube.com/watch?v=NFdpWp2l1wg

2084

2085

2086 **Supplementary Video 3. EMDR increases minimal residual disease.**

2087 HCA simulation of continuous treatment with bortezomib (BTZ), showing agent grid (top)
2088 and PDE grids with scaled concentration of RANKL (bottom left) and bone derived factors
2089 (BDF, bottom right). Treatment begins when multiple myeloma (MM) cells have reached
2090 10% of the bone marrow (the starting point of the supplemental video) and continues until
2091 the MM burden doubles. After treatment begins, MM cells have a probability of resistance
2092 (p_Ω) during cell division that causes resistance to BTZ. When $p_\Omega = 10^{-4}$, EMDR (middle)
2093 protected a portion of sensitive cells, enabling them to acquire resistance and drive tumor
2094 relapse. When EMDR is absent (right), the tumor went extinct.

2095

2096 YouTube link: https://www.youtube.com/watch?v=fnBuxXvWWXw

2097

2098

2099 **Supplementary Video 4. Higher resistance probability increases tumor relapse**
2100 **rates in absence of EMDR.**

2101 HCA simulation of continuous treatment with bortezomib (BTZ), showing agent grid (top)
2102 and PDE grids with scaled concentration of RANKL (bottom left) and bone derived factors
2103 (BDF, bottom right). Treatment begins when multiple myeloma (MM) cells have reached
2104 10% of the bone marrow (the starting point of the supplemental video) and continues until
2105 the MM burden doubles. After treatment begins, MM cells have a probability of resistance
2106 (p_Ω) during cell division that causes resistance to BTZ. When $p_\Omega = 10^{-3}$, EMDR (middle)
2107 protected a portion of sensitive cells, enabling them to acquire resistance and drive tumor
2108 relapse. When EMDR is absent (right), the high resistance probability prevents tumors
2109 from going extinct before the acquisition of intrinsic resistance and also drives tumor
2110 relapse.

2111

2112 YouTube link: https://www.youtube.com/watch?v=EJUOy0yepWw

2113

2114 **References:**

1 Araujo, A., Cook, L. M., Lynch, C. C. & Basanta, D. An integrated computational model of the bone microenvironment in bone-metastatic prostate cancer. *Cancer Res* **74**, 2391-2401 (2014). https://doi.org:10.1158/0008-5472.CAN-13-2652

2 Araujo, A., Cook, L. M., Lynch, C. C. & Basanta, D. Size Matters: Metastatic cluster size and stromal recruitment in the establishment of successful prostate cancer to bone metastases. *Bull Math Biol* **80**, 1046-1058 (2018). https://doi.org:10.1007/s11538-018-0416-4

3 Cook, L. M., Araujo, A., Pow-Sang, J. M., Budzevich, M. M., Basanta, D. & Lynch, C. C. Predictive computational modeling to define effective treatment strategies for bone metastatic prostate cancer. *Sci Rep* **6**, 29384 (2016). https://doi.org:10.1038/srep29384

4 Terstappen, L. W. & Levin, J. Bone marrow cell differential counts obtained by multidimensional flow cytometry. *Blood Cells* **18**, 311-330; discussion 331-312 (1992).

5 Pittenger, M. F. *et al.* Vol. 284 143-147 (1999).

6 Bravo, R. R. *et al.* Hybrid Automata Library: A flexible platform for hybrid modeling with real-time visualization. *PLoS Comput Biol* **16**, e1007635 (2020). https://doi.org:10.1371/journal.pcbi.1007635

7 Sims, N. A. & Martin, T. J. Vol. 3 1-10 (2014).

8 Kular, J., Tickner, J., Chim, S. M. & Xu, J. Vol. 45 863-873 (The Canadian Society of Clinical Chemists, 2012).

9 Manolagas, S. C. Vol. 21 115-137 (2000).

10 Roodman, G. D. Vol. 2 389-409 (1991).

11 Alon, U. (Chapman and Hall/CRC, 2006).

12 Mosheimer, B. A., Kaneider, N. C., Feistritzer, C., Sturn, D. H. & Wiedermann, C. J. Vol. 50 2309-2316 (2004).

13 Breuil, V., Schmid-Antomarchi, H., Schmid-Alliana, A., Rezzonico, R., Euller-Ziegler, L. & Rossi, B. Vol. 17 1751-1753 (2003).

14 Anderson, A. R. A. Vol. 22 163-186 (2005).

15 Delaisse, J.-M. Vol. 3 1-8 (Nature Publishing Group, 2014).

16 Sims, N. A. & Martin, T. J. Vol. 82 507-529 (2020).

17 Novack, D. V. & Faccio, R. Osteoclast motility: putting the brakes on bone resorption. *Ageing Res Rev* **10**, 54-61 (2011). https://doi.org:10.1016/j.arr.2009.09.005

18 van den Dries, K., Linder, S., Maridonneau-Parini, I. & Poincloux, R. Probing the mechanical landscape - new insights into podosome architecture and mechanics. *J Cell Sci* **132** (2019). https://doi.org:10.1242/jcs.236828

19 Bianco, P. *et al.* The meaning, the sense and the significance: translating the science of mesenchymal stem cells into medicine. *Nat Med* **19**, 35-42 (2013). https://doi.org:10.1038/nm.3028

20 Greenbaum, A. *et al.* CXCL12 in early mesenchymal progenitors is required for haematopoietic stem-cell maintenance. *Nature* **495**, 227-230 (2013). https://doi.org:10.1038/nature11926

21 Mendez-Ferrer, S. *et al.* Mesenchymal and haematopoietic stem cells form a unique bone marrow niche. *Nature* **466**, 829-834 (2010). https://doi.org:10.1038/nature09262

22 Tang, Y. *et al.* TGF-beta1-induced migration of bone mesenchymal stem cells couples bone resorption with formation. *Nat Med* **15**, 757-765 (2009). https://doi.org:10.1038/nm.1979

23 Wu, M., Chen, G. & Li, Y. P. Vol. 4 (2016).

24 Civitelli, R. Cell-cell communication in the osteoblast/osteocyte lineage. *Arch Biochem Biophys* **473**, 188-192 (2008). https://doi.org:10.1016/j.abb.2008.04.005

25 Stains, J. P. & Civitelli, R. Cell-cell interactions in regulating osteogenesis and osteoblast function. *Birth Defects Res C Embryo Today* **75**, 72-80 (2005). https://doi.org:10.1002/bdrc.20034

26 Stains, J. P., Watkins, M. P., Grimston, S. K., Hebert, C. & Civitelli, R. Molecular mechanisms of osteoblast/osteocyte regulation by connexin43. *Calcif Tissue Int* **94**, 55-67 (2014). https://doi.org:10.1007/s00223-013-9742-6

27 Watkins, M. *et al.* Osteoblast connexin43 modulates skeletal architecture by regulating both arms of bone remodeling. *Mol Biol Cell* **22**, 1240-1251 (2011). https://doi.org:10.1091/mbc.E10-07-0571

28 Nakashima, T. *et al.* (2011).

29 Xiong, J., Onal, M., Jilka, R. L., Weinstein, R. S., Manolagas, S. C. & O'Brien, C. A. Vol. 17 1235-1241 (2011).

30 Batlle, E. & Massagué, J. Vol. 50 924-940 (2019).

31 Sezer, O., Heider, U., Zavrski, I., Kühne, C. A. & Hofbauer, L. C. Vol. 101 2094-2098 (2003).

32 Xu, S., Menu, E., De Becker, A., Van Camp, B., Vanderkerken, K. & Van Riet, I. Vol. 30 266-279 (2012).

33 Hideshima, T., Mitsiades, C., Tonon, G., Richardson, P. G. & Anderson, K. C. Vol. 7 585-598 (2007).

34 Edwards, C. M., Zhuang, J. & Mundy, G. R. Vol. 42 1007-1013 (2008).

35 Kassen, D. *et al.* Myeloma impairs mature osteoblast function but causes early expansion of osteo-progenitors: temporal changes in bone physiology and gene expression in the KMS12BM model. *Br J Haematol* **172**, 64-79 (2016). https://doi.org:10.1111/bjh.13790

36 Hurchla, M. A. *et al.* Vol. 27 430-440 (2013).

37 Meads, M. B., Gatenby, R. A. & Dalton, W. S. Vol. 9 665-674 (2009).

38 Janssens, K., ten Dijke, P., Janssens, S. & Van Hul, W. Transforming growth factor-beta1 to the bone. *Endocr Rev* **26**, 743-774 (2005). https://doi.org:10.1210/er.2004-0001

39 Brown, D. R. Vol. 72 943-953 (Wiley Online Library, 1999).

40 Goodhill, G. J. Vol. 9 1414-1421 (Wiley Online Library, 1997).

41 Zaccai, N. R., Serdyuk, I. N. & Zaccai, J. (Cambridge University Press, 2017).

42 Syková, E. & Nicholson, C. Vol. 88 1277-1340 (American Physiological Society, 2008).

43 Kaminska, B., Wesolowska, A. & Danilkiewicz, M. Vol. 52 329-337 (2005).

44 Helgason, B., Perilli, E., Schileo, E., Taddei, F., Brynjólfsson, S. & Viceconti, M. Vol. 23 135-146 (2008).

45 Pfeilschifter, J. *et al.* Vol. 13 716-730 (1998).

46 Parfitt, A. M. Vol. 55 273-286 (1994).

47 Akchurin, T., Aissiou, T., Kemeny, N., Prosk, E., Nigam, N. & Komarova, S. V. Vol. 3 (2008).

2208 48 Wergedal, J., Stauffer, M., Baylink, D. & Rich, C. Vol. 52 1052-1058 (1973).
2209 49 Bloebaum, R. D., Bachus, K. N., Momberger, N. G. & Hofmann, A. A. Vol. 28
2210 537-544 (1994).
2211 50 Tranquillo, R. T., Zigmond, S. H. & Lauffenburger, D. A. Vol. 11 1-15 (1988).
2212 51 Bianchi, A., Painter, K. J. & Sherratt, J. A. Vol. 78 1904-1941 (Springer US,
2213 2016).
2214 52 Khodadadi, L., Cheng, Q., Radbruch, A. & Hiepe, F. Vol. 10 721 (2019).
2215 53 Chen, S. *et al.* Vol. 72 4225-4237 (AACR, 2012).
2216 54 Chen, S. *et al.* Vol. 124 2687-2697 (American Society of Hematology
2217 Washington, DC, 2014).
2218 55 Bishop, R. T. *et al.* Pharmacological inhibition of the IKKepsilon/TBK-1 axis
2219 potentiates the anti-tumour and anti-metastatic effects of Docetaxel in mouse
2220 models of breast cancer. *Cancer Lett* **450**, 76-87 (2019).
2221 https://doi.org:10.1016/j.canlet.2019.02.032
2222 56 Marino, S., Bishop, R. T., de Ridder, D., Delgado-Calle, J. & Reagan, M. R. 2D
2223 and 3D In Vitro Co-Culture for Cancer and Bone Cell Interaction Studies. *Methods*
2224 *Mol Biol* **1914**, 71-98 (2019). https://doi.org:10.1007/978-1-4939-8997-3_5
2225 57 McGuire, J. J. *et al.* Mesenchymal stem cell-derived interleukin-28 drives the
2226 selection of apoptosis resistant bone metastatic prostate cancer. *Nat Commun* **12**,
2227 723 (2021). https://doi.org:10.1038/s41467-021-20962-6
2228 58 Schindelin, J. *et al.* Vol. 9 676-682 (Nature Publishing Group, 2012).
2229 59 Silva, A., Jacobson, T., Meads, M., Distler, A. & Shain, K. An Organotypic High
2230 Throughput System for Characterization of Drug Sensitivity of Primary Multiple
2231 Myeloma Cells. *J Vis Exp*, e53070 (2015). https://doi.org:10.3791/53070
2232 60 Silva, A. *et al.* An Ex Vivo Platform for the Prediction of Clinical Response in
2233 Multiple Myeloma. *Cancer Res* **77**, 3336-3351 (2017).
2234 https://doi.org:10.1158/0008-5472.CAN-17-0502
2235 61 Sudalagunta, P. *et al.* A pharmacodynamic model of clinical synergy in multiple
2236 myeloma. *EBioMedicine* **54**, 102716 (2020).
2237 https://doi.org:10.1016/j.ebiom.2020.102716

62 Gatenbee, C. D., Schenck, R. O., Bravo, R. R. & Anderson, A. R. A. Vol. 20 1-4 (Springer, 2019).